Computer simulations of microstructures related to the olivine→spinel transition

Dissertation zur Erlangung des Grades
„Doktor der Naturwissenschaften “

am Fachbereich Geowissenschaften
der Johannes Gutenberg-Universität Mainz

Till Sachau
geboren in Bernkastel-Kues

Mainz, 24. Mai 2008

Erklärung

Hiermit versichere ich, die vorliegende Arbeit selbstständig und nur unter Verwendung der angegebenen Quellen und Hilfsmittel verfasst zu haben.

Mainz, 24. Mai 2008

Zusammenfassung

Tiefherd-Beben, die im oberen Erdmantel in einer Tiefe von ca. 400 km auftreten, werden gewöhnlich mit dem in gleicher Tiefe auftretenden druckabhängigen, polymorphen Phasenübergang von Olivine (α-Phase) zu Spinel (β-Phase) in Verbindung gebracht. Es ist jedoch nach wie vor unklar, wie der Phasenübergang mit dem mechanischen Versagen des Mantelmaterials zusammenhängt. Zur Zeit werden im Wesentlichen zwei Modelle diskutiert, die entweder Mikrostrukturen, die durch den Phasenübergang entstehen, oder aber die rheologischen Veränderungen des Mantelgesteins durch den Phasenübergang dafür verantwortlich machen. Dabei sind Untersuchungen der Olivin→Spinel Umwandlung durch die Unzugänglichkeit des natürlichen Materials vollständig auf theoretische Überlegungen sowie Hochdruck-Experimente und Numerische Simulationen beschränkt.

Das zentrale Thema dieser Dissertation war es, ein funktionierendes Computermodell zur Simulation der Mikrostrukturen zu entwickeln, die durch den Phasenübergang entstehen. Des Weiteren wurde das Computer Modell angewandt um die mikrostrukturelle Entwicklung von Spinel Körnern und die Kontrollparameter zu untersuchen.

Die Arbeit ist daher in zwei Teile unterteilt: Der erste Teil (Kap. 2 und 3) behandelt die physikalischen Gesetzmäßigkeiten und die prinzipielle Funktionsweise des Computer Modells, das auf der Kombination von Gleichungen zur Errechnung der kinetischen Reaktionsgeschwindigkeit mit Gesetzen der Nichtgleichgewichtsthermodynamik unter nicht-hydostatischen Bedingungen beruht. Das Computermodell erweitert ein Federnetzwerk der Software *latte* aus dem Programmpaket *elle*.

Der wichtigste Parameter ist dabei die Normalspannung auf der Kornoberfläche von Spinel. Darüber hinaus berücksichtigt das Programm die Latenzwärme der Reaktion, die Oberflächenenergie und die geringe Viskosität von Mantelmaterial als weitere wesentliche Parameter in der Berechnung der Reaktionskinetic.

Das Wachstumsverhalten und die fraktale Dimension von errechneten Spinelkörnern ist dabei in guter Übereinstimmung mit Spinelstrukturen aus Hochdruckexperimenten.

Im zweiten Teil der Arbeit wird das Computermodell angewandt, um die Entwicklung der Oberflächenstruktur von Spinelkörnern unter verschiedenen Bedigungen zu eruieren.

Die sogenannte 'anticrack theory of faulting', die den katastrophalen Verlauf der Olivine→Spinel Umwandlung in olivinhaltigem Material unter differentieller Spannung durch Spannungskonzentrationen erklärt, wurde anhand des Computermodells untersucht. Der entsprechende Mechanismus konnte dabei nicht bestätigt werden. Stattdessen können Oberflächenstrukturen, die Ähnlichkeiten zu Anticracks aufweisen, durch Unreinheiten des Materials erklärt werden (Kap. 4).

Eine Reihe von Simulationen wurde der Herleitung der wichtigsten Kontrollparameter der Reaktion in monomineralischem Olivin gewidmet (Kap. 5 and Kap. 6). Als wichtigste Einflüsse auf die Kornform von Spinel stellten sich dabei die Hauptnormalspannungen auf dem System sowie Heterogenitäten im Wirtsminerals und die Viskosität heraus.

Im weiteren Verlauf wurden die Nukleierung und das Wachstum von Spinel in polymineralischen Mineralparagenesen untersucht (Kap. 7). Die Reaktionsgeschwindigkeit der Olivine→Spinel Umwandlung und die Entwicklung von Spinelnetzwerken und Clustern wird durch die Gegenwart nicht-reaktiver Minerale wie Granat oder Pyroxen erheblich beschleunigt.

Die Bildung von Spinelnetzwerken hat das Potential, die mechanischen Eigenschaften von Mantelgestein erheblich zu beeinflussen, sei es durch die Bildung potentieller Scherzonen oder durch Gerüstbildung. Dieser Lokalisierungprozess des Spinelwachstums in Mantelgesteinen kann daher ein neues Erklärungsmuster für Tiefbeben darstellen.

Abstract

The polymorphic, high pressure induced transition of olivine (α-phase) to spinel (β-phase) is an important candidate mechanism to explain the occurence of deep seated earthquakes at about 400 km depth in the upper mantle. It is yet still under debate how exactly the phase transition is related to the brittle failure of mantle material. Two important models have been lately proposed, which relate either the microstructural evolution of the olivine/spinel interface or the change of the rheology of mantle material induced by the transition to the mechanical failure. The examination of the role of the olivine→spinel transiton is completely dependent on theoretical kinetic considerations, high pressure experiments and numerical simulations.

It was a central aim of this thesis to develop a working computer model which can be applied in the simulation of microstructures formed by the olivine→spinel transition. An additional aim was the examination of the microstructural development of spinel grains and the controlling parameters of the transition.

The thesis is thus split into two major parts: In the first part (Chap. 2 and 3) the basic principles of the computer model for the simulation of the microstructural evolution of polymorphic solid-solid phase transitions is outlined, based on a combination of kinetic rate laws and non-hydrostatic, non-equilibrium thermodynamics. The model utilizes and extends an elastic normal spring network provided by the software *latte*, which is part of the software package *elle*.

The main driving force considered in the model is the stress on the olivine/spinel interface. In addition, the developed code considers other important parameters for grain growth under mantle conditions. These parameters are the latent heat release of the reaction, the surface energy on the olivine/spinel interface and the low viscosity of mantle material into the calculation.

The structural features of spinel grains resulting from the model are in good agreement with spinel structures observed in high pressure experiments. This applies to microstructures as well as the fractal dimension of the spinel phase.

In the second part the computer model is used to examine the structural evolution of spinel grains in olivine under varying conditions.

The so-called 'anticrack theory of faulting' was reviewed, which suggests a runaway of the olivine→spinel transition in olivine-bearing materials under differential stress due to stress concentrations. The suggested mechanism can not be verified by the computer simulations. Instead, structures resembling so-called anticracks are explained by the inherent disorder on elastic parameters of the host phase and the development of related surface structures (Chap. 4).

Several simulations are dedicated to the derivation of the control parameters of spinel growth in monomineralic olivine (Chap. 5 and Chap. 6). The main influence on the structure of spinel grains can be attributed to the principal normal stress which is applied to the system, the heterogeneity of the host phase and the viscosity of the host.

Further, nucleation and growth of spinel in polymineralic, olivine-bearing assemblages were examined (Chap. 7). The reaction rate of the olivine→spinel transition and the formation of spinel clusters and throughgoing spinel networks is considerably accelerated by the stress fields generated by the presence of non-reactive phases such as garnet or pyroxene in the assemblage.

The formation of throughgoing spinel networks has the potential to significantly alter the mechanical properties of mantle rocks, either by formation of potential shear zones or the formation of a real spinel framework. Since the so-called anticrack mechanism must be excluded as a possible reason for the mechanical failure related to deep seated earth quakes, this could turn out as a new candidate mechanism.

Contents

List of Tables

Nomenclature

D_b	Box-counting fractal dimension
D_M	Fractal mass dimension
D_S	Fractal surface dimension
ΔH_a	Activation enthalpy for growth
δ	Avrami length
δ_{Av}	Avrami length
ΔG^*_{hom}	Activation energy for homogeneous nucleation
ΔG_V	Free energy change of reaction per unit volume
δ_{ij}	Kronecker delta
D_{ij}	Strain rate tensor
E	Youngs modulus
η	Viscosity
f	Helmholtz free energy
γ	Interfacial free energy
G	Shear modulus
I^V	Homogeneous nucleation rate per unit volume
k	Boltzmann constant
K_0	Preexponential factor for nucleation rate

K	Bulk modulus
μ	Chemical potential
μ_d	Statistical mean
α	Constant for normal springs
P	Pressure
ϕ	Shape factor for heterogeneous nucleation
R	Gasconstant
$\sigma^{'}$	Deviatoric stress
$\sigma^{'}$	Deviatoric stress
$\bar{\sigma}$	Mean stress
σ_{ij}^{0}	Isotropic stress tensor
σ_{ij}	Stress tensor
σ_n	Normal stress
T	Temperature in Kelvin
τ	Avrami time
υ	Poisson ration
U_t	Strain energy
v_{HP}	Molar volume of the high pressure phase
v_{LP}	Molar volume of the low pressure phase

1 Introduction

1.1 Aim of the thesis

The thesis is about the computer simulation of microstructures formed by high pressure driven structural phase transitions and the determination of the critical parameters. The computer simulations were based on mineral data of the ultra high pressure olivine→spinel transition, motivated by the important role of this reaction in the discussion about mantle dynamics. This reaction is a prime example for a structural transition without compositional changes and with a distinct dependence on pressure.

The commonly assumed important role of the reaction in the dynamics of the earth's upper mantle led to the pronounced interest of various researchers (e. g. Akaogi et al., 1989, [2], Mosenfelder et al., 2001, [73], Rubie and Ross, 1994, [91], to name some). As a consequence - despite the technical difficulties in performing experiments under the ultra high pressures required by the reaction - a complete and easily accessible dataset of the relevant thermodynamic parameters is available.

It is a common assumption that the composition of mantle olivine is close to its pure Mg-endmember forsterite. Therefore the elastic and thermodynamic parameters used in the computer simulations are those of the pure forsterite endmember of olivine (α-phase, Mg_2SiO_4) and its high pressure polymorph wadsleyite (β-phase). The concentration on the endmember has the additional advantage that it undergoes a purely structural transition, in difference to the transition of solid solutions in the olivine system which are partly affected by compositional changes. The properties of the reaction will be described in Chap. 2.

The computer model is based on a combination of stochastic rate laws and non-equilibrium, non-hydrostatic driving forces to account for the inherent anisotropy of the process. The basis of the simulations is given by an elastic spring network, originally developed by Köhn et al. (2003, [61]) to model fracture processes. This program was extended to be able to model visco-elastic material behaviour and to include heat

conduction. A complete description of the simulation scheme is given in Chap. 3.

Experiments, calculated with this scheme, will be described in Chap. 4 to Chap. 7.

The focus of the experiments is on the structural evolution of spinel grains in different environments. This includes the localization of spinel growth in different olivine bearing assemblages and the derivation of the main control parameters of spinel structures.

1.2 Background

Various first-order phase transformations play a vital role in the dynamics and the evolution of the earth. The understanding of the microstructural development during such a first-order transition is important, since the effects of various physical processes, in particular in the geosciences, depend critically on the microstructures.

One field of special interest in this regard is the formation of deep-seated earthquakes, situated at approximately 400 km in the transition zone of the mantle, which have been assigned to the olivine→spinel transition since early after their first detection (Bernal, 1936, [10]).

Recent publications of Riggs and Green (2001, [88]), Green and Burley (1989, [40]) and Green and Houston (1995, [41]) report the finding of so-called anticrack structures of γ-olivine in an host of α-olivine (Fig. 2.3) in high-pressure experiments using Mg_2GeO_4 as an substitute for olivine.

These structures are believed to be Mode I features, preceding the brittle failure of the material. The suggested mechanism is thought to be an equivalent to conventional brittle shear failure, which succeeds the accumulation of Mode I microcracks (Lockner et al., 1991, [67]).

The supposed rapid growth of these spinel structures, triggered by the stress concentrations at their tips (Fig. 4.2) and assisted by latent heat release, leads to a catastrophic growth of the spinel phase, which in turn causes the brittle fracturing of the material by acting as a superplastic lubricant due to extremely fine grained spinel in these anticrack-lenses (Green et al., 1995, [41]).

This scheme could not be reproduced in the numerical simulations, nor does it stand an analytical treatment if the properties of Mg_2SiO_4 are taken into account. The topic is further discussed in Chap. 4. Structures of this type, observed in high-pressure experiments using germanates by Riggs et al. (2001, [88]) are depicted in Sec. 2.2.2.

Of special relevance in this thesis, considering the roughness of the product phase

in the high-pressure experiments mentioned above, is the development of the surface roughness of the product phase and the determination of the critical parameters.

Further, nucleation and growth of spinel grains in monomineralic and polymineralic assemblages is investigated. Mineral phases in polymineralic assemblages are assumed to be in agreement with the pyrolitic model for mantle material (Irifune, 1987, [45], Ringwood, 1975, [90]). A particular focus in this context is given to the network formation and clustering of spinel grains and the potential impact on the mechanical properties of mantle material.

1.3 Current model in comparison to existing computer models

1.3.1 Previous approaches to the problem

Although it would be ideal to have and employ analytical solutions for the microstructural development, such solutions don't exist even for the simplest case of constant PT conditions and constant rate and nucleation rates.

Noteworthy computer simulations employing rate equations were applied in 2D as well as 3D in works of e. g. Mahin et al., 1980, [69], Frost and Thompson, 1987, [32], Saetre et al., 1986, [93] and Riedel and Karato, 1996, [86]. All of these models are essentially based on the same idea, with important variations in details. Dimensionless nuclei are distributed randomly in a homogeneous single-phase matrix. Once formed, nuclei grow isotropically at a constant rate until impingement.

Several models were applied for the growth rate and the nucleation rate. Mahin et al., 1980, [69], assumed nucleation at the beginning of the transition coupled with constant growth rates as well as constant nucleation rates. Later refinements of e. g. Saetre et al. (1986, [93]) and Frost and Thompson (1987, [32]) include constant variations of the nucleation and growth rate dependent on time as well as the introduction of preferred nucleation sites. Riedel and Karato (1996, [86]) finally simulated the microstructural evolution of the olivine→spinel transition in the mantle and coupled the rate equations with a possible time evolution of the PT conditions in the subducted slab.

The intended purpose of these simulations vary from an interest in the evolving textures to the statistical examination of cluster size and grain size distribution and the percolation of the system.

Still, these simulations have several disadvantages regarding the concurrent evolution of grain shapes and the evolution of grain surfaces. In particular, these models cannot account for the local interplay between the evolving phase and the hostphase, which alters e. g. the stress field or the temperature gradient around a new grain considerably and introduces an element of self-organization into the growth characteristics. These models are further restricted to the case of homogeneous monomineralic systems, thus excluding the simulation of anisotropic grain growth and the effects of anisotropic textures within the host rock. Finally, they are restricted to generalized assumptions about the ambient parameters P and T or a predefined evolution of the kinetics of the system, and are therefore bound to the paradigm of hydrostatic stress.

1.3.2 This work

The computer simulation code employed and developed in this work is based on the combination of a spring network, giving full information about stress and strain at every node, with stochastic kinetic rate laws and non-equilibrium driving forces for solid-solid phase transformations. The simulations are based on the software *latte*, which was developed and described by Köhn (2006, [62], 2003, [61]) and comes combined with and as part of the microstructural simulation software package 'elle' (e. g. Jessel, 2001, [49]). Physical processes, which the original code corresponds to, are for instance the simulation of brittle fracturing of deformed materials or fluid-solid interactions in stylothites.

The original code applies a hybrid approach of a hexagonal central force elastic spring network and a discrete element (particle) network. (Fig. 3.2 and 3.1). The particle lattice is superposed to the spring network, using the same nodes, and allows therefore the combination of information about internal forces and the stress pattern of the system, with discretized material properties obtained from the particle code.

Evidently, this model does not intend to describe the material on an atomic basis, as for instance known from molecular dynamics, but has its validity at a much larger length scale, where the medium can be described by a vector fields of the internal movement of the material. Therefore one does not have to bother about realistic interatomic potentials, because the elastic equations of motion suffice.

In order to apply a statistical rate law to a volume element, the volume element must be large enough to contain a statistically significant number of atoms. For solids,

a few hundred ångström are sufficient (Stace, 1989, [95]).

This advantage, which led to the development of the model for the simulation of fracturing, applies equally to the simulation of grain boundary migration, the main topic of this work, and has been the main reason to choose the existing code as a basis for further development. In the context of the simulation of pressure driven grain boundary migration the *latte*-code serves as an excellent basis, mainly because of the potential to calculated a stress tensor for each discretized volume element combined with the possibility to treat these volume elements as thermodynamic subsystems, thus enabling the application of stochastical rate laws and therefore the calculation of local reaction velocities.

The combination of a spring network with a discrete element particle-code is capable to provide information about relevant kinetic factors besides stress, which can be included to the calculation of reaction rates, e. g. the change of the interphase surface energy for a discrete volume of material before and after the reaction or the elastic energy change.

The code has been expanded to include the time-dependent processes of viscous flow on geological timescales and heat conduction, in order to include the latent heat release of the reaction.

1.4 Structure of the thesis

Chap. 2 and Chap. 3 are about the reaction kinetics and the characteristics of the olivine→spinel transition as well as the principles of the computer model.

Chap. 4 to Chap. 6 focus on the spinel growth on small scales in the range of μm, in accordance with the scale of most high pressure experiments of the olivine→spinel transition.

Chap. 4 reviews the 'anticrack theory of faulting' on the basis of the developed program. The inconsistencies between the stress and displacement fields associated with the formation of spinel grains in olivine and the theory are described.

Chap. 5 concentrates on the simulation and examination of the control parameters for spinel growth. In order to isolate the relevant driving forces under 'clean room' conditions, the computer experiments apply a monomineralic, homogeneous olivine host. Chap. 6 extends these computer experiments to the more realistic case of an olivine host with an inherent disorder.

Chap. 7 finally simulates spinel growth on the scale of several centimeters, taking the whole assemblage into account.

2 Reaction kinetics and characteristics of the $\alpha \rightarrow \beta$ olivine transition

2.1 Overview

Two broad types of phase transformations can be distinguished, those that involve changes in composition, for instance because of unmixing of a solid solution phase, and polymorphic transformations, in which there is a change of symmetry but not of composition. Commonly only the latter process is termed a phase transition, in particular if the polymorphs are structurally related modifications.

Both transformation types are usually described by stochastic kinetic rate laws, although polymorphic transformations show a much closer dependency on local limiting parameters, which act directly on the migrating grain boundary, as for instance normal stress on a grain boundary or the local temperature. In contrast, transformations depending on changes of the chemical composition are additionally controlled by long range diffusion processes, therefore the state of the complete material, including parameters as for instance the porosity, have to be taken into account.

Most first-order and reconstructive phase transformations occur through a mechanism of nucleation and growth, where the new phase is initiated by a local fluctuation of the composition or the structure, the nucleus. This nucleus serves as a starting point from which the new grain boundary starts to migrate into the parent phase, thereby overcoming an activation energy. Grain boundary migration (GBM) continues until complete impingement with other grains of the same phase, or until the parent phase is exhauseted.

Structures formed by the $\alpha \rightarrow \beta$-olivine transition, observed in high pressure experiments with either Mg_2GeO_4-olivine or Mg-rich compositions of silicate olivine by various authors, are reviewed in Sec. 2.2.2 below.

The governing kinetic equations for high pressure phase transitions used in the avail-

able literature are usually formulated for hydrostatic conditions, using the scalar variable of the ambient pressure instead of the tensorial variable of stress. Other applications of essentially the same set of equations result in probability functions on the atomic scale, and are therefore useless in the geologically interesting calculation of rocks textures, which form on a much larger length scale and are oftenly strongly affected by anisotropic grain growth.

In Sec. 2.3 these equations will be modified for the application to non-hydrostatic and non-equilibrium situations, in order to be useful in the calculation of growth rates, given that the stress tensor and other limiting thermodynamically meaningful parameters are known. In addition equations for nucleation rates and grain size determination are given. The resulting set of equations was applied in the computer model.

2.2 Properties of the olivine→spinel reaction

2.2.1 Significance and occurrence

Olivine $(Mg, Fe)_2SiO_4$ and its high pressure polymorphs are the main constituent of mantle material in the widely accepted pyrolitic model developed by Ringwood (1975, [89]) and have been object of intense research during the past decades. The main interests in this respect are the impact of the density increase of mantle material, caused by the reaction, on mantle dynamics in general and in particular the explanation of the phenomenon of deep seated earth quakes along the Wadati-Benioff zone at extreme depth.

The mantle has major discontinuities at c. 400 and 670 km depth, observed by transitions in the calculated seismic velocities. The change in seismic velocity defines the separation of the mantle in upper and lower mantle and a related transition zone. Bernal (1936, [10]) was the first author to propose that the density increase associated with the increase of seismic velocities is a consequence of the mineral transition from $\alpha-(Mg, Fe)_2SiO_4$ (olivine) to either $\beta-$ (wadsleyite) or $\gamma-(Mg, Fe)_2SiO_4$ (ringwoodite). This proposal is today widely accepted (e. g. Irifune, 1987, [45], Putnis, 1992, [82], and others). Due to the experimentally confirmed correspondence of the discontinuities to the phase boundaries of olivine and its high pressure modifications and the similarities of the density increase of the mantle material to the density increase related to the reaction, it is widely considered reasonable to assume a causal relation between these

findings. Experimental data, justifying this assumption, have been provided by a variety of researchers, e. g. Akimoto and Fujisawa (1968, [3]), Suito (1977, [96]), Akaogi et al. (1989, [2], 1978, [1]), Green (1994, [41], 1989, [40]), Rubie and Ross (1994, [91]), Mosenfelder et al. (2001, [73]), to name a few.

Despite the wide acceptance of the pyrolitic mantle model some authors stated (e. g. Anderson and Bass, 1986, [5]), that the transition of olivine to its β- or γ-modification would occur over a considerable depth interval, causing a gradual increase of the seismic velocities rather than the observed abrupt increase. These authors claim additionally, that the magnitude of the seismic velocity increase caused by such a transition would be twice as high as actually observed. Anderson and Bass propose an alternate garnet-pyroxene dominated 'piclogite' composition for mantle rocks in the transition zone, composed of less than 30% olivine. The 400 km discontinuity itself is ascribed to a compositional boundary between the overlying peridotitic layers and the piclogite layer.

This alternate model is widely rebuted today and can be ascribed to the relative imprecise rheological and thermodynamic dataset available to these authors. Concerning the seismic velocity argument it was convincingly disproven by Bina and Wood (1987, [13]) and Irifune (1987a, [45] and 1987b, [46]).

2.2.2 Kinetic properties and microstructures

Microstructures observed in high pressure experiments

Due to the obvious technical difficulties in performing high pressure experiments with α/β-olivine and the main interest of researchers in thermodynamic datasets rather than in the grain topologies of the new phase, relatively little is known about the resulting microstructures. Most notable in this regard are the works of Riggs and Green (2001, [88]) and Vaughan (1984, [101]), who used Mg_2GeO_4 olivine as analogue substitutes for forsterite. Dupas et al. (1994, [25]) and Young et al. (1993, [106]) investigated microstructures using almost pure forsterite, refined from Lherzolites. All mentioned authors have been using materials refined from hotpressed powder as starting materials of the experiments. An unavoidable drawback of these experiments is the short timeframe, under which they have to be performed, and the resulting extreme strain rates exerted on the material, if compared to geological realistic times.

Vaughan et al. and Young et al. observed anisotropic growth textures in Mg_2GeO_4,

which appear whenever non-hydrostatic conditions are applied. The interphase boundaries between remaining olivine grains and spinel regions are highly irregular, displaying elongate fingers of spinel, separated by thin spikes of olivine, which wedge out into the olivine grains (Fig. 2.1). Young et al. (1993, [106]) observed similar structures on

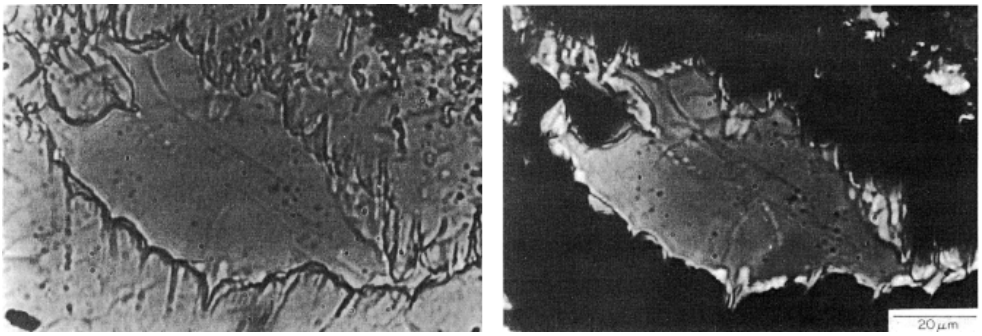

Figure 2.1: Optical micrographs of a non-hydrostatically compressed Mg_2GeO_4-sample, taken from Vaughan et al. (1984, [101]), depicting a residual olivine grain (center), surrounded by spinel. σ_1 is vertically oriented. Spinel fingers are developed along the grain interface, preferentially paralleling the σ_1-direction. On the right hand side the assemblage is shown under crossed nichols.

approximately the same system size in the presence of differential stress (Fig. 2.2), although the separating α-phase spikes are not as pronounced as in the experiments of Vaughan et al.

Green and Burnley (1989, [40]) and Riggs and Green (2001, [88]) focus in their Mg_2GeO_4-based experiments on elongated lenses, which develop normal to σ_1 at certain temperature conditions. These authors suggest these lenticulare structures to be micro-anticracks, using a term coined by Fletcher and Pollard, 1981, [29]. Some of these structures resemble flame structures, shown in Fig. 2.3, (a), while others give the impression of 'real' anticracks (Fig. 2.3, (b)).

An important feature, observed in the experiments of Dupas et al. (94, [25]) and applied throughout the simulation, is the property of the spinel phase to compensate impurities and point defects present in the olivine host phase, thus reducing the inherent disorder.

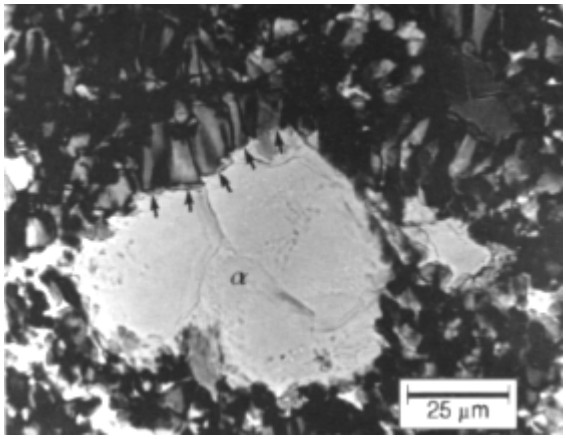

Figure 2.2: Optical micrograph of two large primary α-olivine grains in a spinel (β-olivine) matrix (Young et al., 1993, [106]). σ_1 is vertical. The grain size and the principal characteristics of spinel are similar to Fig. 2.1. The β-phase forms elongate grains, preferentially paralleling σ_1 and normal to the grain interface of the α-phase (black arrows).

Stability field and reaction mechanism

Equations used to calculate the rate of a reaction must be based on the relevant reaction mechanism. In case of the olivine→spinel transition, the transformation can occur by at least three different mechanisms depending on the PT conditions and the differential stress in the system.

If the transformation occurs under near-equilibrium conditions in one of the two-phase stability fields $\alpha + \beta$ or $\beta + \gamma$ (Fig. 2.4), the transformation involves compositional changes and is therefore likely to be controlled by the Mg - Fe diffusion in olivine and the coexisting high pressure phases (Rubie and Ross, 1994, [91]).

If the deviation from equilibrium is larger and the reaction occurs in the stability field of β- or γ- olivine, the transition does not involve compositional changes and is controlled by incoherent grain boundary nucleation and grain boundary migration (e. g. Akaogie et al., 1989, [2], Brearly and Rubie, 1994, [14], Mosenfelder, 2001, [73]).

Finally, if differential stresses are very high, a limited amount of the transformation to γ phase has been reported to be controlled by martensitic transformation (Green, 1989, [40], Burnley and Green, 1989, [16]), although the authors are not entirely sure of the transformation kinetics.

Reliable experimentally determined kinetic data are currently only available for the

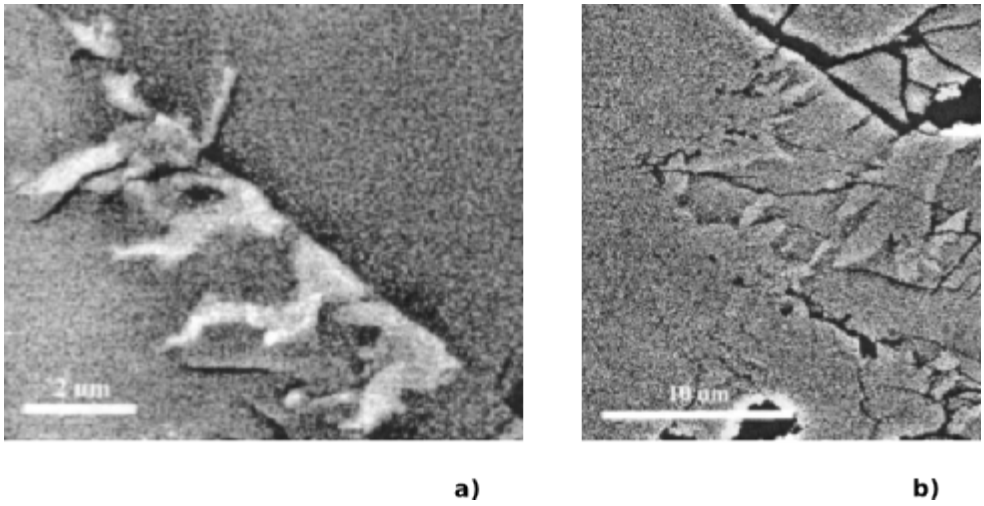

Figure 2.3: Microstructures obtained in laboratory experiments by Riggs and Green (2001, [88]) in non-hydrostatically compressed Mg_2GeO_4. (a) β-olivine flame structures (light color) on a nucleation site on a α-phase grain boundary. (b) Irregular grain boundary front of β-phase (left, high relief), overgrowing lenticular anticracks.

mechanism involving incoherent nucleation and interface controlled growth, which is also likely to be the dominant mechanism for the olivine→spinel transition in the upper mantle (Rubie and Ross, 1994, [91]). This mechanism the basis of a number of numerical models (DäSSler et al., 1996, [21], Riedl and Karato, 1996, [86]) and is widely used for the evaluation of kinetic data obtained from laboratory experiments (Akaogi et al., 1989, [2], Mosenfelder et al., 2001, [73]).

The phase diagram of olivine is well known (e. g. Akaogie et al, 1989, [2], Ito and Takahashi, 1989, [48], cp. Fig. 2.4). The stable phase at low pressures is orthorombic olivine (α-phase), which transforms with increasing pressures subsequently into its β-polymorph (wadsleyite) and its γ-polymorph (ringwoodite). Only the endmembers forsterite and fayalite of the solid solution undergo a purely structural transition without changes in composition.

Since the computer program is restricted to the mechanism of structural phase transitions, where diffusion occurs only across the grain boundaries and a change of composition is not involved, the mineral data of pure Mg_2SiO_4, the forsterite endmember, was applied in the simulations. Preferring pure forsterite over some solid solution is a common simplification to all types of model calculations for this reaction, since

the average composition of mantle olivine is commonly estimated to be approximately $(Mg_{0.92}, Fe_{0.02})_2SiO_4$ (Dupas, 1994, [25], Ringwood, 1975, [90]), and is thereby close to the composition of pure forsterite.

The critical pressure for a reaction can be calculated for an arbitrary temperature, using the equation ((cp. Fig. 2.4(a))):

$$P_e = P_o + T \cdot \frac{dP}{dT}. \tag{2.1}$$

Parameters for the Clapeyron constant P_0 and the Clapeyron slope dP/dT for the $\alpha \rightarrow \beta$ transition of olivine are given in Appendix C.

The $\alpha \rightarrow \beta$-olivine reaction is presumed to occur under fluid-absent conditions in the earth's mantle, which is confirmed by the occurrence in the presumably fluid-absent center of subducted lithosphere (Green and Houston, 1995, [41]). The existing high pressure experiments appear to confirm the assumption, since the derived thermodynamic datasets for dry materials sustain a transition at a depth in accordance with the observed 410 km seismic discontinuity.

Dry conditions are a relevant feature of the reaction, as far as the direct applicability of the reaction kinetics given below to the computer model is concerned, since the simulations do not take long-range diffusion processes, oftenly triggered by the presence of fluids, into account.

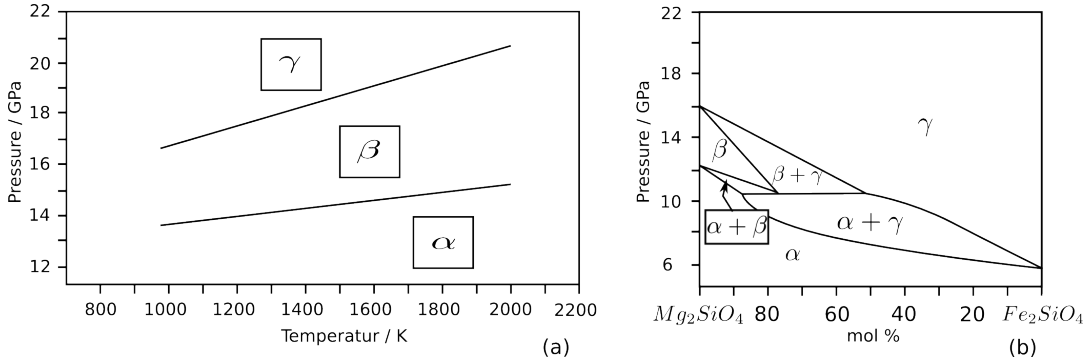

Figure 2.4: (a) Stability fields of pure Mg_2SiO_4. (b) Phase boundaries of the solid solution $Mg_2SiO_4 - Fe_2SiO_4$. Only the endmembers of the solid solution undergo a purely structural phase transition without a change in composition.

2.3 General reaction kinetics

In the following, the stochastic kinetic rate laws for nucleation and growth under hydrostatic pressure will be outlined. The growth rate function is of particular interest to the model and will receive a somewhat more elaborate treatment. Subsequently, the non-hydrostatic, non-equilibrium driving force in poly-mineralic, isochemical solids will be derived and the relevant equations for the computer simulation will be given.

Further, as far as necessary, the formulas used for the calculation of stresses and energies are given and possible coupling effects will be briefly mentioned, if not given in Chap. 3.

2.3.1 Stochastic kinetic rate laws

Energetic effects related to phase transitions

Some energies may be released while others may be absorbed during phase transitions. This is true for the system in total as well as the vicinity of the transformed volume element. The total energy change due to a phase transition can be expressed by (Sung and Burns, 1976, [97]):

$$\Delta G_T = \Delta G + \Delta\gamma + \Delta U_t + \Delta E^h \tag{2.2}$$

where G is the Gibbs free energy release, E^h is what Sung and Burns termed the 'energy of heterogeneity', caused by impurities, point defects, the inherent disorder of the system etc., γ is the surface energy introduced by the new grain boundary and U_t is the strain energy. U_t can be further subdivided into the shear strain energy introduced by application of high pressure (E^d) and the energy created by the difference in volume and elastic parameters between the two phases (ξ).

In kinetic theory a phase change is supposed to be associated to an energetic barrier that has to be overcome in order to transform a phase from an initial to a final state (Fig. 2.5).

Growth rates

In growth processes, the only energy barrier that has to be overcome is the activation energy (ΔH_a), which is encountered when atoms diffuse across the grain boundary and

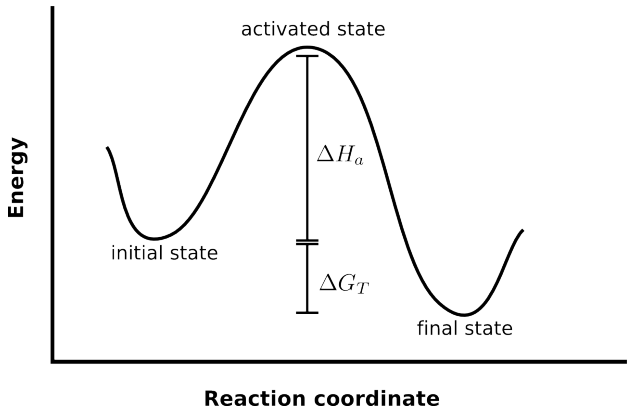

Figure 2.5: Sketch of the energy change for a mineral transformation from an initial to a final state.

attach to the new interface. Application of Boltzmann statistics leads to the following wellknown equation for growth rates (Dowty, 1980, [24], Putnis, 1992, [82])

$$Y_{att} = K \exp\left(-\frac{\Delta H_a}{RT}\right). \tag{2.3}$$

Atoms detaching themselves from the new phase in a back reaction must overcome the same activation energy plus the energy difference between the two states, thus

$$Y_{det} = K' \exp\left(-\frac{\Delta H_a}{RT}\right) \cdot \exp\left(-\frac{\Delta G}{RT}\right). \tag{2.4}$$

Combing Eqs. 2.3 and 2.4 gives the net growth rate Y, which is usually given in the form

$$Y = Y_{att} - Y_{det} = K'' \exp\left(-\frac{\Delta H_a}{RT}\right) \cdot \left(1 - \exp\left(-\frac{\Delta G_T}{RT}\right)\right). \tag{2.5}$$

After introduction of a preexponential factor accounting for heat energy we have

$$Y = Y_0 T \exp\left(-\frac{\Delta H_a}{RT}\right) - K' \exp\left(-\frac{\Delta H_a + \Delta G}{RT}\right), \tag{2.6}$$

which allows the further elaboration of the energies on both sides of the term. The energies contributing to ΔG_T in Eq. 2.2 can now be added to the enumerator in the exponential of each side according to their signs. This is usually done for a thermody-

namic system under hydrostatic pressure by (Sung and Burns, 1976, [97])

$$Y = Y_0 T \left[\exp\left(-\frac{\Delta H_a + \xi + \gamma}{RT} \right) - \exp\left(-\frac{\Delta H_a - \Delta G - E^d - E^h}{RT} \right) \right], \tag{2.7}$$

where we can safely assume positive signs for the addends in the enumerator in the exponential on the left, and negative signs for the addends on the right.

However, Eq. 2.7 can not be applied to a discrete high resolution system as applied in the computer model, where the growth rate calculations are performed for a particular local volume element under differing types of stress and under changing geometric situations of the particular volume element on a given grain boundary. The generalized equation, as used in the program, is just

$$Y = Y_0 T \left[\exp\left(-\frac{\Delta H_a + \sum E_{pos}}{RT} \right) - \exp\left(-\frac{\Delta H_a - \Delta G - \sum E_{neg}}{RT} \right) \right], \tag{2.8}$$

where E_{pos} and E_{neg} represent arbitrary energy term, that is included in the particular simulation.

Further, ΔH_a is not a constant but becomes pressure and temperature depend upon inclusion of the activation volume $V^*$and via setting the activation energy as a function of temperature. The pressure dependence can be introduced by application of the van't Hoff law for the reaction isotherme with (e. g. Langbein, 1999, [63], DäSSler, 1994, [21], Rubie and Ross, 1994, [91])

$$\Delta H_a = PV^*. \tag{2.9}$$

The pressure dependence of the activation volume can be formulated after a model of O'Connel (1977, [76]), in which the activation volume is considered to be equal to the formation volume of a vacancy and the vacancy is considered to be a cavity in a solid under pressure, by

$$V^* = V_0^* \left(1 + \frac{PK_c^{'}}{K_c} \right)^{-1/K_c^{'}}. \tag{2.10}$$

V_0^* is the activation volume at zero pressure, K_c is the effective bulk modulus of the cavity and $K_c^{'}$ is the pressure derivative of K_c.

Temperature dependence of the activation energy is given by

$$\Delta H_a = \alpha_m T_m, \tag{2.11}$$

where T_m is the melting temperature of olivine at 1 bar and α_m is a constant (Frost and Ashby, 1982, [33]). Values for α, K_c and $K_c^{'}$ are listed in Appendix C.

Nucleation rates

The nucleation rate I^V as a function of temperature T and pressure P for unit volume is given by (Dowty, 1980, [24]):

$$I^V = I_0 T \exp\left(-\frac{\Delta G^*_{hom}(P,T)}{kT}\right) \times \exp\left(-\frac{\Delta H_a(P,T)}{RT}\right) \tag{2.12}$$

where ΔG^*_{hom} is the activation energy for the formation of a stable nucleus, K_0 is a constant and ΔH_a is the activation energy for growth. ΔG^*_{hom} is given by (e. g. Putnis, 92, [82]):

$$\Delta G^*_{hom} = \frac{16\pi\gamma^3}{3\left(\Delta G_v + U_t\right)^2} \tag{2.13}$$

where γ is the interfacial free energy, ΔG_V is the free energy change due to the reaction per unit volume and U_t is the strain energy of a nucleus. As a common simplification, the strain energy U_t is usually assumed to be zero (e. g. DäSSler et al., 1996, [21], Riedl et al., 1996, [86]), which corresponds to the case where the volume change due to the transformation is compensated by ductile flow rather than by elastic strain.

Pressure and temperature dependence of ΔG^*_{hom} is achieved with (Däßler, 1996, [21])

$$\Delta G_V = \Delta V \cdot \Delta P(T) - \Delta S \cdot \Delta T(P) \tag{2.14}$$

where ΔT and ΔP are the undercooling and the overpressure with regard to equilibrium conditions.

ΔG^*_{hom} can be further refined for heterogeneous nucleation on grain boundaries and edges by a shape factor ϕ, yielding

$$\Delta G^*_{het} = \phi \Delta G^*_{hom} \tag{2.15}$$

(Christian, 1981, [18]).

2.3.2 Grain size, nucleation sites and transformation time

The average grain size of rocks usually changes after a phase transformation (Karato, 2003, [52]). The physics behind this lies in the mutual interplay of nucleation and growth during the ongoing deformation. Once nucleated, grains of the new phase will grow and impinge on each other until the transformation is completed. If the nucleation rate is high in comparison to the growth rate, the number of grains will be large with a small average grain diameter and vice versa.

It is well established, that the model of nucleation and growth, as applied here, has an exact dimensional scaling, following from the observation that I^V (usually given in m^3/s) and Y (usually given in m/s) permit the definition of natural length scales. The average grain size and the half time needed for the transformation in 3D can thus be estimated by the so-called Avrami length δ and the Avrami time τ, using the rate for volume nucleation (I^V) and for growth (Y), by (Axe and Yamada, 1986, [8], Riedel and Karato, 1997, [87])

$$\delta = \left(\frac{I^V}{Y}\right)^{-1/4} \tag{2.16}$$

and

$$\tau = \left(I^V Y^3\right)^{-1/4}. \tag{2.17}$$

Combining Eq. 2.16 and Eq. 2.17 yields

$$\delta = Y\tau. \tag{2.18}$$

Adapting Eq. 2.16 to two dimensions gives

$$\delta_{2D} = \left(\frac{I^B}{Y}\right)^{-1/3}. \tag{2.19}$$

Eq. 2.19 was actually applied in the program, if polymineralic rocks where simulated. In this case I^B, the nucleation rate on grain boundaries, must be considered to be a more realistic parameter than I^V, since nucleation usually occurs along grain boundaries and edges. A realistic pattern of nucleation sites would thus resemble Fig. 2.6. I^B can be related to I^V by

$$I^V = I^B \cdot^v O^B \tag{2.20}$$

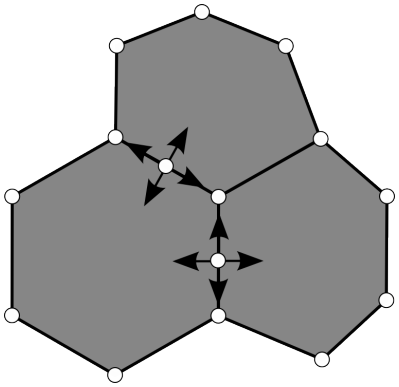

Figure 2.6: Nucleation on grain boundaries, controlled by the refined nucleation rate I_B, Eq. 2.20.

where ${}^vO^B$ is the grain boundary area per unit volume of the reactant phase (Christian, 1981, [18]). The probably most realistic simplifying assumption for the calculation of ${}^vO^B$ is to consider all grains as tetrakaidecahedra, which were mathematically treated by Kelvin (1887, [56]). The grain boundary area ${}^vO^B$ is then given by

$$ {}^vO^B = \frac{3.35}{L_B} \tag{2.21} $$

where L_B is the separation of square faces (which is set to the mean grain diameter) and depends on the number of grains per unit volume (n_B) with

$$ n_B = \frac{2}{(L^B)^3} \tag{2.22} $$

Using these equations and ignoring the change of the grain boundary area due to the addition of new grains as well as a probable time evolution of the PT-conditions during the ongoing phase transition, we can give an estimate of the average grain size after the transformation. This principle will be extensively applied in the nucleation scheme of the computer simulations (Chap. 3.4.1).

2.3.3 Driving forces under non-hydrostatic conditions

Classical thermodynamics as applied above is not directly applicable to non-hydrostatic systems, since the scalar variable of pressure, P, as used in kinetics and equilibrium

thermodynamics, can not be replaced by the tensor variable of stress (σ_{ij}). It is therefore a conventional way in dealing with nonhydrostatic states to replace the pressure by the mean stress as a first approximaiton (Fitts, 1962, [28]). The stress tensor can be split into two parts (e. g. Ranalli, 1995, [84]):

$$\sigma_{ij} = \sigma_{ij}^{'} + \sigma_{ij}^{0} \tag{2.23}$$

where $\sigma_{ij}^{'}$ is the deviatoric stress tensor and σ_{ij}^{0} the isotropic stress tensor. The isotropic stress is defined as

$$\sigma_{ij}^{0} = \delta_{ij}\bar{\sigma} \tag{2.24}$$

with Kronecker delta δ_{ij}. Finally, the scalar variable of mean stress ($\bar{\sigma}$) is defined as

$$\bar{\sigma} = \frac{1}{3}\sigma_{kk}, \tag{2.25}$$

where indices kk denote the elements on the main diagonal of the stress tensor. However, application of this scalar to anisotropic growth in a solid under stress fails, since it does not reflect the orientations-dependence of the reaction velocity, given by the stress tensor.

Instead, Gibbs (1906, [36]) was the first author who proposed the application of the equally scalar variable of the normal stress (σ_n) on a given grain boundary. Averaged over all possible orientations of a grain boundary, this would give the mean stress again and does thus not alter the overall growth rate of a given system. This idea was further elaborated by e. g. Shimizu (1992, [94]), who derived a driving force for grain boundary migration from this assumption (Fig. 2.7), given by

$$\Delta\mu = -\sigma_n \Delta v + \Delta f. \tag{2.26}$$

$\Delta\mu$ is the the difference in the chemical potential between the two phases (i. e. the Gibbs free energy per mole) and Δf the difference in free Helmholtz energy, which includes contributions of the surface and the elastic energy, if the solid behaves elastic.

$\Delta\mu$, as it appears in Eq. 2.26 can not be applied to a stochastic rate law, since it does not take the pressure decrement caused by the transformation into account, as it is applied in kinetics. Thus, applied to the kinetic rate laws used in this work and under the idealizing assumption of equilibrium conditions after the transformation, the

driving force has to be regarded as the difference between the actual pressure and the equilibrium pressure, giving

$$\Delta G = -(P_E - \sigma_n)\Delta v \,[+\Delta f]\,. \tag{2.27}$$

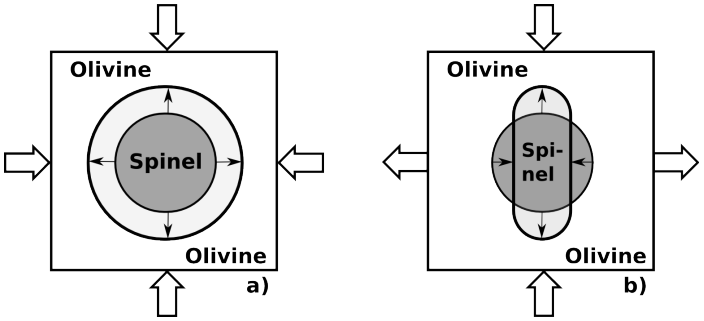

Figure 2.7: Grain growth direction under non-hydrostatic conditions. Thick black arrows indicate the direction of $\sigma_n - P_E$, where P_E is the equilibrium pressure for the reaction at a given temperature. (a) Under uniform hydrostatic pressure with $\sigma_1 = \sigma_3 > P_E$, growth of the high pressure phase occurs in all directions. (b) Under the condition $\sigma_1 > P_E > \sigma_3$, growth of the high pressure phase occurs in the σ_1-direction only, while a back reaction occurs on the σ_3 direction.

2.3.4 Resulting rate equation

Putting the pieces together for a rate law for growth under non-hydrostatic, non-equilibrium conditions and taking care of the positive and negative contributions to the net growth rate, we can finally define a vectorized growth rate $\vec{Y}$ for an arbitrary point on a grain boundary with

$$\vec{Y} = Y_0 T \exp\left(-\frac{\Delta H_a + \sum E_{pos}}{RT}\right) - \exp\left(-\frac{\Delta H_a + (P_E - \vec{\sigma_n})\Delta v - \sum E_{neg}}{RT}\right) \tag{2.28}$$

for a negative ΔG (ol→spin) and

$$\vec{Y} = Y_0 T \left[\exp\left(-\frac{\Delta H_a - (P_E - \vec{\sigma_n})\Delta v + \sum E_{pos}}{RT}\right) - \exp\left(-\frac{\Delta H_a - \sum E_{neg}}{RT}\right)\right] \tag{2.29}$$

for positive ΔG (spin→ol). $\vec{Y}$ is oriented normal to the grain boundary. The normal stress is treated as a vector for this purpose (Fig. 2.8), so that σ_n from Eq. 2.26 and Eq. 2.27 on an arbitrary point, situated on the grain boundary, equals $|\vec{\sigma_n}|$. Eq. 2.28 was applied in the subroutine for grain growth in the computer program.

2.3.5 Volume reduction, heat capacity and latent heat release

Volume reduction and heat capacity

The reduction of the molar volume (v), related to the phase transition, can be calculated using the thermodynamic data of Akaogi et al. (Tab. C.3 and Tab. C.4) with:

$$\alpha = a + bT + cT^{-2} \tag{2.30}$$

and

$$v = v_0 \cdot e^{\alpha}. \tag{2.31}$$

The heat capacity of the material is given by:

$$C = A + BT^{-0.5} + CT^{-2} + DT^{-3}, \tag{2.32}$$

where the dataset for the parameters is again listed in Appendix C.

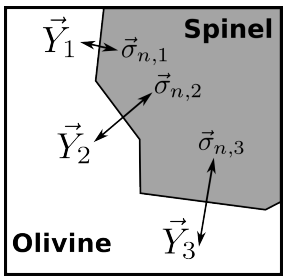

Figure 2.8: The orientation of the normal stress on an olivine/spinel interface and the vectorized growth rate $\vec{Y}$, as used in Eq. 2.28.

Temperature increase

The amount of thermal energy, released due to the reaction, can be calculated depending on temperature and pressure of the material with

$$\Delta H_{T,1bar} = \Delta H_0 + \int_{T_0}^{T} \Delta C_0 dT \tag{2.33}$$

and

$$\Delta H_{T,P} = \Delta H_{T,1bar} + \int_{1bar}^{P} \Delta V_{T,P} dP. \tag{2.34}$$

ΔV and C are given by Eq. 2.32 and Eq. 2.31. The actual increase in temperature in the transformed material can be calculated with

$$\Delta T = \frac{T \cdot C_{Ol} + \Delta H_{T,P}}{C_{spin}} - T. \tag{2.35}$$

Fig. 2.9 shows the dependence of the released heat energy on the initial heat and the resulting temperature increase, using Eq. 2.33, Eq. 2.32 and Eq. 2.35. The influence of the pressure on the new temperature is vanishingly small and has been omitted in this context.

Thermo-kinetic coupling The increase of the temperature of the material due to the temperature-dependent latent heat release, heat capacity and volume change related to the olivine→spinel transition (Fig. 2.9) serves as a good example for several kinetic coupling processes in the system.

The exothermic properties of the olivine→spinel are frequently taken into account as a viable explanation for the assumed run-away of the reaction in the upper mantle (Green and Burnley,1989,[40], Young et al.,1993,[106], Däßler et al., 1996,[21]), since the rates for nucleation and growth are in turn significantly controlled by heat energy in addition to their apparent high pressure dependence (cp. Eq. 2.8, 2.12 and 2.14).

In the context of the evolution of microstructures, the main interest in this work, the latent heat might be responsible for localisation effects of the growing mineral phase. This is further discussed in Sec. 3.3.

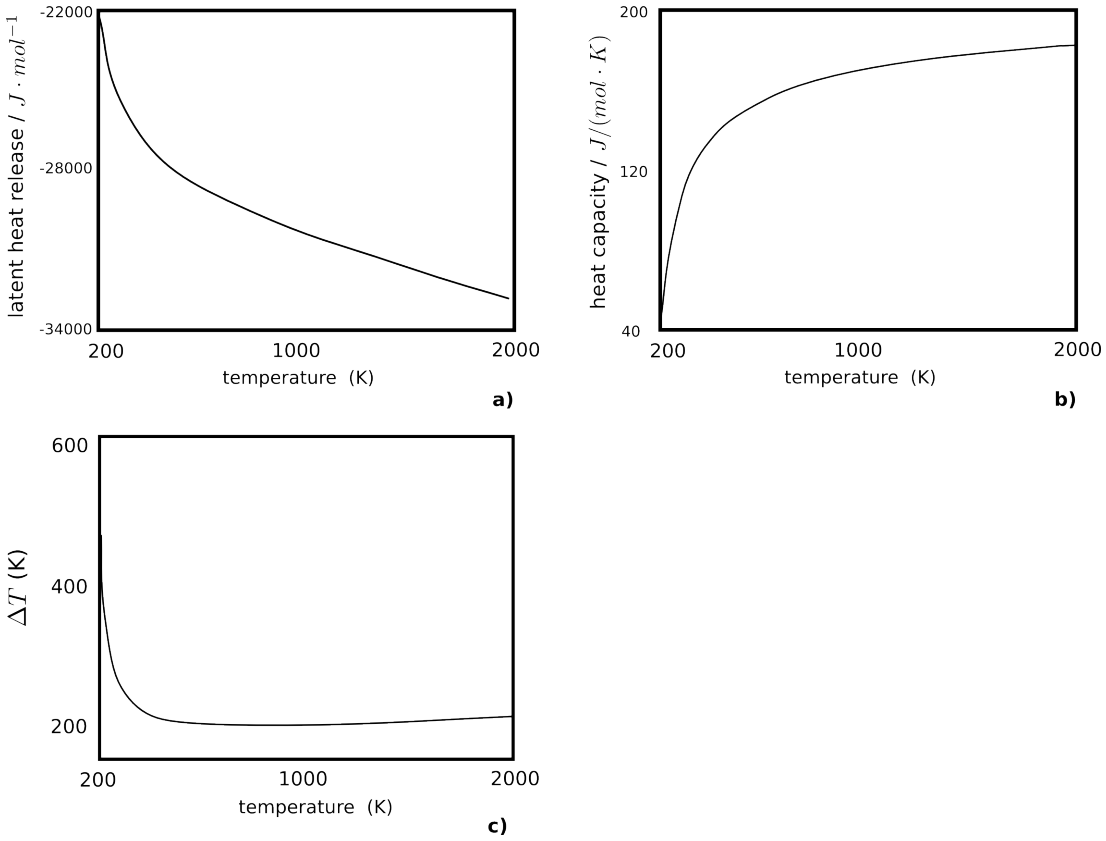

Figure 2.9: (a) Latent heat release of the ol→spin reaction at fixed pressure 12.5 GPa. (b) Heat capacity of olivine with temperature. (c) Temperature increase under consideration of the change in the heat capacity and the latent heat release at 12.5 GPa for the reaction after Eq. 2.33, 2.34 and 2.35. The effect of pressure on the temperature change is neglectible and has been omitted.

3 Description of the numerical model

3.1 Brief description of the program flow

It is the intention of this paragraph to give a brief summary of the basic idea of the program flow. A further discussion of, e. g., the properties of the normal spring network lattice will take place in the following sections.

The basis of the model is given by a two-dimensional material representation, which utilizes a combination of a hexagonal normal spring network, based on the work of Malthe-Sørenssen et al. (1998, [70]) and implemented by Köhn et al. (2003, [61]), with a discrete element network. This setup is combined with a finite difference network (cp. Fig. 3.3 and Fig. 3.2). This way linear elastic behaviour, including a full description of the stress and strain field, can be simulated and combined with a discrete description of the material properties as well as - eventually - viscoelasticity and thermal conduction.

In a nutshell, the general flow of the program is as follows: the initially undeformed material is progressivly deformed with a constant displacement rate by either uniaxial/biaxial compression in x- or y-direction or by simple shear paralleling the x-axis (Fig. 3.3). Combinations of these deformation mechanism are possible and frequently applied.

The boundary condition is either given by fixed spatial coordinates of the lattice boundaries, which are subjected to the externally applied progressive deformation only, but not affected by the relaxation process, or by wrapping of the side-walls in combined with fixed top and boundary walls, in order to diminish boundary effects on the stress field. The choice of the actual boundary condition depends on the necessities, given by the external deformation. The topic will be adressed in Sec. 3.2.1.

The simulated material may be either a homogeneous or heterogeneous one-component system, where homogeneity and heterogeneity relate to a Gauss normal distribution on the mechanical properties of the spring network in order to simulate the inherent disor-

der. Another type of heterogeneity is created by the introduction of more-component system, which include grains of non-reactive phases with differing rheological parameters, in order to achieve a closer resemblance of the model with real rock textures.

The simulation of grain boundary migration can either focus on the development of textures. In this case the simulation has to include the independent kinetic processes of nucleation of the new phase and subsequent growth until impingement. Nucleation occurs only once, after the critical pressure - defined by the phase boundary of the olivine→spinel reaction - is reached.

In addition to using nuclei as starting points for grain boundary migration, arbitrary initial olivine/spinel phase-boundaries can be defined and grain boundary migration will commence from there. This procedure was applied in a number of simulations, in order to examine the evolving surface structures on very small scales. A discussion of nucleation routines is given in Sec. 3.4.1.

Once nucleation occurred, the system is supposed to be dominated by grain boundary migration. For olivine particles, which are situated on grain surfaces, the growth rates of the spinel phase is calculated, and vice versa for spinel particles (Fig. 3.10). The particle with the lowest computed time until its complete transition will be transformed. The process is repeated until the transformation is finished, i. e. the α-phase is exhausted.

The transition of a particle to the new phase is simulated by resetting the mechanical and thermal properties of the particle area to parameters defined by the new phase and a recalculation of the energetic state of the complete system, caused by the local energy release or consumption. This includes thermal and surface energies, normal stress on the grain boundary and the change in strain energy.

Except for the driving force $\Delta\sigma_n\Delta v$, the main reason for grain boundary migration in general and for anisotropic growth rates in particular, the energies to be taken into account in an individual simulation can be arbitrarily selected at the beginning of every run. This enables the experimentator to analyze the influence of specific parameters on the reaction or simply to save computation time, if the expected influence of a specific energy is neglectible for a certain system size.

If thermal energy is considered in a simulation run, the temperature distribution due to the latent heat released will be calculated on basis of a finite difference lattice. In addition, besides a purely elastic regime, viscous flow induced by non-hydrostatic stresses can be taken into account.

3.2 Calculation of driving forces on the spring network

3.2.1 Internal stress modeling

Elastic spring network

In order to obtain a numerically tractable representation of the internal stresses of the strained and partly transformed material, a central force spring model as described by Malthe-Sørenssen et al. (1998, [70]) and Koehn et al. (2003, [61]) has been applied and extended. In this type of numerical simulation the medium is reduced to a set of points, embedded in a grid, which are connected by hookean linear elastic mechanical elements (Fig. 3.1 and 3.2).

In case of composite materials the network represents a discretization of continuum phases with the springs adjusted locally according to the specific elasticity tensors of all the phases.

In the central force model each elastic spring can rotate freely around the node it is attached to.The net force acting on every node can be calculated from

$$f = \sum_i \alpha(|\vec{l_i}| - |\vec{x}_0 - \vec{x}_i|), \tag{3.1}$$

where the sum is over all connected neighbours i. $\vec{l}$ is the vector between the two nearest neighbour nodes in undeformed equilibrium and x_0, x_i denote their current positions after deformation, α is the internal spring constant, similar to the Youngs modulus in a real material. Thus, for the two dimensional triangular case as depicted in Fig. 3.2, the equilibrium position of every node with regard to its six next neighbours can be calculated as the sum of 6 vectorial force equations. The final solution for the total system is obtained by a standard overrelaxation algorithm (e. g. Allen, 1954, [4] or Davies, 1980, [22]), which is repeated until the movement of the nodes is below the value of a predefined relaxationthreshold.

The model is coupled with a discrete element material representation, termed a particle model, where the mechanical and thermodynamic parameters of the material are attributed to finite sized circular elements with the configuration of the spring network (Fig. 3.2).

The general setup of the two-dimensional simulations is a square box. Depending on the deformation type, the boundaries of the system can be fixed. Alternatively,

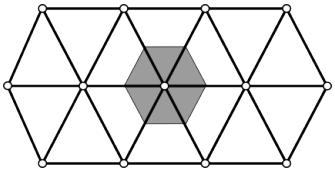

Figure 3.1: Idealized hexagonal unit cell of the triangular spring network. The simulations approximate the hexagonal unit cells with circular particles (cp. Fig. 3.2).

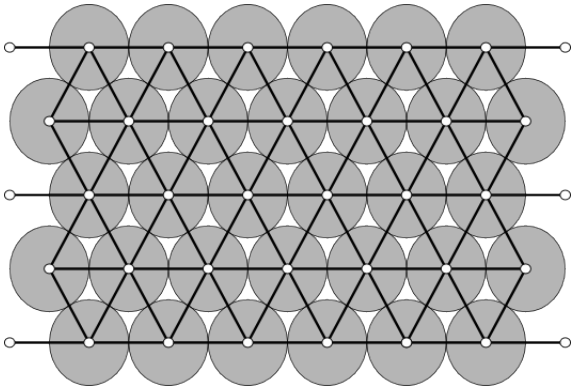

Figure 3.2: Schematic drawing of the triangular elastic spring network, superposed on the discrete element network.

wrapping across the right and left system wall can be utilized, meaning that the nodes of either side of the elastic lattice are seamlessly connected to those on the other side while top and bottom boundaries are fixed. In order to stress the system, the upper and the right wall can be moved depending on the required deformation type. Through this setting all major types of deformation can be achieved. The strain on the system can be either linear uniaxial or linear volumetric, by pushing the left or top wall inward at a constant rate and thus generating hydrostatic or uniaxial stresses. In addition, simple shear can be simulated by moving the top wall in x-direction.

While fixed walls are a sufficient boundary condition in case of an exclusively axe parallel externally applied deformation, the change of the angle between the lattice boundaries during simple shear deformation leads to stress concentrations along the side walls if they are constrained, a problem well known from simple shear analogue experiments. In the simulation setup this problem can be circumvented by the wrapping algorithm mentioned above. In addition, any combination of the beforementioned

strain schemes is possible, enabling e. g. the application of volume constant pure shear to the system (cp. Fig. 3.3 for an overview of the available basic deformation mechanisms).

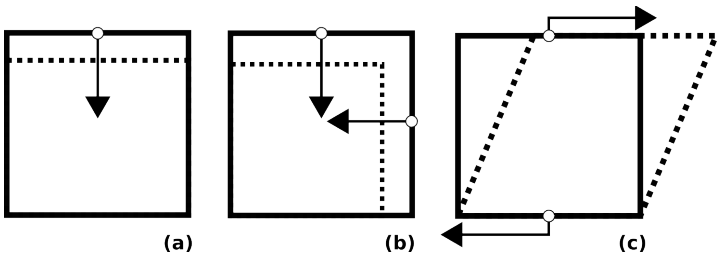

Figure 3.3: The three basic ways of imposing an external strain on the elastic spring network; (a) uniaxial compression; (b) volumetric compression; (c) simple shear. Depicted are the boundaries of the system. Combination of these deformation schemes leads to more complex strains.

In difference to the original intention of spring networks, the study of fracturing processes, the application to phase transitions does not include the breaking of springs, and does therefore not allow the direct direct observation of transition related fracture processes. The main reason for this shortcoming is an enormously complicated application of the grain growth routine and the study of the heat flow in the system, after bonds are removed from the network and gaps come into existence.

Visco-elastic spring network

In a number of simulations the purely elastic material behaviour was replaced by visco-elasticity, in order to simulate the stress field caused by a progressive deformation in presence of hard and/or soft bodies, i. e. grains of non-reactive minerals, and the effect of the material flow on the stress field in the material and subsequently on the preferred growth orientation of the β-phase.

In difference to purely elastic behaviour, viscous flow is a time-dependent process which does not sustain shear stress. The viscous effect of shear strain imposed on a body is therefore a time-dependent, principally irreversible change of the configuration of the body, until the shear stress and the deviatoric stress is zero and the body achieves a state of rest.

In the spring-network this goal is achieved through the coupling of a purely elastic with a subsequent purely viscous relaxation process, where the deviatoric stress tensor

at every node is given by the forces in elastic equilibrium. The basic scheme for the simulation of viscous flow is the distortion of the unit cells of the elastic lattice, in order to adjust the geometrical configuration of the network according to the induced viscous strain. This is accomplished by adapting the internal equilibrium length of the springs at every node of the spring lattice to the local deviatoric stress tensor and a predefined timestep. Using the area conserving scheme for particle path calculations under plane strain, as given by Ramberg (1975, [83]), this results in a change of the lattice geometry without changing the total or the unit cell areas.

Creep in minerals under mantle conditions is generally assumed to follow a flow law of the general form

$$\dot{\epsilon} = A \cdot \left(\sigma^{'}\right)^{n} \cdot d^{m} \cdot \exp\left(-\frac{Q}{RT}\right), \tag{3.2}$$

where A is a preexponential factor, d is usually the fugacity of some consitutent of the mineral, Q the activation energy for creep and $\sigma^{'}$ the deviatoric stress (King, 1995, [58]). Parameters for the above equation, incorporating diffusion and dislocation creep, are given in Appendix C.3 for various mantle materials. Since Newtonian viscosity is defined as

$$\eta = \frac{\sigma^{'}}{\dot{\epsilon}}, \tag{3.3}$$

creep can be directly linked to the flow scheme as described in Appendix A if the deviatoric stress and the temperature of a material are known.

Billen et al. (2005, [11]) and Gölke et al. (1994, [37]) derive values for linear η under the strain conditions of the upper mantle, based on the simplifying assumption of olivine being the only constituent of mantle material. They derive values for η between c. $10^{19}\ Pa \cdot s$ to $10^{22}\ Pa \cdot s$, depending on the assumed strain rate and active creep mechanisms. In the following simulations we will assume $10^{22}\ Pa \cdot s$, the upper limit of the given range, to be the effective viscosity of the olivine phase, mainly to avoid an over-evaluation of olivine-flow on the structural development.

Olivine is assumed to be considerably weaker than other mantle minerals (e. g. Karato and Wu, 1993, [55], Gueguen and Nicolas, 1980, [42]). For reasons of computational simplicity, the viscosity η of minerals other than olivine is considered to be infinite in the simulations.

Since flow in geomaterials is only relevant on large timescales, while a phase transition on the regarded system sizes occurrs relatively fast, the viscousity algorithm is

disabled after the phase transition started in order to save computation time.

Mechanical properties and heterogeneities of the spring network

Basic mechanic lattice parameters The spring constant α is related to the planar bulk and shear modulus by (Grah et al., 1996, [39])

$$G = \frac{1}{2\sqrt{3}}\left(\frac{3}{4}\alpha\right) \qquad K = \frac{1}{2\sqrt{3}}\left(\frac{3}{2}\alpha\right) \tag{3.4}$$

The equation for planar Poisson's ratio is (Thorpe and Jasiuk, 1992, [99])

$$\upsilon = \frac{K - G}{K + G} \tag{3.5}$$

which, applying equation 3.4, is

$$\upsilon = \frac{1}{3} \tag{3.6}$$

for a central force spring lattice, thus restricting the anisotropy of this type of lattice within narrow limits (cp. e. g. Ostoja-Starzewski et al. (1996, [78]) for a comprehensive discussion of the mechanical properties of a spring network).

The internal reference value for α is set to 1, calibrated and applied to the olivine phase. Spring constants for other phases are linearly related to $\alpha_{olivine}$ by

$$\alpha_{phase} = \alpha_{olivine} \cdot \frac{G_{phase}}{G_{olivine}}. \tag{3.7}$$

Grains, in the terminology used here, refer to continuous two-dimensional areas which are separated from their surroundings through a difference in the mechanical properties, in particular of the spring constants of the respective area (Fig. 3.4). These grains can be part of the reaction, if they represent either α- or β-phase, or can be non-reactive. In either case grains will have an impact on the surrounding stress field. Springs crossing a grain boundary are assigned the average youngs modulus of the involved grains.

Heterogeneities Due to the limited capability of the normal spring network to model anisotropies of materials, the elastic moduli of single grains will be initialized with the isotropic moduli of the respective material as tabled in Appendix C under application

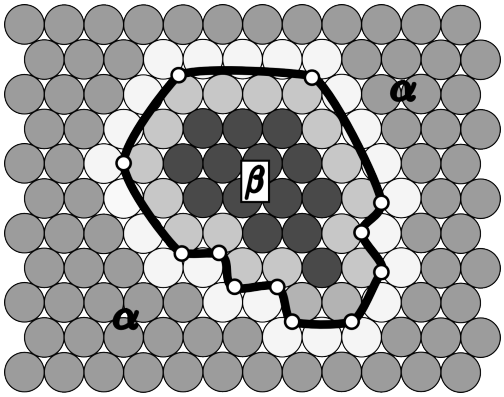

Figure 3.4: Outline of an interphase boundary of a β-phase grain in a homogeneous matrix comprised of α-phase, as it is represented in the model. Dark coloured particles are located within the respective phase, while lighter colours indicate particles situated at the interphase boundary. The bold black line marks the idealized continuous 'real world' grain-boundary.

of Eq. 3.7. Distributions of any kind are applied subsequent to this initialisation.

The typical thermodynamic assumption of a perfectly homogeneous system must be regarded as a simplifying approach towards the description of a system. Heterogeneities and anisotropies build important nucleation sites in real materials, in particular boundaries and edges of grains, and are thus of great importance for the modeling. In the simulations, which have been performed, the following three types of heterogeneities were applied to the discrete material representation.

The inherent disorder of a system can be modeled as an extension to a fully homogeneous system by applying quenched noise, i. e. every mechanical element is attributed a mechanical property, selected randomly from a gaussian distribution which is characteristic for the material (Fig. 3.5, (a)). Besides being a reallistic parameter in some settings, this approach allows to reduce effects of the hexagonal lattice orientations (Malthe-Sørenssen et al., 1998, [70]).

A further type of heterogeneity can be introduced in order to model a system with randomly oriented anisotropic mineral grains in the commonly homogeneous material representation of the central force spring network. For this purpose, a gaussian normal distribution is applied to the properties of the mechanical elements of entire grains, leading to mechanically homogeneous subareas within the system. This approach is of importance for grains of the anisotropic α-phase, in order to supply nucleation sites

for the β-phase in an monomineralic material.

Finally, a third type of heterogeneity is applied by introducing non-reactive grains, representing e. g. garnet in the present context, which have either higher or lower Youngs moduli than the host phase and are important factors for the distortion of the stress field (Fig. 3.5, (b)).

Effects of a phase transition on the parameters of the unit cell and the network
If a particle undergoes a phase transition, the mechanical and thermal properties of a particle need to be adjusted to the properties of the new phase, scaled to the internal settings of the network (Sec. 3.2.2). This implies a reduction of the equilibrium length of the springs of the particle, due to the volume decrease of the high pressure phase, an increase in Youngs/bulk modulus and an increase of the temperature due to the latent heat to be released.

The new internal equilibrium length of the springs (l) of the two dimensional unit cell is calculated from the ratio of the new and the old molar volume from Eq. 2.31 and 2.30, assuming a spherical shape of the unit cell, by

$$f_l = \sqrt[3]{\frac{v_{old}}{v_{new}}},$$

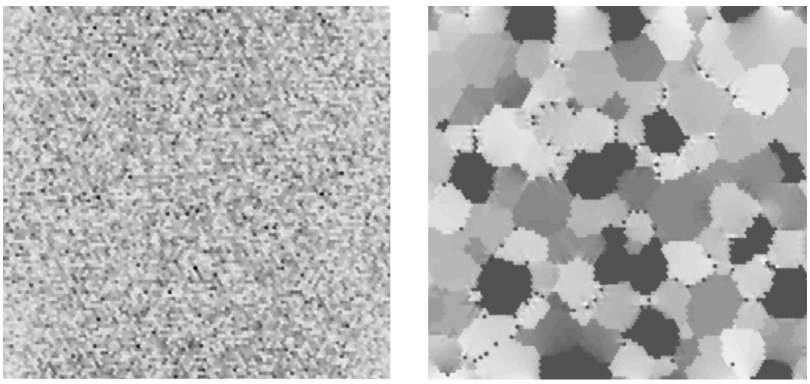

Figure 3.5: Screenshots of mean stress distributions, caused by heterogeneities in the 2D simulations before grain boundary migration starts. (a) Gaussian normal distribution, mimicing an inherent disorder in the system. (b) System containing garnet and pyroxene grains. 'Spots' are spinel nuclei at grain boundaries.

with

$$l_{new} = l_{cur} \cdot f_l.$$

The same principal is applied to the spring parameter α. Since the bulk modulus is linearly related to the Youngs modulus, the ratio of the isotropic bulk modulus of the two substances can be applied by

$$f_\alpha = \frac{G_{old}}{G_{new}}$$

and

$$\alpha_{new} = \alpha_{cur} \cdot f_\alpha.$$

The latent heat release is calculated from Eq. 2.35 and the new heat distribution for the last dynamic timestep is calculated using the finite difference network.

If an initial gaussian distribution was given in the olivine phase, this is overriden by the spinel, which is assumed to form homogeneous grains (Dupas, 1994, [25]) and to erase preexisting impurities or other sources of heterogeneity.

Further consequences affect the surface energy, that will be changed due to the new curvature of the grain boundary. Similiar effects occur for the normal force acting on the particle, partly because of the new mechanical properties, but also because of the new curvature of the volume element.

3.2.2 Time stepping and stress/strain scaling

The code employs two different kinds of time-step, adapted to the different processes. A primary timestep is related to the progressive deformation of the networks, while the phase transition occurrs on a much shorter timescale and employs a secondary timestep. While the primary timesteps are constant and calibrated to match the strain increments to a geological meaningful timescale, the secondary timesteps will be dynamically determined at runtime. Dynamic timesteps are calibrated to the time, which the next particle needs to be transformed and are fractions of the primary timesteps. Cp. Sec. 3.4.2 for a detailed description of the growth mechanism.

Primary timesteps are used for the calculation of the viscoelastic flow on geological timescales, while dynamic timesteps are used to determine the heat distribution caused by the released latent heat, as well as to determine the point in time when the next

externally applied strain increment has to be occur.

The internally derived stress tensor of the spring lattice, which is based on the spring constant α, is linearly related to geological meaningful stresses by a scaling factor, which is determined by the compression of the spring lattice in relation to the strain on pure olivine reaching the critical pressure of the reaction. Since the kinetic equations depend critically on stress, but not on the exact strain due to the large volume and elastic modulus differences between α- and β-phase, the scaling variable will be reset to the exact desired overpressure after the desired strain is approximated by the finite external deformation steps.

3.2.3 Calculation of relevant energies for a phase transition

The normal stress σ_n, acting on the grain boundary, can be calculated directly from the stress tensor given for every node of the spring network after an elastic relaxation by (Ranalli, 1995, [84])

$$\sigma_n = \frac{1}{2}(\sigma_{11} + \sigma_{22}) + \frac{1}{2}(\sigma_{11} - \sigma_{22})\cos(2\Theta) + \sigma_{12}\sin(2\Theta) \tag{3.8}$$

where Θ the angle between the normal to the grain boundary and the x-axis of the common coordinate system. The grain boundary is assumed, in this context, to be defined by the normal to the connecting spring (Fig. 3.6).

In order to reduce discretisation effects of the spring network on grain boundaries,

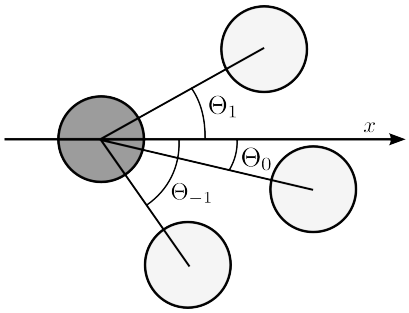

Figure 3.6: Normal stress calculation. The direction of the normal stress is defined by the springs across the grain interface, Θ_n is the angle to the x-axis of the respective spring. The normal stress is adapted to an idealized grain boundary as in Fig. 3.4, using an average scheme described in the text.

caused by the discrepancy between a grain boundary as in Fig. 2.6 and the hexagonal lattice, an averaging scheme is applied which loops over neighbour particles belonging to the other phase, which is simply

$$\sigma_{n,av} = \frac{\frac{\sigma_{n,-1}+\sigma_{n,1}}{2} + \sigma_{n,0}}{2}, \tag{3.9}$$

where the used indices are illustrated in Fig. 3.6.

Another important parameter, the change in surface energy for a specific particle, is calculated from the change in the curvature of the phase boundary, that would be caused by a transition of the particle under consideration. The surface energy is calculated twice, once for the current configuration and once for the geometry that would come into existence after a grain boundary migration. The surface energy γ_s around a single element that crosses the interface can be calculated by

$$\gamma_s = \frac{\gamma_{inter}}{\rho} \tag{3.10}$$

where γ_{inter} is the interfacial free energy and ρ is the radius of the local curvature, determined from the particle springs crossing the phase boundary (Fig. 3.7).

The reduction of discretization effects of the interface boundary on the surface energy is performed by an average over the neighbours, analoguous to the normal stress average above by

$$\gamma_{av} = \frac{\frac{\gamma_{-1}+\gamma_1}{2} + \gamma_0}{2} \tag{3.11}$$

where γ_{av} is the average surface energy and the indices mark neighbour particles of the same side of the phase boundary. The use of indices is clearified in Fig. 3.7.

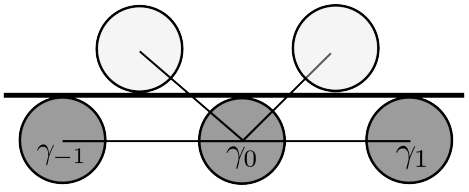

Figure 3.7: Sketch of a phase boundary. The thick black line illustrates the grain boundary. Surface energies are calculated over the springs crossing the interface for every particle and averaged over the neighbour particles, indices as in Eq. 3.11.

The difference in the strain energy before and after the reaction can be calculated by a internal transformation of the boundary particles, giving the two stress tensors of the transformed and the untransformed particle. Due to the large computation times associated with the elastic relaxation, this operation is performed for all boundary particles at once, instead applying a subsequent transformation of every solitary boundary particle.

The strain energies can then be calculated from the strain tensor alternately for the transformed and the untransformed state by (Saada, 1993, [92])

$$U_s = \frac{K(e_{ii})^2}{2} \tag{3.12}$$

and

$$U_d = \mu(e_{ij}e_{ij}) \tag{3.13}$$

where U_s is the spherical strain energy and U_d the energy of distortion. The total strain energy amounts to $U = U_d + U_s$. In the context of Eq. 2.28 and Eq. 2.29, the energy of distortion may be regarded as an approximation for the strain excerted by the volume reduction of the transformed element on its vicinity, while the spherical strain energy represents the stress reduction with regard to the ambient pressure.

3.3 Finite element scheme for thermal conduction

Due to the exothermic character of the olivine→spinel reaction, the local temperature increase of a transformed volume and the reduction of the local temperature in case of a back reaction have to be taken into account. Reaction rates will be accelerated by an increased temperature and may therefore be responsible for considerable localization effects or even a thermally accelerated runaway of the transformation of the total system, as frequently considered by various workers (Sec. 2.2.1 and 2.3.5).

In both cases, the temperature change in a transformed volume element will affect its vicinity, which rises the necessity to include an algorithm capable of calculating the spatial and temporal temperature distribution due to the conduction of the released thermal energy. This is performed using a finite difference lattice with the same spatial extension as the elastic network.

This setting requires a simple API in order to pass information about the current

temperature of a particle back and forth (Fig. B.1). The solution of the set partial differential equations is obtained using an Alternating Direction Implicit (ADI) method, which has the advantage over other solution schemes that the finite difference lattice can be expanded or shortened along the axes of the common coordinate system. It is therefore fully possible to deform the finite difference network in the same manner as the spring network, as far as axe parallel defomation is applied, and to a limited amount in case of simple shear (Fig. 3.8).

Implementation and solution of the finite difference scheme are explained in greater detail in Appendix B.

At the beginning of every simulation run the system is initialized with an uniform temperature, usually 1000 °K. The boundary condition for the finite difference lattice is set by a constant temperature of the same amount as the initial system temperature, which acts therefore as a heat sink during the duration of a simulation, resetting the average system temperature to the starting condition again if thermal energy is produced to slowly. Therefore the the reaction velocity of the system as a whole is not necessarily affect by the locally released thermal energy in a simulation. Instead, released latent heat affects mainly the localisation of the progressing grain boundary migration, rather than overall growth rates.

In order to avoid inadequate localized runaway effects of the grain boundary migration, caused by the local temperature increment, the usually followed discretisation approach - where one particle is transformed at a time - is replaced by a more gradual procedure. During every dynamical timestep, the newly overgrown area of every grain surface particle is calculated, and the released thermal energy of the complete grain

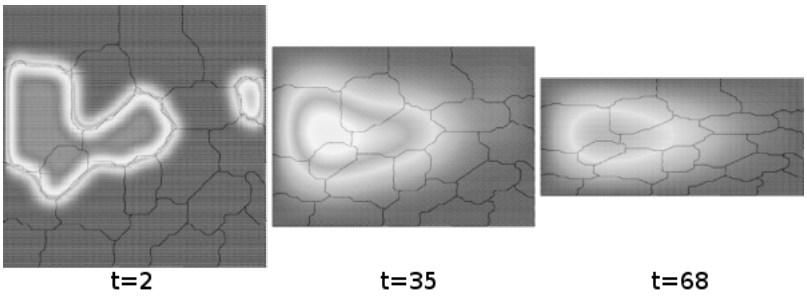

Figure 3.8: Demonstration of heat conduction combined with a vertical compaction of the material.

boundary is considered in the calculation of the heat distribution.

3.4 Phase transition simulation

3.4.1 Spatial starting points of grain growth (nucleation)

Although the computer simulations focus mainly on the process of grain boundary migration, it is, however, necessary to define some sort of starting points from which the growth process can proceed. In general, two distinctly different procedures can be taken into account for this purpose. It is either possible to nucleate grains by some process within the host phase, in order to examine the resulting texture after grain growth, or, alternatively, to start with predefined grains of the product phase in order to observe the evolution of grain surfaces. Both approaches will be briefly discussed below.

Nucleation

In simulations undertaken in previous works (e. g. Mahin et al., 1980, [69], Orgzall et al., 1988, [77]) as well as in the analytical treatment, nuclei are regarded as essentially dimensionless points from where the grain boundary progression starts. Under ideal conditions, without growth at all, it is even possible that a depletion of nucleation sites will never occur as long as growth rates are zero. In a more realistic setting nuclei would be regarded as clusters of several thousand atoms.

However, in a system as it was applied here, using finite volume elements, both assumptions are not appropriate, since the smallest possible amount of material that can be transformed is a single volume element, which is already much larger than a potential nucleus would be. Therefore a nucleus in terms of the model must be thought of as a micro grain or a seed, from where the grain boundary migration does not start, but rather continues.

Two limiting cases for the nucleation process are frequently considered, the homogeneous nucleation model and the site saturation model, both of them reflecting extreme conditions.

In case of an isotropic, one-component solid the Johnson-Mehl model is common (Christian, 1981, [18], Mahin et al., 1980, [69]). In this model, nucleation sites are regarded as inexhaustible and randomly distributed, consequently nucleation occurs

randomly throughout the total volume at a constant net-rate (Johnson and Mehl, 1939, [50]). The transformation is complete, if the total volume is transformed by a combination of nucleation and growth. This nucleation model is best applicable to either homogeneously nucleated transformations or if either nucleation rates are so slow or nucleation sites so plentiful that a depletion of nucleation sites can be ignored during a simulation. Structures resulting from this nucleation model and coupled with constant growth rates were studied by Mahin, 1980, [69].

In the other limiting case, the site saturation model, which was considered by Avrami (1949, [7]), nuclei are regarded as discrete and randomly distributed entities, which are simultanously activated at the beginning of the transformation. The reaction is considered to be finished when the grains, starting from these points, impinge and fill the complete space of the material. This case describes the real situation where there exist preferred nucleation sites due to grain boundaries or impurities in the material.

To complete the mentioned models, Kirkpatrick (1976, [59]) introduced the case of a possible time evolution of the nucleation and growth rate into these models, assuming randomly distributed nucleation sites in a spatially homogeneous magmatic melt.

In this work models introduced above have been modified with regard to the discretized state of the material. A 'nucleus' in the sense of a discrete element simulation can not be described as an infinitesimal small amount of material, as is the case in the idealizing assumptions in the treatments of Johnson and Mehl or Avrami, but has to be represented in form of a completely transformed particle. Therefore we cannot consider the case of essentially inexhaustible nucleation sites, since the number of particles in the system is finite. Further, since a single particle has to be thought of as a thermodynamic system by itself, a proper kinetic treatment would involve a combination of the stochastic kinetic laws for nucleation and growth for every single particle, in order to calculate when the particle is completely transformed. Although this is principally possible, this treatment would desire an accuracy in the progressive deformation of the compressed material which is impossible to achieve, if finite deformation steps are applied. Another factor adding to this problem stems from the still relatively low accruacy in the determination of the parameters relevant for the reaction.

In Sec. 2.3.2 the so-called Avrami length δ_{Av} was introduced, which enables the calculation of the average grain diameter of a system, if constant rates for either grain boundary nucleation I^B or volume nucleation I^V and a constant growth rate Y are

assumed (Eq. 2.16 and Eq. 2.19). For a 2D structure this is

$$\delta_{Av} = \left[\frac{I^B}{Y}\right]^{-1/4} \tag{3.14}$$

where the Avrami length δ_{Av} equals the average grain diameter.

In the course of a particular simulation, I^B and Y are adjusted to the starting conditions of the pressure and the average temperature of the total system, thus the reaction has to be started at some overpressure with reference to equilibrium conditions. An upper estimate for the average grain size is given by the average grain size of the host phase, which has been estimated to approximate 3 mm in diameter (Karato, 1984, [51]) in the transition zone of the mantle. Using δ_{Av} to estimate the number of grains in a system of given size, we can then calibrate the number of nuclei or - more accurately - starting points for the growth process.

Nuclei are inserted at local maxima in the mean stress distribution of the system (Fig. 3.9, a). This procedure is exclusively applicable to systems with heterogeneities, as described in Sec. 3.2.1 above.

A second approach towards nucleation in the simulations is essentially a combination of the Johnson-Mehl and the site-saturation schemes. Particles are transformed randomly in space at the beginning of the transformation (Fig 3.9, b). This approach is applied in case of homogeneous mono-crystalline systems. Also in this case the number of nuclei is adapted to the system size, using grain diameters given by Eq. 2.16.

As another start condition, the growth routine is applied to predefined interfaces of α- and β-phase. This is useful if the development of surfaces on small scales is examined and is also frequently applied.

3.4.2 Grain boundary migration

General description

The growth rate equation, given in Eq. 2.8, relies on the difference between the energetic states of a thermodynamic system before and after it went through a possible phase transition. Obviously this scheme depends on certain inavoidable simplifications, common in thermodynamics.

For once the scheme assumes a monomineralic starting material in combination with predefined values for the scalar variables pressure and temperature, which are assumed

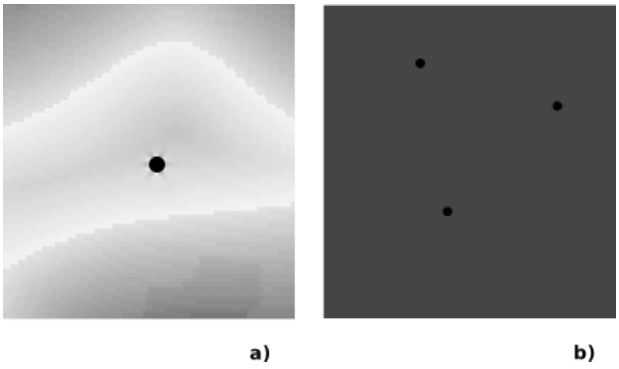

Figure 3.9: Depiction of the two different nucleation models used in the simulation. Black dots represent nuclei. a) Nucleation at a local maximum of the mean stress distribution. b) Random nucleation in a homogeneous stress field. Both models nucleate at the beginning of the transformation.

to be homogeneous throughout the entire system. Local anisotropies and heterogeneiteis of the starting material, introduced by e. g. a polymineralic host material or a non-hydrostatic deformation, can not be taken into account.

Further, the common thermodynamic treatment can not consider the rheological change of the material created by the phase transformation itself, namely the volume reduction and the raised bulk modulus caused by the transition itself. Finally, the equation set insinuates that the system is not affected by and does not interact with ambient materials.

In the simulations these shortcomings of the given thermodynamic equations can be circumvented by regarding every particle as a finite-sized subsystem, which is in constant elastic and thermal interaction with its neighbouring particles. This allows the introduction of local energies into the equation. Thus, in difference to the schemes mentioned in Sec. 1.3.1, the calculation scheme is not bound to a unique growth rate for every grain of β-phase or even the total system, instead a growth rate can be calculated for every node of the network, thereby taking anisotropies of the growth rate into account.

Since rate laws depend on the change of the free energy in a system induced by the reaction, the rate of grain boundary migration can be determined for a given boundary-particle if it is possible to calculate the energies acting on it before and after it was subjected to a possible phase transition.

The main driving force is given by the normal stress acting on a grain boundary in conjunction with the volume change associated with the phase transition. The effective direction-dependent normal stress force, entered in Eq. 2.8 is given by (Shimizu, 1992, [94])

$$\Delta\sigma_n = P_E - \sigma_n. \tag{3.15}$$

This equation applies the common assumption of equilibrium pressure (P_E) for the particle after the phase transition occurred. The volume of a particle before and after a transition, the second part of the driving force, is calculated by Eq. 2.31 for the present local temperature. The volume reduction due to pressure can be ignored, since compression is automatically taken into account in the relaxation algorithm of the elastic lattice.

In case of surface energies and strain energies, the state before and after a transition of a particle are taken into account, thus

$$\Delta\gamma = \gamma_{transformed} - \gamma_{initial} \tag{3.16}$$

and

$$\Delta U_t = U_{t,transformed} - U_{t,initial}. \tag{3.17}$$

The current temperature of a particle is given by the latent heat release in conjunction with conduction of the thermal energy released by nearby transitioned particles.

Direction dependency of growth rates

The direction of growth rates on a migrating phase boundary is defined by the orientation of the grain surface (Fig. 3.10 and Fig. 2.8). In the continuous case the orientation of the surface is defined by a tangent on a infinitesimal section of the grain interface. In a discrete material representation, a grain boundary element is defined by an area of finite extend with a circular or elliptical outline. As a consequence, similar to the argument in the discussion of the nucleation routine, an isolated particle has properties resembling an independent system of finite extend fare more than an geometrical point and requires an adequate treatment (Fig. 3.11). Therefore a particle is overgrown from more than one direction, depending on the given interphase boundary and outlined by the particle network.

In agreement with the hexagonal geometry of the lattice it suffices to consider the

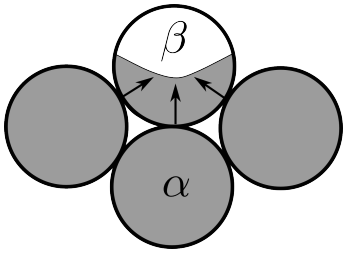

Figure 3.10: Sketch of the direction-dependent overgrowth of a particle of phase α, situated on the grain surface, by phase β. This is a section of the hexagonal particle lattice.

six next neighbours as potential growth directions, where the direction dependent parameter is given by the normal stress (Sec. 2.3.3). Other relevant parameters (e. g. the change of the surface energy) are direction independent and have to be calculated only once for each particle.

For reasons of mathematical solvability, a particle is regarded to be rectangular concerning the addition of rates and the calculation of the transformed area (Fig. 3.12). This requires the conversion of the calculated rate vectors from the hexagonal configuration to the common rectangular coordinate system.

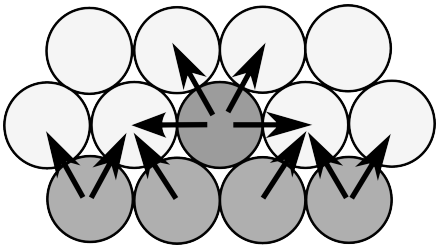

Figure 3.11: Sketch of the growth directions for single particle on a grain boundary. The figure is simplified in so far as only growth of one phase is depicted.

The vectorized growth rates are added up in every timestep and for every particle, which will be transformed in the instant it is completely transformed.

3.5 Classification of the growth algoritm

The growth-algorithm described above shows much resemblance the classical Eden-model for fractal growth (Eden, 1961, [26]), which is frequently applied in the simula-

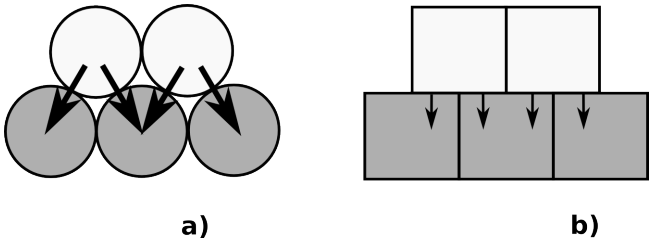

Figure 3.12: (a) Vectorized growth rates, derived from the hexagonal grid. Since the equation for the overgrown area is not solvable for circular shapes, the rates are transformed internally into vectors on a rectangular grid. (b) The shape of particles is assumed to be rectangular for this purpose. Including the correction of the normal force vector on the grainboundary (Sec. 3.2.3), the resulting growth rate vectors derived from (a) for the particle in the middle are depicted.

tion of mineral growth (e. g. Meakin, 1988, [71], Reis, 2003, [85]). The basic procedure of the Eden model is as follows: starting from a seed, one of the empty sites next to the perimeter of the current cluster is selected randomly and added to the cluster. After repeating this procedure many times, a large cluster is achieved with a self-affine, non-trivial fractal surface structure, while the general geometric outline is spherical (Fig. 3.13).

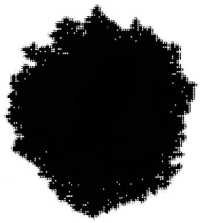

Figure 3.13: Eden cluster containing 5000 particles grown from a single seed by random occupation of interface sites. After Vicsek, 1992, [102].

Consequently, due to the algorithmical similarities, the spinel structures which were obtained in this work can be assigned to the large class of Eden type growth fractals. If the base conditions of the Eden model are seemingly slightly varied, e. g. by combining the stochastic procedure with a quenched noise on one or more lattice parameters, the mathematical treatment of the resulting growth structures becomes surprisingly non-trivial (Bunde and Havlin, 1996, [15], Viscek, 1992, [102]). In general, variations of the

setup of stochastic fractal growth models leads to variations of the roughness of the structure (i. e. the either the fractal surface dimension or the fractal mass dimension) as well as of the rate of asymptotic convergence towards a stable limit of this parameter.

4 Review of the anticrack theory of faulting

4.1 Anticrack theory of faulting

Green and Burnley (1989, [40]), Green and Houston (1995, [41]), Riggs et al. (2001, [88]) and other authors promote what is called the 'anticrack theory of faulting' as the cause of deep seated earthquakes. This idea arose from microstructures which were observed by these authors in a couple of high pressure experiments on the basis of germanate olivine (Mg_2GeO_4) as an analogue material for common olivine (Mg_2SiO_4). They encountered spinel lenses with long-axes which were oriented parallel to the direction of the lowest compressive stress (σ_3). They concluded that these structures form in a similar way as anticracks, a concept introduced by Fletcher and Pollard (1981, [29]) for the description and explanation of pressure solution surfaces (Fig. 4.1).

Anticracks originate at stress concentrations in rocks and propagate parallel to the direction of σ_3. Thus these structures can be described by the same equations commonly used for the description of tensile cracks, if a simple inversion of the signs for the displacements and the stress fields around these structures is performed. Green and Houston (1995, [41]) propose a similar model to explain the preferential propagation of the spinel phase in the σ_3 direction, in the presence of differential stress (Fig. 4.2).

In their model, the driving force for the transition is given by stress concentrations at the tips of spinel inclusions, where the volume decrement related to the phase transition is compensated. These stress concentrations accelerate in turn the transition parallel to the direction of the least principal normal stress, σ_3. This is accompanied by a stress reduction on the σ_1 facing site of the spinel inclusion, which decelerates the transition in the respective direction. Following the approach of Green and Houston (1995, [41]), the observed preferred growth orientation normal to the direction of main compression would result.

The identification of anticracks and the distinction between anticracks and other growth features that Green and Houston (1989, [40]) and Riggs and Green (2001, [88]) found in their high pressure experiments was not performed on the basis of an in situ observation of the local stress field around the spinel inclusions. Instead, the authors evaluated secondary characteristics of anticrack structures, e. g. the roughness of the grainboundary of β-phase grains and the observed general growth orientation normal to the orientation of the externally applied main compression.

The classical theory of anticrack formation, as described in a thought experiment by Fletcher and Pollard (1980, [29]) is depicted in Fig. 4.1. An initial cavity is cut into a solid under differential stress. Large compressive stresses develop at the tips of the cavity, because the solid around the cavity is now completely sustained by the remaining material. Since these normal stress concentrations face the σ_3-direction, a compaction-dependent pressure solution processes normal to the direction of main compression is initiated (cp. Fig. 4.1).

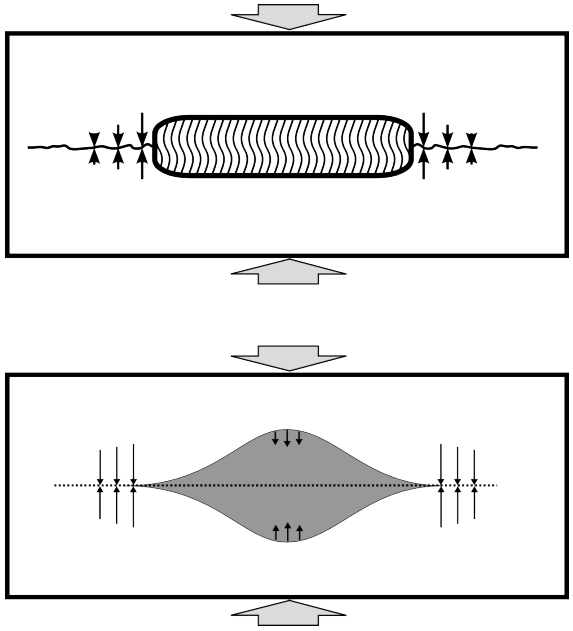

Figure 4.1: Induced compressive stress around a cavity under differential stress, the basis of the original anticrack model put forward by Fletcher and Pollard (1980, [29]). The depicted pressure solution surface normal to the stress concentrations is an example for the formation of anticracks.

The authors, who promote the anticrack theory of faulting as the cause of deep seated earthquakes, believe the effects of the local volume decrease on the stress field, which is caused by the transition of olivine to the denser spinel structure, as similar to the effects of the cavity in the thought experiment of Fletcher and Pollard (1981, [29]).

Nevertheless, unlike a cavity, a solid inclusion does still interact with the surrounding material and is able to induce or compensate stress. The stress induced by the phase transition is strongly dependent on the ambient pressure, as will be outlined in the next section.

Green and Burnley (1989, [40]) and Green and Houston (1995, [41]) are not explicit about the particular transformation mechanism that is expected to be responsible for the propagation of a spinel grain, once it is nucleated. However, three different mechanism for the olivine→spinel transition are discussed in literature (e. g. Shimizu, 1992, [94], Riedl and Karato, 1996, [86], Rubie and Ross, 1994, [91]). In order to achieve anisotropic grain growth by means of a kinetic acceleration of the grain boundary migration into a preferred direction one of the following situations must be given, depending on the transformation mechanism.

- Either the normal stress acting on the grain boundary displays a relative maximum on a particular segment of the grain boundary, compared to other sections. In this case, an acceleration of the grain boundary migration in the sense of the Gibbs scheme can be expected (cp. Sec. 2.3).

- Another possibility to be considered is an increase of the mean stress in the surrounding host material, so that a relative increase of the reaction rates would be initiated. In this case the growth of the spinel lense would not be caused by a lateral grain boundary migration in the classical sense, but would include the full mechanism of nucleation and growth, but locally accelerated.

- A third mechanism that might be responsible for anisotropic growth of the spinel phase is a local increase of the differential stress, which has been considered to be a possible driving force for the transition on the basis of a martensitic mechanism (cp. e. g. Mosenfelder et al. (2001, [73]) for a short review).

However, the general role of the martensitic mechanism for the olivine→spinel transition is highly controversial and occurs probably only under unrealistically extreme

conditions. Although Burnley and Green (1989, [40]) consider a martensitic mechanism for the explanation of spinel nucleation, they were able to exclude a martensitic transformation explicitly as the mechanism behind the grain boundary migration of spinel grains in their experiments.

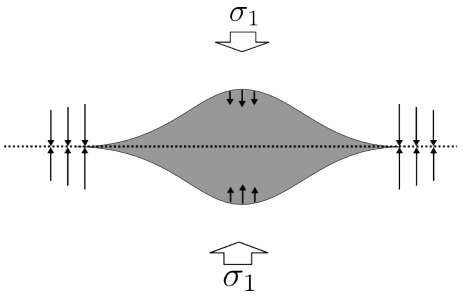

Figure 4.2: (a) Anticrack mechanism caused by an spinel inclusion as proposed by Green et al. (1995, [41]), where the structure propagates normal to the σ_1-direction. The reason for the propagation is a supposed stress increase at the tips of the spinel lense and a decrease on the σ_1 facing side, caused by the depicted displacements within the host material.

Since stress is the driving force of the olivine→spinel transition and the grain boundary migration, the next section is dedicated to the derivation of the characteristics of the stress field in the vicinity of a spinel inclusion. Further the displacements within the parent phase caused by a olivine→spinel transition will be investigated.

4.2 Local stress and displacements initiated by the $\alpha \rightarrow \beta$-olivine transition

In this section we are going to consider the magnitude and the type of stress associated with a $\alpha \rightarrow \beta$ olivine transition of an arbitrary portion within an olivine host under externally applied strain. Since differential stress is a necessary precondition for the formation of the σ_3-parallel structures described above, we will consider the somewhat extreme differential stress caused by vertical uniaxial compression in the following. The relevant parameters for the propagation of a preexisting high pressure phase are given by the location of local stress-maxima around the spinel grain, which are caused by the interplay of the transition with the external stress field. Hence we are going to derive the stress at the grain boundary of the spinel inclusion, which is represented

by a number of characteristic points, using numerical simulations on the basis of the elastic spring network together with analytical considerations.

For this purpose we consider a 2-dimensional section through the host material under vertical uniaxial strain, as depicted in Fig. 4.3. Because the strain which is exerted on the grain boundary by the phase transition is linearly related to the change in stress, it suffices to derive the stress state before and after a sudden transformation of a circular portion of the host material at the points A_1, A_2 and B_1, B_2, given in the same figure. These points are located at opposing sides of the spinel/olivine boundary and are thought to be the endpoints of two traverses, termed profile A and B from here on.

Since these profiles are parallel to the minimal and maximal external compression, the points A_1, A_2 and B_1, B_2 are located at the local maxima or minima of stress induced by a phase transition. The stress conditions at A_1, A_2 and B_1, B_2 are obviously identical and are thought to be dominated by the one-dimensional contraction along the respective profile, which is caused by a phase transition. As a precondition we assume an identical stress field for every volume element within the olivine-host prior to the transition.

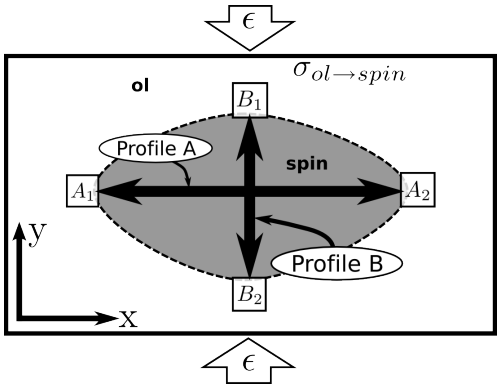

Figure 4.3: Section through the portion of olivine that will be transformed to spinel. The points A_1, A_2, B_1 and B_2, connected by the profiles A and B, are located at the maxima and minima of the stress field and are referred to in the text.

According to the anticrack theory of faulting displacements within the host material during the transition are responsible for a pressure increase at A_1 and A_2. This process corresponds to a displacement field as depicted in Fig. 4.2, where particles within the host material are supposed to be displaced vertically towards the horizontal median-line

of the spinel inclusion. However, a displacement path like that is strongly simplified, since it ignores the stress and hence the strain, which is exerted on the grain boundary due to the phase change.

The transition-related stress and the strain are defined by two parameters:

1. by the spherical volume decrement, caused by the density increase, and
2. by the hardened elastic parameters within the transformed volume.

The normal stress, exerted on the grain boundary at the marked points in Fig. 4.3 by a transition of the material inbetween can be calculated by

$$\Delta\sigma_n = E_{spin} \cdot (\epsilon_{ex} - (1 - f)) - E_{ol} \cdot \epsilon_{ex}, \tag{4.1}$$

where ϵ_x denotes the externally applied strain parallel to the profile in consideration with $\epsilon_y = max$, $\epsilon_x = 1/3 \cdot \epsilon_y$ in case of uniaxial compression. This equation accounts for the strain, introduced by the volume change of the transformed volume element, as well as for the changing youngs modulus. f is derived from the molar volume of the low pressure phase (v_{LP}) and of the high pressure phase (v_{HP}) by

$$f = \frac{\sqrt[3]{v_{HP}}}{\sqrt[3]{v_{LP}}}.$$

The Youngs modulus E is derived from the isotropic bulk modulus K by (Fowler, 2001, [30])

$$E = 3K\,(1 - 2v)\,,$$

with $v = 0.\bar{3}$ the Poisson ratio.

Fig. 4.4 depicts the normal stress, would will be exerted on the grain boundary, if the transition would occur at an arbitrary external compression parallel to any profile over the grain. Due to the interplay between the Youngs modulus and the volume change, the exerted normal stress is negative for small external deformations and turns positive for large deformations.

If the phase transition occurs at a small external deformation, it will therefore result in a displacement pattern as in Fig. 4.5 (a). For large external deformations the resulting displacement pattern is as in Fig. 4.5 (b), since under vertically uniaxial compression the horizontal compression amounts to only 1/3 of the vertical external

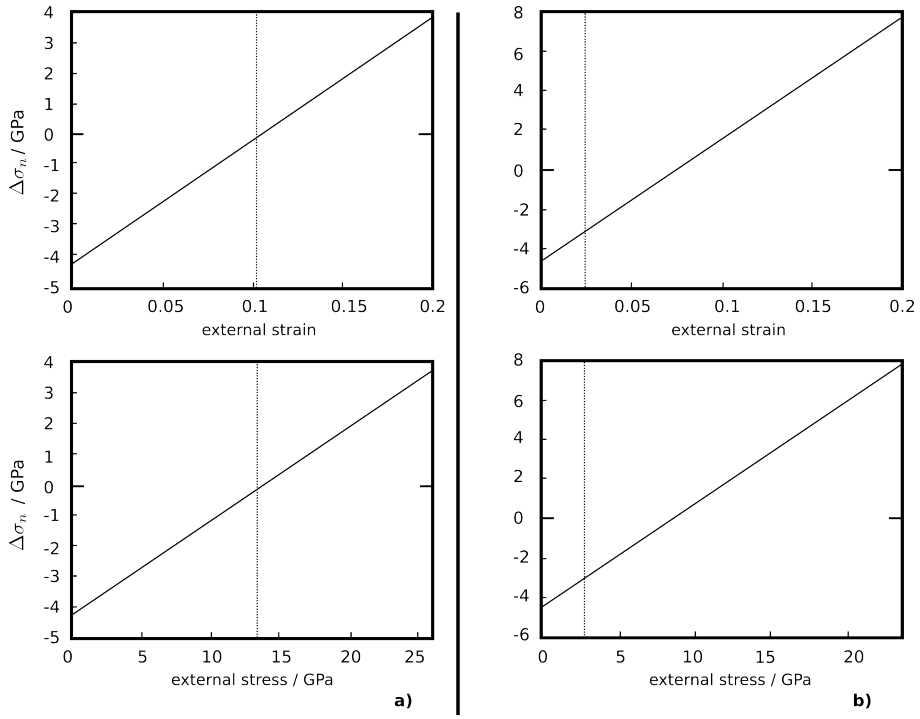

Figure 4.4: The lower plot in each figure plots the normal stress, which is exerted on the olivine/spinel grain boundary by a hypothetical phase transition, against the externally applied normal stress in the same direction. The upper plots in both figures depict the same in dependence of the externally applied compressional strain. (a) for the silicate-olivine/spinel (Mg_2SiO_4) system. (b) for the germanate-olivine/spinel (Mg_2GeO_4) system. The vertical dotted line in (a) marks the critical pressure of a α/β-Mg_2SiO_4 at 1000 K. The common reference value for the critical pressure in Mg_2GeO_4 is marked with a vertical dotted line in (b).

strain and causes thus a negative strain on the boundary. The transition related stress on the grain boundary is therefore positive in the direction parallel to the main compression and negative in the direction normal to it.

To compare the displacement patterns with those of the original anticrack scheme from Fletcher and Pollard (1981,[29]), Fig. 4.5 (c) depicts the displacement field within a solid caused by insertion of a cavity. The principal directions of the displacements are independent of the amount of externally applied uniaxial compression. The different displacement fields caused by a phase transition and by a cavity are obvious and make it clear that the term 'anticrack' is not appropriate for a phase transition in olivine.

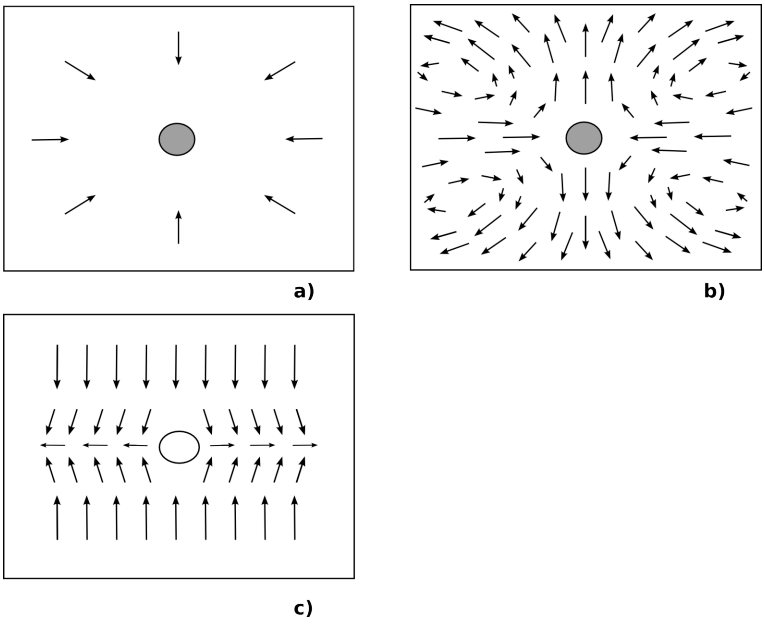

Figure 4.5: Displacement patterns caused by the transition of a circular portion within the material to a denser high pressure phase, compared to displacements induced by the introduction of a circular void, calculated with the spring network. The length of arrows is independent of the amount of the displacement. (a) and (b) depict the displacements associated with a phase transition with an externally applied uniaxial vertical strain of 0.01 and 0.175, respectivly. The inversion of the flow field is evident. (c) Flow field due to the introduction of a void, where the flow pattern is independent of the amount of uniaxial strain.

If we consider the effect of the phase transition on the stress field in the vicinity of the spinel inclusion at points A_1, A_2, B_1 and B_2, we come to the following conclusions for several types of externally applied stress.

- The change of the normal stress acting on the grain boundary ($\Delta\sigma_n$) and thus of the strain depends linearly on the relation between the external compression parallel to each profile and the contraction of the material between the endpoints of these profiles. For low external strain $\Delta\sigma_n$ is negative, while it turns positive if the externally applied compressive strain is larger than a certain threshold. Since the external strain is larger in y-direction, which is the direction of the uniaxial compression, than in x-direction, the normal stress acting on the grain boundary reaches a maximum at points B_1 and B_2 and local minima at A_1, A_2.

- The mean stress, which is usually taken as a replacement value for pressure in thermodynamics, shows the same maxima at B_1, B_2 and minima at A_1, A_2 as the normal stress. This conclusion can be directly drawn for these points by the definition of mean stress ($(\sigma_x + \sigma_y)/2$), where the transition-induced reduction of σ_x is under the assumed state of external deformation always larger than the reduction in σ_y. 2D-related effects on the stress field are ignored. Thus the absence of horizontal transition-related strain at B_1, B_2 and of vertical transition-related strain at A_1, A_2 is assumed. Fig. 4.6 (a) and (b) display the mean stress field, based on a simulation using the spring network.

- The differential stress, defined as $|\sigma_1 - \sigma_2|$, displays an inverted gradient field compared to mean and normal stress, with maxima at A_1 and A_2 and minima towards the direction of compression at B_1, B_2. The reason is essentially the same as above, since σ_1 and σ_2 correspond to σ_x and σ_y under the given uniaxial deformation. Inserted into the equation of differential stress, we obtain the mentioned maxima. The differential stress field from a simulation with the elastic spring network is displayed in Fig. 4.6 (d).

Comparing Fig. 4.6 (a) and (b) with Fig. 4.6 (c) we find that the stress field related to a cavity is inverted with regard to the stress field caused by a phase transition.

4.3 Consequences for the anticrack hypothesis and the grain topology of spinel

The assumption of an anticrack mechanism of Riggs and Green (2001, [88]), Green and Burnley (1989, [40]) and others, outlined in Sec. 4.1 and Fig. 4.2, is critically related to a vertical displacement of the particles in the host phase towards the horizontal axis of the spinel inclusion. This displacement is considered to be a response to the volume loss caused by the phase transition.

It is evident from Fig. 4.5 and the considerations above that this mechanism is far to simplifying, since it does not take the radial volume loss and the hardening of the material into account. Taking these variables into consideration it becomes clear that the particle movement caused by the phase transition, does not resemble the displacement pattern caused by a cavity as in the thought experiment of Fletcher and

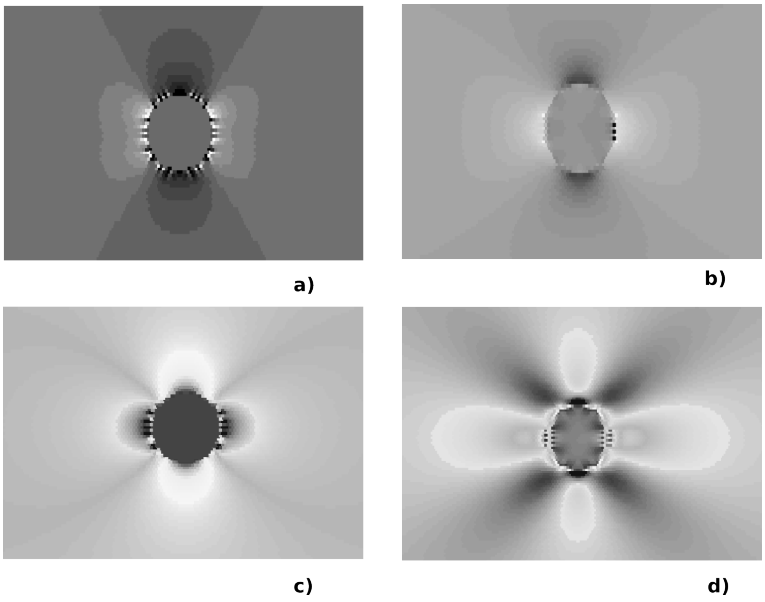

Figure 4.6: Stress patterns developed after the insertion of a circular spinel inclusion or a cavity into an olivine host, calculated with the elastic spring network. The deformation is vertically uniaxial. Dark colours indicate high stresses. (a) Mean stress field caused by an spinel inclusion, developed at a very low deformation of the system. (b) Mean stress caused by an spinel inclusion developed at a strain of 0.15. (c) Mean stress pattern due to insertion of a circular hole. (d) Differential stress induced by the presence of a spinel body.

Pollard (1981, [29]).

If the transition occurs at pressures below a certain threshold the vertical component of the displacements caused by the transition agree with the displacements caused by introduction of a void, but are horizontally reversed. If the critical pressure in Mg_2SiO_4 is larger than this threshold, the displacement field is completely inversed compared to the displacement field caused by a hypothetical void.

It is of interest to point out the differences between the olivine analogue Mg_2GeO_4, which has been used in the experiments by Riggs et al. (2001, [88]) and Green and Burnley (1989, [40]), and Mg_2SiO_4. While the elastic properties and the volume difference between α- and β-phase in both materials are almost identical (Appendix C.2), the phase transition in germanate olivine occurs at roughly 2.7 GPa, compared to c. $13 - 14$ GPa in silicatic olivine. With reference to Fig. 4.4 this means that the transition in $MgGeO_4$ occurs clearly in the field of $\Delta\sigma_n \ll 0$, causing a displacement

pattern as in Fig. 4.5 (a), while the critical pressure of $MgSiO_4$ is close to the point, where the phase transition doesn't induce any strain at all. The displacement effects caused by a Mg_2SiO_4 transition are thus considerably smaller than those caused by its germanate analogue.

Assuming a phase transition at 1000 C, which is related to a critical pressure of 13.2 GPa, combined with uniaxial compression as above, the critical pressure of the transition will be reached if $\sigma_x = 20.5\ GPa$, which is clearly above the threshold at which the phase transition will exert a positive normal stress on the grain boundary. The value of σ_y is only 4.4 GPa under these circumstances and exerts thus a negative strain on the grain boundary. Hence, if the host material is composed of Mg_2SiO_4, the realistic displacement field is given by Fig. 4.5 (b), and thus reverse to the displacement field of an anticrack. Thus, an anticrack-like mechanism can be excluded. In germanate olivine, which transforms at c. $\sigma_x = 4.05\ GPa$, i. e. far below the development of positive strains due to the phase transition, the displacement field of Fig. 4.5 (a) must be assumed.

In addition, the normal stress on the grain boundary and the mean stress field, that form maxima on the grain boundarie at points B_1 and B_2 from Fig. 4.3, can be ruled out as the driving forces behind lateral growth of spinel parallel to the σ_3-direction. The maxima in the differential stress field could be an alternative explanation for anticrack-like structures, if the according transformation mechanism hadn't been ruled out by Green and Burnley (1989, [40]) as well as Riggs et al. (2001, [88]).

4.4 Possible alternative explanations for the occurence of anticrack-like microstructures

It appears likely from the considerations above that the spinel-structures, that the Burnley and Green (1989, [16]), Riggs and Green (2001, [88]) and others believed to be anticracks, formed by localization processes on impurities in the olivine host, an effect which was encountered in the numerical simulations presented in the following chapters as well (cp. Chap. 6). Alternatively, they could be a simple misinterpretation of the local stress field, which can not be easily monitored in high pressure experiments.

The growth mechanism, encountered in the computer simulations described in detail in the following chapters, is a normal stress driven grain boundary migration into a

host with a certain inherent disorder. This will lead to a dominant grain growth parall to the σ_1 direction, but permits the development of secondary anomalous structures.

5 Control parameters of high pressure driven grain morphologies

5.1 Overview

The aim of this chapter is the derivation of the basic influences on the dynamics and the grain shape development of the pressure driven polymorphic olivine→spinel transition. We are going to demonstrate that a simple relation between grain growth and the scalar thermodynamic variables, which are commonly applied in simulations of the olivine→spinel transition, does not exist.

The dynamics of a reaction as well as the resulting structures of the product phase are influenced by the direction of the general stress field and dynamic factors created by co-developing high-pressure grains. This is of particular interest if predictions about the material properties caused by the transition are being made. The formation of stable throughgoing networks of the product phase within the host are a decisive turning point for the rheological properties of the over-all material.

The principal strength of a computer simulation over laboratory experiments is two-folded:

- firstly the computer enables the experimentator to observe the dynamics of the process during its occurence, instead of relying on the static outcome of an experiment and the need of a correct interpretation.
- Further, the experimentator is capable to eliminate any unwanted or even unknown parameters contributing to a physical process completely from the computer experiment. Therefore it is possible to focus exactly on the parameters of interest.

This chapter is therefore about the general control parameters of a grain boundary migration under high pressure. Assuming the wide range of possible adjustments which

can be made to the experimental setup, which include e. g. the self organization of the growth process by the initial süatial distribution and number of nuclei, the exact value of the activation energy and other parameters, this chapter will concentrate on particulary important or typical patterns which were frequently encounterd in simulations.

The parameters which may potentially determine the structure of olivine/spinel boundaries can be assigned to one of three following categories.

- The first category consists of environmental, thermodynamically intensive, parameters. In the computer simulations this is the externally induced stress field. The other intensive parameter, temperature, is initialized with a homogeneous 1000 C.
- The second category consists of the material parameters of the host phase and the product phase, which determine the local conditions for grain growth. In the simulations this refers to e. g. heterogeneities of the elastic constants of the mechanical elements of the spring network and the value of the viscosity constant η.
- A third group of factors consists of energies which are created by the phase transition itself. This includes the surface energy, which depends on the local curvature of the α/β interface, and the thermal gradient field which is created by the latent heat release of the reaction. This dependence of the reaction on self-generated parameters introduces an element of self-organization into the development of the grain morphology.

The microstructural evolution of spinel grains was simulated and analysed under the assumption of strongly idealized conditions, where the idealization consists of a predefined spatial distribution of spinel nuclei and a clearly defined homogeneous stress field. This setup is combined with a monomineralic, completely homogeneous olivine parent.

Local growth rates were calculated based on the normal stress on the grain boundary. These normal stress based calculations were then supplemented in alternation by the thermal energy released by the transition and the surface energy of the olivine/spinel interface. In addition to a solely elastic spring network, the structural development of spinel grains was simulated under visco-elastic conditions. The main contributor to the

driving force for grain boundary migration, the normal stress on the grainboundary, was included in every simulation run.

The simulations were performed on a rectangular 200×200 or, alternatively, 100×100 hexagonal grid and were scaled to a side length of 10 μm. This system size is in the range of the microstructures observed by Vaughan et al. (1984, [101]), Young et al. (1993, [106]), Dupas et al. ([25]), Riggs et al. (2001, [88]) and Green and Burnley (1989, [40]), which were presented in Chap. 2. In addition, this specific system size ensures that both, thermal and surface energy, are effective within the resolution of the model.

The temperature of the system is set to an initial value of 1000 K, which leads to a critical pressure of the transition of 13.2 GPa (cp. Eq. 2.1).

5.2 Basic grain shapes

In absence of additional influences on the grain growth of spinel, the effect of the externally applied stress in a monomineralic homogeneous olivine parent is straightforward (Fig. 5.1 (a) - (c)).

Application of homogeneous biaxial strain leads to an isometric shape of the spinel grain, due to the hydrostatic stress and hence identical driving forces in every direction. The hexagonal grain shape is predefined by the hexagonal geometry of the spring network (Fig. 5.1 (a)). In agreement with the discussion in Chap. 4, the presence of a spinel grain leads to a radial symmetric mean stress gradient in the parent material, where the minimum of the stress field is situated at the grain interface. This is due to the density increase of the transformed material, which outweighs the increased Youngs modulus and creates tension on the grain boundary.

Grain growth initiated by a uniaxial compression of the host solid creates a pronounced elongate grain morphology of the spinel grain (Fig. 5.1 (b)), parallel to the direction of σ_1. This elongation is similar to observations in high pressure experiments by Young et al. (1993, [106]) and Vaughan and Green (1984, [101]), which were depicted in Fig. 2.1 and 2.2. The mean stress field created by the presence of the denser spinel phase displays a pronounced orientation, where positive maxima are directed towards the main compression (σ_1), while an elongate stress minimum is situated at the long sides of the grain, facing σ_3.

Again, the characteristics of the stress field and the spinel shape are in agreement

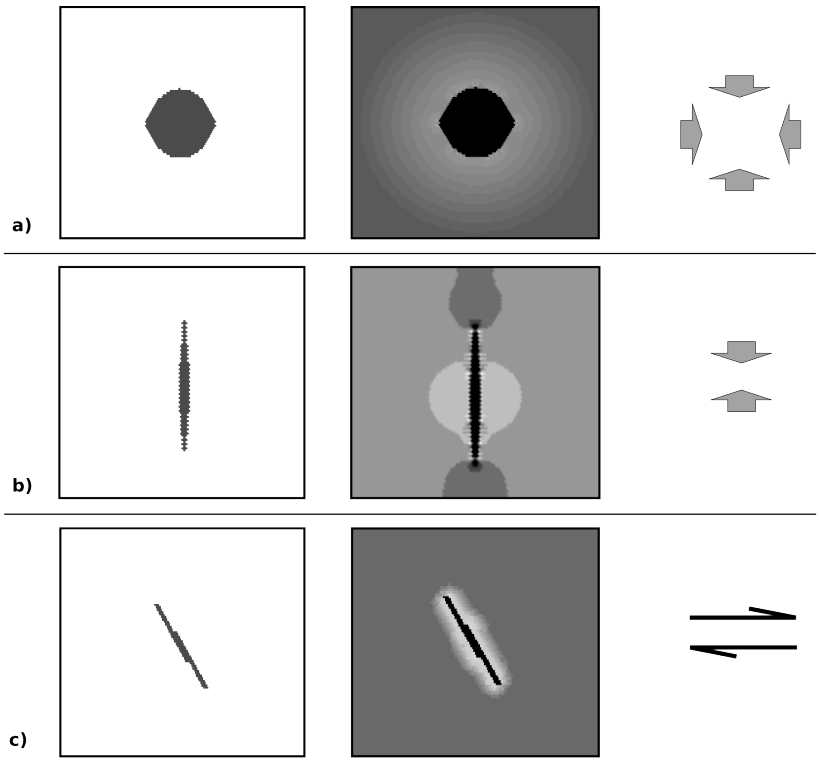

Figure 5.1: Grain shapes created by different types of externally applied stress. The outline of the developing spinel grain is displayed on the left, the mean stress distribution on the right of each subfigure. (a) Hydrostatic stress induces isometric spinel grains and a radial stress gradient. (b) Strongly elongate grain in the presence of uniaxial compression (right), with pronounced stress concentrations at the tips towards σ_1. (c) Elongate grain growth under simple shear conditions.

with the discussion in Chap. 4. The large vertical strain on the system causes the harder and denser spinel phase to produce compressive stress on the grain boundary facing the direction of the largest compression. In addition it causes tension on the sides of the spinel grain facing the low horizontal compression. This stress field is both, created by the presence of the spinel grain and a stabilizing factor for the principal shape of the spinel structure, since the stress maxima at the tipse accelerate the rate of grain boundary migration.

A final stress regime is considered in Fig. 5.1 (c), where the system was subjected to simple shear. The simple shear component was combined with biaxial compression,

which is necessary to create the critical pressure for the transition but does not affect the lattice geometry.

The resulting grain shape displays an elongation similar to the grain morphology which developed under uniaxial strain in Fig. 5.1 (b). The orientation of the grain elongation is parallel to the direction of shortening associated with simple shear. This leads to a maximum of the principal normal stress along the diagonal between the top left and the bottom right in the computer experiment and thus to the grain orientation displayed in Fig. 5.1 (c). The stress gradient field created by the phase transition is far less pronounced than under the conditions of uniaxial compressions, due the the large biaxial compressive component of the deformation, but displays in principal the same features with a maximum of the normal stress at the tips and a minimum along the long sides, but bending the long axis of the stress concentration towards the shear direction.

Under the idealizing conditions of the above experiments, any driving forces other than stress proved to be irrelevant for the development of the grain morphology. Considering the latent heat release of the transition and the surface energy at the interface in the calculations led to grain shapes similar to those that formed in the absence of these energies. This is in particular true for the effect of the surface energy. However, under uniaxial compression the latent heat release leads to a very minor thickening of the resulting grain shape compared to the one depicted in Fig. 5.1 (b).

We may conclude that the crucial factor for the structural evolution of spinel grains under simple conditions is the externally applied stress field only.

5.3 Influence of the presence of viscous flow on the shape of spinel grains

A better representation of the material under mantle conditions, where the olivine→spinel transition naturally occurs, can be reached if the experiments described above are performed on a visco-elastic spring lattice instead of a solely elastic spring network.

It has to be mentioned in this context that the concept of Newtonian viscosity and its particular application in the numerical simulations abstracts and simplifies real conditions in two ways. On one hand the flow behaviour of mantle material is commonly described by power laws, in difference to the linear Newtonian stress-strain

relationship in the model. Secondly, the simulations assume the viscosity η to be a constant scaled to the viscosity in approximately 400 km depth, and abstain from a dynamic adaption of η to the temperature and stress conditions during a specific deformation history. As a consequence the host material displays a non-quantifiable though definitively exaggerated flow during the progressive deformation if compared to a real situation and must be regarded as an extreme case.

The viscosity η is set to a value of 10^{22} $Pa \cdot s$ in the simulations, while the timestep associated with a finite strain of 0.002 is set to 10^{11} s, which approximates conditions within a fast subducting slab.

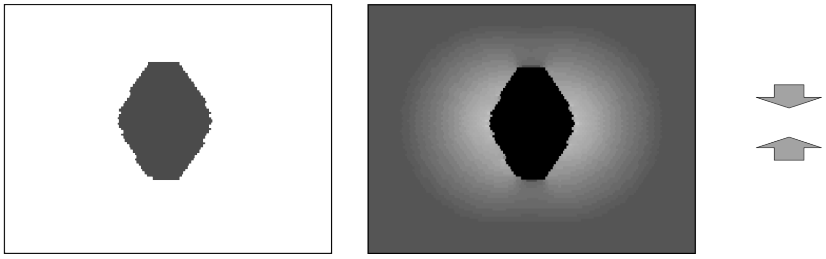

Figure 5.2: Shape of a spinel grain, which developed under uniaxial stress in a viscoelastic system. The image on the right displays the mean stress distribution in the system.

Under purely biaxial compression the stress field as well as the resulting grain morphology are identical to Fig. 5.1 (a). If vertical uniaxial strain is applied, the grain morphology is far less elongated than it would be under solely elastic conditions (Fig. 5.1 (b)), since the orientation of the principal normal stress within the parent phase is largely compensated by internal flow during the progressive deformation. Nevertheless, even though the viscosity is set to a relatively low value, the effects are still clearly present. The spinel grain in Fig. 5.2 does still display a clear elongation into the direction of the main compression.

5.4 Coupling effects during grain growth

It is reasonable to assume that the growth of spinel grains is affected by several energetic coupling effects, which are related to gradient fields created by mineral transitions at nearby localities.

Since the formation of a β-olivine grain depends on the type and the orientation of the stress field present in the parent phase, it can be expected that the characteristic stress fields discussed above, which are a direct consequence of the grain shape of the high pressure phase and the externally applied deformations, will affect the growth of coexisting spinel grains in their reach. Apart from stress the localisation of grain boundary structures is controlled by additional gradient fields, in particular the thermal gradient created by the latent heat release of a phase transition at other localities. Further, the surface energy can accelerate or slow down the velocity of the reaction at energetically favourable localities and thus alter the geometry of the grain shape, which in turn alters the related gradient fields. The simple basic grain morphologies shown above, which are completely controlled by the interplay of the external stress field and the stress created by the growth of a single grain, will gain complexity if they are in the range of the stress or temperature gradient created by another high pressure grain.

In the following two simple examples for the effects of mutual interplay between a few growing nuclei will be presented. Both examples were calculated for uniaxial compression of the system in order to create a pronounced and easily recognizable orientation of the stress dependent component of the grain shape.

The outcome of the simulations is widely dependent on the particular stress field which is typically associated with a spinel grain under differential stress, showing stress concentrations at the tips towards the direction of main compression and a stress minimum at sides facing the principal σ_3 orientation (cp. Fig. 5.1 (b) and discussion in Chap. 4).

Since these stress fields are not symmetric, the decisive condition for the type of the coupling will be the initial spatial distribution of spinel nuclei which decides whether the grain boundary migration will be affected by a local minimum or a local maximum in the stress field. Because the amount of stress in a gradient field is linearly dependent on the square of the distance from its origin (Ostoja-Starzewski, [78]), the proximity of the nuclei will play an important role in the structural development.

5.4.1 Grain shapes influenced by local stress minima created by coexisting spinel grains combined with thermal and surface energies

Both, the temperature gradient field as well as the surface energy acting on a phase boundary, tend to smoothen the roughness of surfaces and create circular or isometric grain morphologies. In case of the surface energy this effect can be explained by the general principle of energy minimization, which is achieved if the local curvature is reduced. This will slow down the growth at the tips of a grain, while irregularities of the surface structure will be evened out.

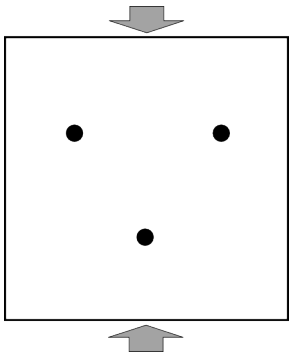

Figure 5.3: Initial settings of the simulations described in this paragraph. Black dots inidcate the location of spinel nuclei in a homogeneous olivine parent under vertically uniaxial compression.

The smoothing-effect of the heat energy on the grain shape is caused by the relatively symmetric shape of the gradient field which is created by the conduction of local latent heat release of the phase transition. Since the effect of the temperature on the growth rate is exponential (Eq. 2.28), the growth of spinel will be considerably accelerated by higher temperatures.

The examples in this section used three spinel nuclei, placed in a fixed triangular configuration within the isotropic, homogeneous olivine parent. The system was vertical-uniaxially compressed (Fig. 5.3). The calculation of the resulting structures incorporates alternatingly plain normal stress (Fig. 5.4 (a)), normal stress plus surface energy (Fig. 5.4 (b)) and normal stress combined with surface energy and thermal energy.

The calculations in the section were calculated on a 100×100 grid and scaled to a

side-length of 10 μm. However, the same structures were obtained in a system with a side-length of 100 μm. Larger systems resulted in structures similar to those in Fig. 5.4 (a). Calculations for smaller system sizes than 10 μm were omitted, due to the considerable difference in size compared to the experimental structures presented in Chap. 2.

Fig. 5.4 (a) depicts elongated spinel grains which evolved after 3200 timesteps. The only considered driving force of the reaction is the normal stress on the grain boundary. The stress concentrations at the tips of the grains are clearly visible. The broad stress minimum along the elongation axes of the grains has, if any, only a slight thinning effect on the spinel grains to the left and the right.

This changes drastically if surface energy is included into the calculation of the local reaction rates, which results in a deflection of the tips of the outer grains towards the larger mean stress and thus away from the coexisting spinel grains which cause the stress gradient (Fig. 5.4 (b)). This effect of the surface energy is closely related to the presence of a gradient stress field. Growth at the tips is slowed down by the effect of the surface energy, while growth at the elongated sides is accelerated towards larger stresses.

If the calculation of the growth rates consider latent heat release in addition, a pronounced concentration of thermal energy develops in between the three elongated spinel grains (Fig. 5.4). The thermal gradient accelerates the reaction towards the central grain. In combination with the deviation of the grain shape caused by the surface energy, the two effects compensate each other which leads to straightend structures.

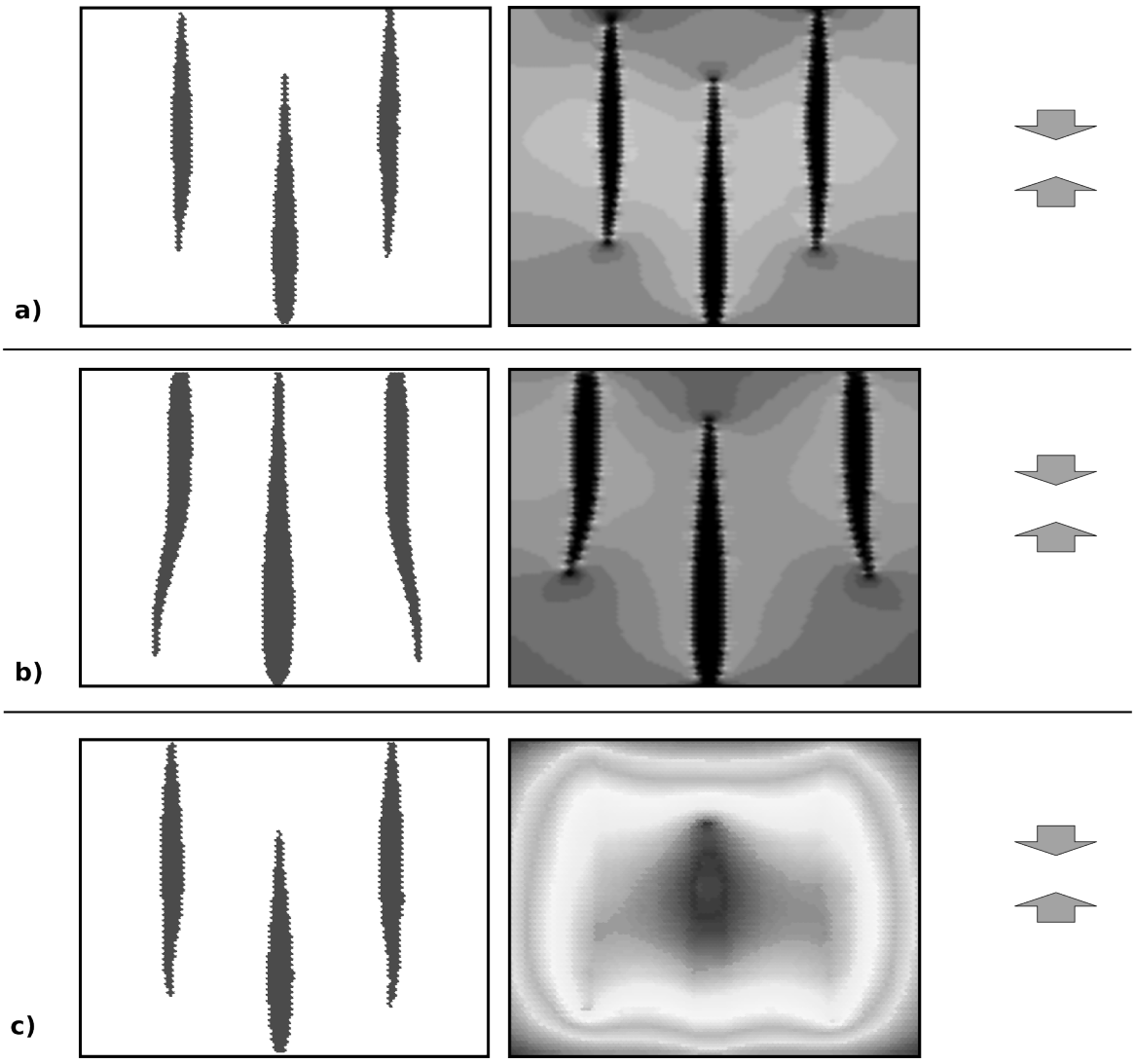

Figure 5.4: Spinel grain shapes evolving under vertical uniaxial deformation. Subfigures (a) and (b) were taken at timestep 3245, (c) at timestep 2000. (a) The only considered driving force is normal stress on the grain boundary. (b) Driving forces are the normal stress and the surface energy. (c) Normal stress combined with latent heat release and surface energy.

5.4.2 Grain shapes influenced by local stress maxima created by coexisting spinel grains

If the spatial location of the spinel nuclei is slightly changed to be situated in the local stress maximum created by a coexisting spinel grain under otherwise identical conditions as above, it is not very surprising to find a more or less opposite behaviour in the interplay of the grains (Fig. 5.5). In difference to the simulations above, the temperature and the surface energy do not interfere with the development of the grain shapes and a far field influence of the stress field is not recognizable.

The basic influence of the grains on each other is a compensation of the dominating stress concentration at the tips of the spinel fingers. Hence the grains coalesce when their tips pass each other and cease to grow at the respective locality. In effect they continue to grow as a single spinel grain.

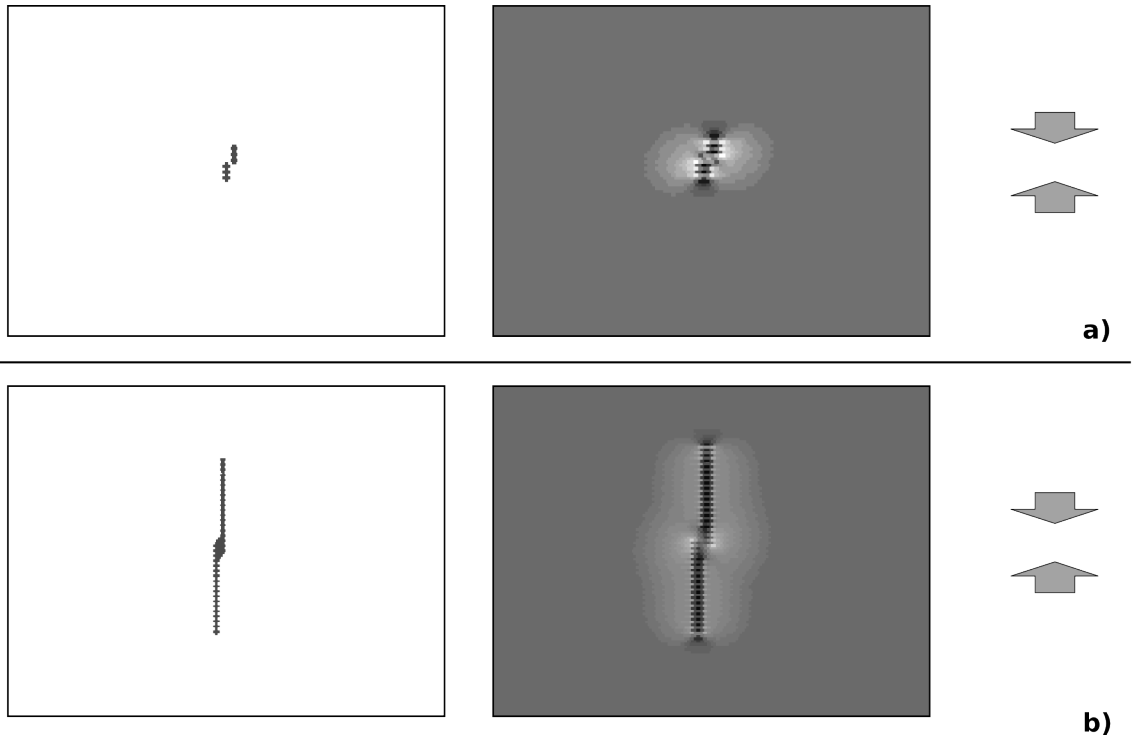

Figure 5.5: Merge of neighbouring spinel grains under vertical uniaxial compression. The image on the left displays the outline of the spinel grain, the image on the right the mean stress. (a) Shortly after nucleation at timestep 90. (b) After merging at timestep 225.

6 Spinel grain morphologies in presence of inherent disorder

6.1 Aim and structure of the chapter

Real matter can not be expected to be as homogeneous as assumed in the previous chapter. Therefore, this chapter is about spinel structures forming in a more realistic material representation within the model. In order to mimic the inherent disorder of the material a gaussian quenched noise is induced on the elastic properties of the olivine host. This leads to a certain roughness of spinel grains, in contrast to the even grained spinel structures which resulted in the previous chapter.

The most important aim of the chapter is the comparison of structures resulting from the simulations with spinel structures obtained in high pressure experiments. This is achieved by a comparison of the fractal dimensions of spinel structures from the computer experiments and from high pressure experiments performed by Riggs and Green (2001, [88]). Further, the most important control parameters for spinel grain shapes will be discussed.

The chapter is structured as follows:

- Sec. 6.2 gives a general description of the effects of a olivine host with an gaussian distribution on elastic material-properties on the resulting olivine/spinel structures.
- A short discussion of useful analytical methods for the resulting rough structures is given in Sec. 6.3.
- Sec. 6.4 describes the basic settings of the series of computer simulations and gives a detailed description of the resulting spinel structures. This is followed up by a summarizing discussion of the resulting structures and the important influences on the shape of spinel grains.

- Sec. 6.5 discusses the fractal analysis of the spinel structures from the computer model. This includes a generalizing discussion of the mathematical/phyiscal meaning of fractal dimensions and the procedure of the fractal analysis.
- Sec. 6.6 is about the comparison of the fractal dimensions obtained from the computer experiments and from high pressure experiments.
- The chapter is concluded in Sec. 6.7 with a short discussion of a localization phenomenon on spinel boundaries, which was occasionally encounterd in simulations involving disordered olivine hosts.

6.2 Effects of a statistically heterogeneous olivine host on spinel growth

The presence of inherent disorder in real materials can be expected to have a considerable impact on the evolution of grain shapes on small scales. In order to mimic more natural conditions in the simulations, the experiments described and analysed in this section were performed with a gaussian quenched noise on the Youngs moduli of the mechanical elements in the spring network. This is a common aproach in order to mimic the presence of inherent disorder in the host material, caused e. g. by impurities and point defects (Dupas et al., 1994, [25], Malthe-Sørenssen, 1998, [70], Sung, 1976, [98, 97]).

The quenched noise on the elastic properties of the spring network adds a random-element to the growth process of a spinel grain. Objects generated by a setting like that will obtain a fractal structure (Vicsek, 1992, [102]), somewhere between a surface fractal and a pore fractal, following the classification of Pfeifer and Obert (1989, [80]) (Fig. 6.1).

The local stress on the olivine/spinel interface, which is a major driving force of the grain boundary migration, is determined by the statistical mean μ_d and the standard deviation σ_d of the gaussian distribution on the elastic parameters of the parent phase. Since stress is a linear function of the strain and the Youngs modulus, the importance of the local elastic parameters for inhomogeneities within the stress field increases proportional to the externally applied deformation of the system.

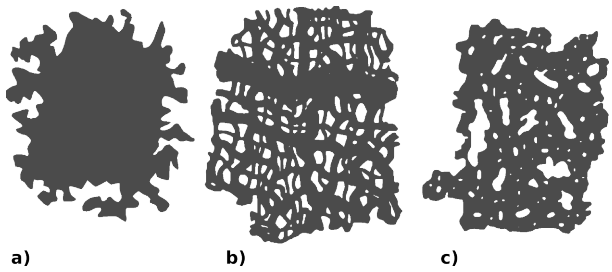

Figure 6.1: Pfeifer classification of surface fractals (after Goyet et al., 1996, [38]). (a) Surface fractal, (b) mass fractal, (c) pore fractal.

6.3 Analysis and classification of the roughness of spinel structures

The description of spinel grain shapes in case of a homogeneous parent phase as in Chap. 5 can be easily done by a classical mineralogical or geometrical description. This procedure can not be applied to spinel forming in olivine with an inherent disorder on the material parameters, due to the roughness of the grain surface. Additionally, the growth of a spinel grain is a time-dependent process, where the exact outline of the grain is constantly under change.

The analysis of such structures is ideally done by means of the fractal dimension, which allows the classification of rough, ideally self-affine objects by a single numerical quantity. The fractal dimension allows an easy examination of the temporal development of the spinel structure, the formulation of the limits of the process and predictions about the further evolution of the grain shape.

A further advantage is the easy comparability with the fractal dimension of olivine/spinel structures from high pressure experiments, which were analysed by Riggs and Green (2001, [88]).

A descriptive approach to the classification of fractal structures is the already introduced classification of Pfeifer and Obert (1989, [80]), which is outlined in Fig. 6.1.

6.4 Computer experiments

6.4.1 Base settings and boundary conditions

The simulations were performed on the basis of a 200×200 hexagonal spring network, scaled to a side length of 10 μm, which corresponds to the size of various experimental investigations of the resulting olivine/spinel microstructures (Dupas et al., 1994, [25], Vaughan et al., 1984, [101], Riggs and Green, 2001, [88]). The inherent disorder on the olivine parent is simulated by a gaussian distribution on the values of the spring constants α, with a statistical mean value $\mu_d = 1$ and a variable standard deviation σ_d.

Two simulation-series were calculated, with $\sigma_d = 0.2$ and $\sigma_d = 0.5$, respectively. The choice of σ_d must be considered rather arbitrary, since no values for natural olivine could be retrieved from the available literature. $\sigma_d = 0.2$ is a standard value which is often applied in simulations where a quenched noise on the elastic properties of a material is involved (e. g. Köhn, 2008, [60]), while $\sigma_d = 0.5$ can be considered an extreme value and serves as a counterpart to the absence of a distribution in the previous chapter.

According to examinations of spinel formed in high pressure experiments which were described by Dupas et al. (1994, [25]), heterogeneities in olivine will be erased and homogeneously overprinted after the transition to spinel. Consequently, a homogeneous spring constant will be assigned to those springs which are part of spinel grains in the simulations.

In order to create hydrostatic stress field homogeneous biaxial compression is applied on the system, the strain is set to a finite compression $\epsilon_y = \epsilon_x = 0.002$ per timestep. If differential stress shall be created, the vertical component of the deformation is set to $\epsilon_y = 0.002$, combined with horizontal finite compression of $\epsilon_x = 0.001$, thus the vertical strain is double the horizontal strain. If visco-elasticity is applied, a single timestep in the simulation is set to $t = 10^{11}\ s$, combined with a viscosity $\eta = 10^{22}\ Pa \cdot s$ of the olivine host (cp. Sec. 3.2.1).

Effects of competitive grain growth are ignored, instead the grain boundary migration starts from a single seed.

In order to derive the particular influence of individual parameters, the experiments consider the influence of latent heat release of the reaction, the surface energy and the presence of viscous flow separately in every series of simulations. In addition, these

factors are combined in one run of every series of simulations.

6.4.2 Spinel structures developing under hydrostatic stress

The spinel structures, which resulted from simulations under hydrostatic conditions, are compiled in Fig. 6.2, which is organized according to the parameters included in the simulations. Each subfigure opposes grains developed in presence of a standard deviation of $\sigma_d = 0.2$ directly with grains developing if $\sigma_d = 0.5$. The effect of the standard deviation on the principal grain shape is generally large, and leads from almost even grained spinel structures with $\sigma_d = 0.2$ to a large alteration of the grain structure if $\sigma_d = 0.5$.

The most eye-catching effect of a quenched noise on the spinel structure under hydrostatic conditions is a drastic increase of the interior porosity (Fig. 6.2 (a)).

If the surface energy or the thermal energy are considered in the simulations, a transition from a pore fractal to a surface fractal is initiated and the principal outline of the grain perimeter tends to display dentritic structures.

If a visco-elastic spring network is applied, the effects of elastic heterogeneities on the spinel structure are drastically reduced (Fig. 6.2 (d)). A distribution with $\sigma_d = 0.2$ has no observable effects on the grain shape under these conditions, compared to grain growth in a homogeneous host material. If σ_d is set to 0.5, the grain shape shows first signs of symplectite-type growth. However, this effect is far more pronounced in the presence of differential stress, described below.

In experiments considering all individual parameters from above in combination, effects of the distribution become negligible. Grain shapes for both σ_d can be described as almost non-porous surface fractals.

6.4.3 Spinel structures developing under differential stress

Spinel structures developing under differential stress are compiled in Fig. 6.3, sorted after the standard deviation σ_d and the parameters, which were considered in the indivual simulation.

While the presence of inherent disorder under hydrostatic stress led primarily to an increase of the porosity of the spinel interior, the main effect in the presence of a differential stress regime is a roughening of the grain surface (Fig. 6.3 (a)). This

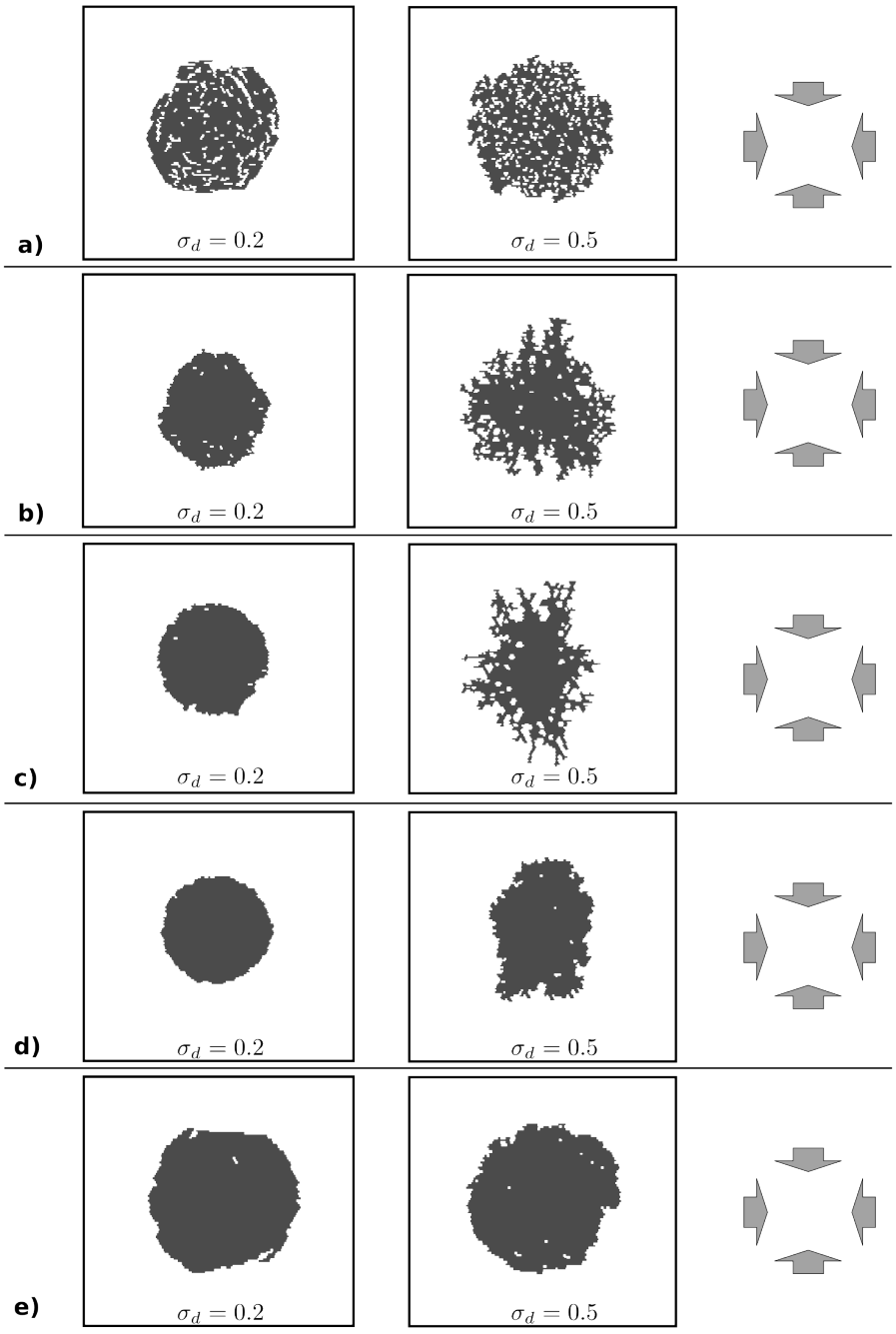

Figure 6.2: Spinel structures developed under hydrostatic stress, using two distributions on the spring parameters of the spring network. In each subfigure the left image depicts structures with $\sigma_d = 0.2$, opposed with $\sigma_d = 0.5$ to the right. All structures developed at timestep 5500. (a) Stress driven growth. (b) Considering surface energy. (c) Thermal energy. (d) Visco-elastic spring network. (e) Combination of all parameters.

is due to the large surface/volume ratio of the intensly elongated basic grain shapes developing under differential stress (cp. Chap. 5).

While the influence of the thermal energy and the surface energy are negligible if the standard deviation $\sigma_d = 0.2$, the consideration of these parameters induces a pronounced thickening and pore-formation of the spinel structure if $\sigma_d = 0.5$ (Fig. 6.3 (b) and (c)).

In simulations including visco-elasticity, spinel growing in an olivine host with a standard deviation of $\sigma_d = 0.2$ develops a dense structure. The grain shape is diamond-shaped if the effects of thermal and surface energy are excluded from the calculations, and becomes almost isometric if they are included.

In case of a large standard deviation of 0.5, a visco-elastic springnetwork leads to almost symplectitic growth pattern of the spinel structure with a large porosity (Fig. 6.3 (d)). Adding thermal energy and surface energy to this simulation reduces the symplectitic component of the spinel structure and leads to the formation of a surface fractal (Fig. 6.3 (e)).

6.4.4 Generalizing description and influences on the resulting spinel structures

In summary, the surface structure of spinel grains is influenced by the following parameters, where viscous material behaviour must be regarded as the most dominant influence:

- The basic grain geometry, which is dictated by the externally applied deformation of the system (Chap. 5). If the surface/mass ratio is low, i. e. in the presence of uniaxial stress, the resulting spinel grain tends to develop a rough surface rather than a porous interior. Under hydrostatic stress, if the resulting spinel grain is isotropic, the surface roughness tends to be rather unaffected, compared to the developing interior porosity.

- The value of the standard deviation σ_d. Increasing this parameter increases the effects on the structure which are encountered from lower standard deviation, rather than developing own characteristic features. An exception is the effect on localisations on the grain boundary, which may occasionally form dentritic structures (cp. 6.7).

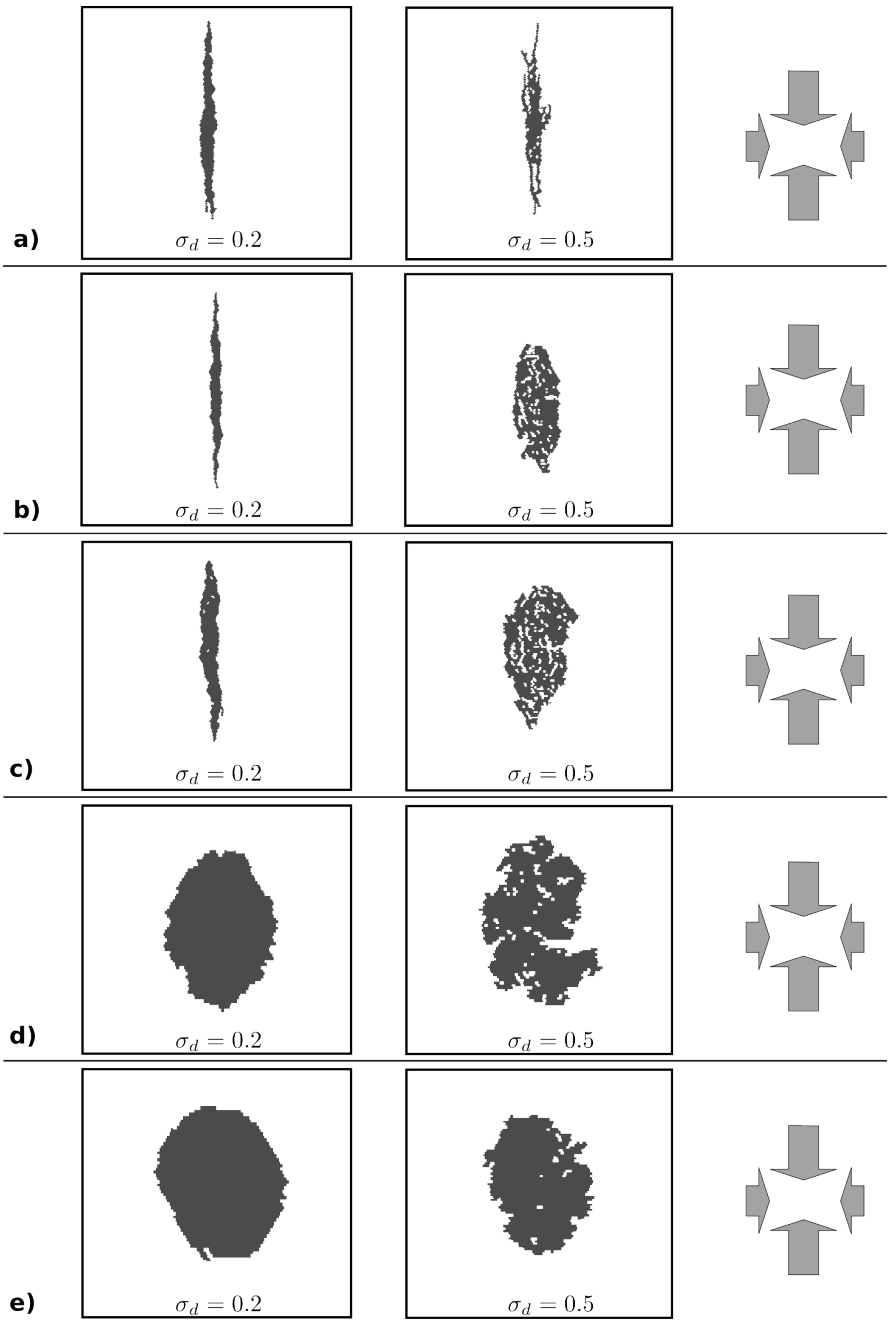

Figure 6.3: Spinel structures developed under hydrostatic stress, using two distributions on the spring parameters of the spring network. In each subfigure the left image depicts structures with $\sigma_d = 0.2$ to the left, $\sigma_d = 0.5$ to the right. Images (a) and (b) developed at timestep 1800, (c) - (e) at timestep 2300. (a) Stress driven growth. (b) Including surface energy. (c) Including thermal energy. (d) Visco-elastic spring network. (e) Combination of all parameters used in (a) - (d).

- The surface energy and the latent heat release tend to diminish the interior porosity of a grain, rather than affecting the general outline of the transformation zone. This effect is due to the large surface energy associated with small residual olivine inclusions in spinel, and the resulting large energy minimization if these inhomogeneities within the spinel structure are removed. The concentration of thermal energy in the interior of the grain is much larger than on the surface, where thermal energy will dissipate (Fig. 6.4).

- If visco-elasticity is added to the spring network, the stress field will be partly homogenized (Fig. 6.5). Thus visco-elasticity counteracts the effects of the quenched noise and is in favour of a general straightening of the olivine/spinel interface. The remaining stress distribution is characterized by comparatively extended gradient fields around nodes with a large deviation from the elastic mean. This effect appears to be more distinct if the externally applied stress is differential, which leads to symplectitic growth of the spinel grain (Fig. 6.2 and Fig. 6.3 (d) and (e)).

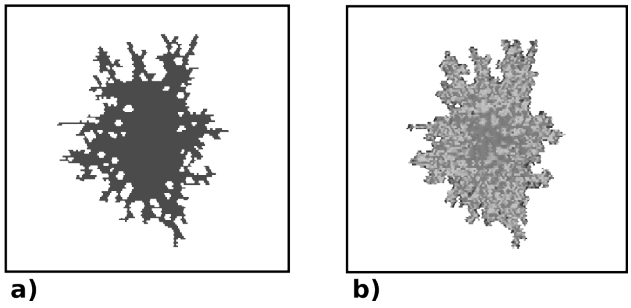

Figure 6.4: (a) Grain shape and (b) temperature distribution at timestep 5000 of a spinel grain developed under biaxial compression with $\sigma_d = 0.5$. The displayed temperature interval is 1000-1230 K, darker colours mean higher temperatures.

6.5 Fractal analysis of the spinel grain topography

6.5.1 Fractal analysis

The calculation of the fractal dimension of the spinel grains was performed using self-written python-scripts, which calculated the box-counting fractal dimension D_b directly

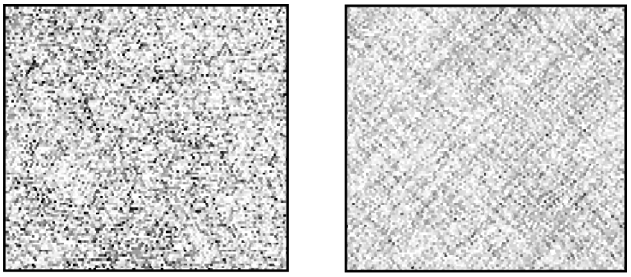

Figure 6.5: Mean stress distribution after 50 timesteps, using a standard deviation $\sigma_d = 0.5$ for the youngs modulus of individual nodes. (a) for an elastic spring network, (b) for a visco-elastic spring network, with $t = 10^{11}$ s and cubical compression $d = 0.004$ per timestep.

from the native output files of the *elle* software package. The box-counting dimension is in particular suitable for sets of discrete points, as the output of the computer simulations.

The mathematical definition of D_b for a set of an infinite number of points in 2D is as follows: divide an arbitrary area, which contains the point set, into square cells of side length l, where $N(l)$ denotes the number of squares that contain one or more points of the point set. Then D_b of the point set is defined as (Faloutsos and Kamel, 1997, [27]):

$$D_b = \lim_{l \to 0} \frac{\log N\,(l)}{\log\,(1/l)}. \tag{6.1}$$

This scheme is adapted to a finite set of points by computing a boxcount-side plot, where $\log N(l)$ is plotted versus $\log l$ for a selected interval $l_1 < l < l_2$ with l_1 greater or equal than the resolution of the computer simulation. If the structure is indeed fractal, this will give a straight line with a slope D_b.

When calculating the mass dimension D_M, which is a measure for the required space of the fractal structure, every point of the set is used. To calculate the fractal boundary dimension D_S, which is a measure for the roughness of the structure, only points situated at the boundary of the structure are taken into account by the box counting algorithm.

In the here-undertaken simulations it is possible that a certain error is introduced by the mismatch of the hexagonal spring network and the square lattice used for the

calculation of the boxdimension. However, a careful choice of l_1 and l_2 for Eq. 6.1 is able to diminish this effect almost entirely. The encountered standard deviation in the calculation of fractal dimensions was between 1% and 7%.

6.5.2 Meaning of the fractal mass and the fractal surface dimension of an object

Knowledge of the fractal mass dimension and the fractal surface dimension is able to provide three kinds of information:

- Due to the random properties of the spinel grains in the simulations, a direct comparability of clear morphological features of simulated and real structures must remain speculative to some extent. The fractal dimension is a good parameter in order to test the similarities of the structures, since it abstracts from specific details of the grain shape.

- The numerical simulation of a growth process, even if it is based on the physics of the process itself - as in this work - and not on a more or less physically meaningless mathematical analogy, as regularly applied in the study of fractal growth (cp. e. g. Vicsek, 1992, [102] or Lasaga, 1998, [64]) involves inevitable mathematical/physical simplifications, for instance lattice and discretisation effects. This adds up to simplifying assumptions in the kinetic equations, for instance the assumption of a perfectly spherical nucleus. If the development of the fractal dimension during the simulation approaches a limit, we may safely assume that these effects are minimized, due to the number of unit cells/particles which are involved and act like an improvement of the resolution of the structure. In addition, physically questionable start conditions will be adjusted by the growth process.

- The fractal dimension gives us a clear numerical quantity, to evaluate the influence of changing parameters on the evolution of the shape of structures. This is particularly true, if the difference is indistinguishable for a human observer.

The fractal mass dimension allows a characteristic statement about the space requirement $\rho(r)$ of a circular structure with radius r by the relation

$$\rho(r) \sim \frac{M(r)}{V(r)} = \frac{r^{D_m}}{r^2} = r^{D_m - 2}, \tag{6.2}$$

where D_M is the fractal mass dimension, $M(r)$ the area of the fractal structure and $V(r)$ the area of a smooth object with the same radius r with the Euclidean embedding dimension d (Nordmeier, 1999, [75]). The more the fractal mass dimension approximates the Euclidian embedding dimension 2, the better is the planar preoccupation of the fractal object. Consequently an isometric has a large mass dimension close to 2, while dentritic structures are characterized by smaller dimensions, in extreme cases slightly above 1.

In contrast, the fractal surface dimension D_S of a fractal object is a characteristic quantitiy for the surface roughness of the structure.

6.5.3 Results of the fractal analysis

The results of the analysis of the fractal dimensions are compiled in Fig. 6.6, where they are sorted according to the externally applied stress on the system and the standard deviation of the parent phase. In order to evaluate the convergence towards a stable limit of the fractal dimension, the dimension is plotted as a function of the timestep in the respective simulation. Below the development of the fractal dimension will be shortly summarized.

Convergence of the fractal dimension towards stable limits

The fractal dimensions, calculated from the output of the simulations, are clearly convergent towards a stable limit with progressing timesteps. However, not every displayed fractal dimension in Fig. 6.6 did actually reach the stable limit during the duration of the simulations, which were stopped after 5500 timesteps. This concerns in particular the fractal surface dimension under purely elastic conditions in Fig. 6.6 (a), where the limit can only be estimated to approximate a value slightly above 1.6. The general limit of convergent fractal dimensions is situated between $D_M = 1.5$ and $D_M = 1.9$ in case of mass fractals and $D_S = 1.3$ and 1.6 for surface fractals, respectively.

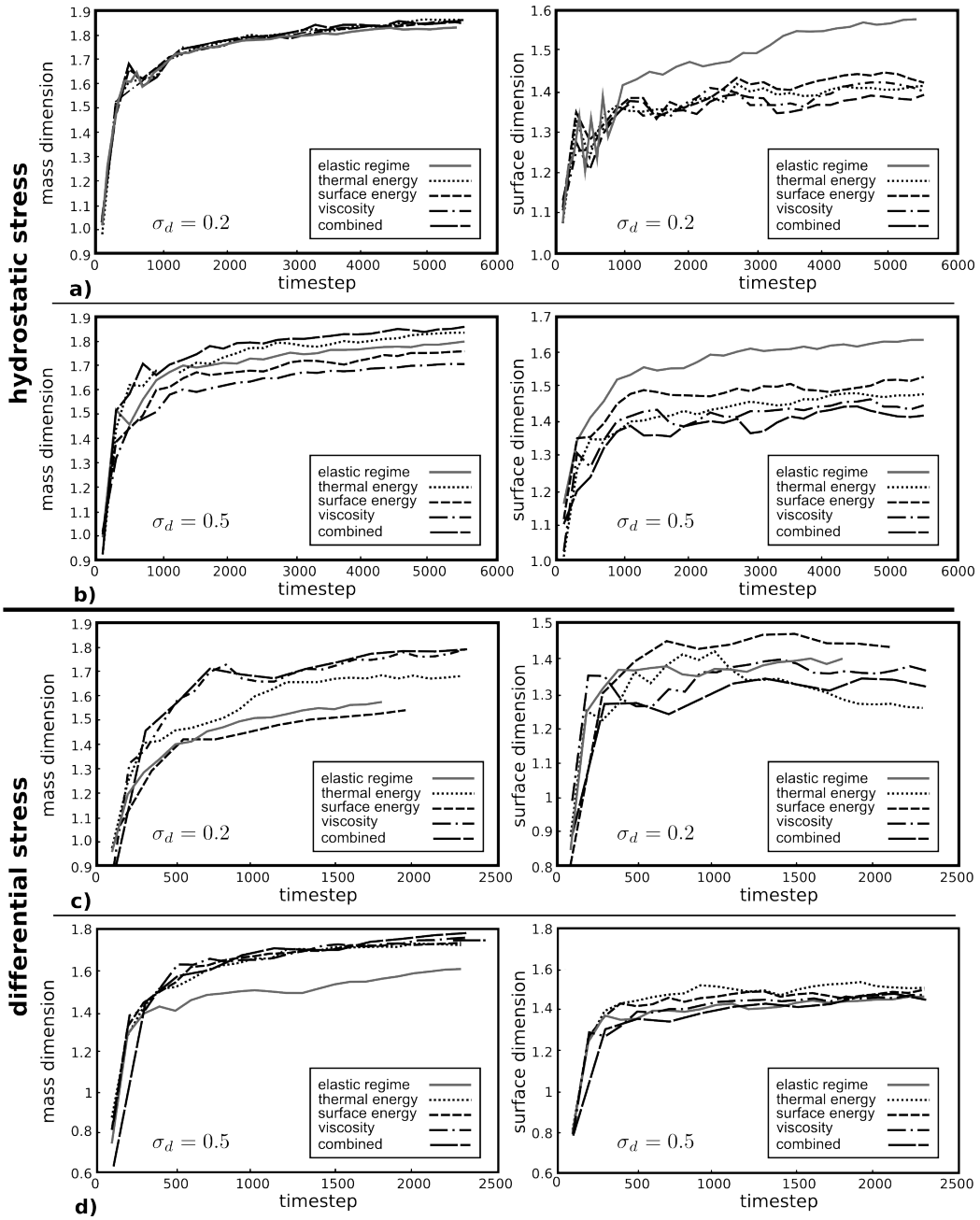

Figure 6.6: Temporal evolution of fractal mass dimension (left) and surface dimensions (right), obtained from the series of computations in this chapter. Subfigures (a) and (b) are in the presence of hydrostatic stress, (b) and (c) in presence of differential stress. Effects of every parameter which was applied in the simulations is displayed separately (i. e. surface/thermal energy and visco-elasticity), in addition to purely elastic conditions and a combination of all used parameters.

Convergence is faster under differential stress conditions, where a stable value is commonly reached after approximately 500 timesteps, than under hydrostatic conditions, where the static limit is typically reached after approximately 1000 timesteps. This difference can be explained by the strongly anisotropic structure-building effect of directed stresses.

Development of fractal mass dimensions

Considering the fractal mass dimension, the value is dictated by the tendency of the evolving grain to form dense isometric structures (cp. Eq. 6.2). As a consequence, the mass dimension of spinel forming under hydrostatic conditions has a strong tendency to acquire large fractal dimensions approximationg the embedding dimension 2. Increasing the standard deviation to 0.5 leads to a decrease of the fractal dimension, due to an intense roughnening of the surface, on the edge of forming dentritic structures.

The inclusion of additional factors, i. e. of the surface energy, the thermal energy and visco-elasticity, makes virtually no difference for the fractal mass dimension in presence of a low distribution. Applying a larger standard deviation on the system affects the dimension by localization effects on the grain perimeter, induced by the latent heat release and the surface energy and leading to a smaller dimension as well as by the straightening effect of the presence of viscosity in the spring network, leading to an increase of the dimension.

These effects on the mass dimension are partly reverted under uniaxial conditions, since the strongly elongated basic grain shape diminishes the fractal mass dimension considerably to approximately 1.5 if $\sigma_d = 0.2$. Increasing the standard deviation as well as considering surface energy, thermal energy and visco-elasticity in the calculations of the grain shape broaden the grain shape and lead thus to an increase of the fractal mass dimension.

Development of fractal surface dimensions

Under hydrostatic conditions the fractal surface dimension is just slightly lower in the presence of a small standard deviation than in presence of large σ_d, though the convergence is must faster if σ_d is large, due to the larger control of the growth structure by the inherent disorder. Also, despite large discrepancies of the grain shape between the different simulations, the influence of latent heat release, surface energy and visco-

elasticity converges towards similar values between 1.4 and 1.5, though slightly lower if the standard deviation is small.

If exterting a differential stress on the system, the fractal surface dimension is in the range of 1.3 to 1.5 if $\sigma_d = 0.2$ and comverges towards 1.4 for $\sigma_d = 0.5$. The relative large interval in case of a small distribution is due to the large scatter of the fractal dimension in the presence of surface energy, thermal energy and viscosity, where the thermal energy increases the fractal dimension while it is lowered by the surface energy.

If σ_d is increased to 0.5, the dominant factor for the fractal dimension is clearly the statistical distribution on the elastic spring parameters of the spring network, since the development of the fractal dimension is almost identical for every considered parameter.

6.5.4 Influence of externally applied stress and the standard distribution σ_d on the fractal dimension of the grain shape

Fractal mass dimension D_M

The fractal mass dimension displays the general space requirements of the structures, and is therefore sensitive to changes of the general geometry of the grain shape.

The type of stress, which is externally applied on the system, has a dominant influence on the fractal mass dimension, lowering it from up to $D_M \approx 1.85$ under hydrostatic conditions to approximately 1.5 - 1.6 under differential stress. This effect is easily explained by the very elongate grain shapes which form in the presence of differental stress, compared to the isometric grain shape created by hydrostatic stress.

If the effect of the externally applied stress is altered by the presence of viscous material properties, we encounter a reduction of the fractal mass dimension under hydrostatic stress, due to a straightening of the surface structures, in contrast to an increase of the mass dimension under differential stress conditions due to the formation of more isometric grain shapes.

The standard distribution has a significant influence on the fractal mass dimension, which is lowered by approximately 0.1 if σ_d is increased from 0.2 to 0.5.

Fractal surface dimension D_S

The surface dimension is strongly affected by the surface roughness and the interior porosity of spinel grains.

A principal difference between the stress regimes is the influence of surface energy, thermal energy and visco-elasticity on the relative development of the fractal dimension, whether mass related or surface related.

Comparing the principal influence of externally differential stress - which is ideally 0 under hydrostatic conditions - we encounter a tendency towards lower values of the fractal surface dimension with increasing differential stress.

The effect of visco-elasticity is a reduction of the dimension under hydrostatic conditions, due to a homogenization of the stress field. Surprisingly, if differential stress is externally exerted on the system, no effect on the surface dimension can be encountered, independent from the standard distribution. This appears to be caused by a reduction of the rougness of the grain perimeter on one hand, coupled with an increase of the interior porosity of the spinel grain.

The influence of the standard deviation on D_S is a reduction of the scatter of the fractal dimension if surface energy, thermal energy and visco-elasticity are included in the calculations.

6.6 Comparison of fractal dimensions obtained from the computer model and from high pressure experiments

6.6.1 Fractal dimensions of olivine/spinel interfaces obtained in high pressure experiments

Riggs and Green (2001, [88]) determined the fractal surface dimension (D_s) of several transformation zones of spinel in olivine, which they obtained from high pressure experiments using Mg_2GeO_4 as a substitute for silicatic forsterite (Fig. 6.7). They obtained values for D_s between 1.17 and 1.35 for various sections of interest through the transformed material. The fractal dimension of the transition zone in Fig. 6.7 for instance amounts to 1.17.

The fractal dimensions given by Riggs and Green (2001, [88]) are not fully comparable to the dimensions obtained from structures in the simulations. For once, the fractal dimension of the simulated spinel/olivine interface was determined for the entire material, instead for selected sections of interest. Secondly, the fractal dimension of a growth fractal undergoes a process, where it approaches asymptotically some limit for the fractal dimension, which usually starts from some very small value. This is

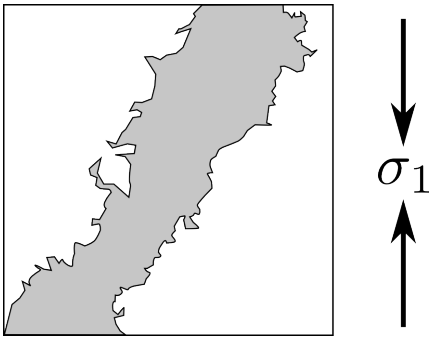

Figure 6.7: Spinel transformation zone of spinel (grey) in olivine. Image after Riggs and Green (2001, [88]), who performed high pressure experiments in Mg_2GeO_4-olivine. The fractal surface dimension $D_s = 1.17 \pm 0.03$.

true for natural fractals as well as numerical fractals, although for different reasons. It is, however, not clear, for which stage of the experimental transformation process the fractal image analysis of Riggs and Green (2001, [88]) was performed.

6.6.2 Comparison with simulated spinel structures

Comparing the surface dimensions calculated from the spinel structures in the computer experiments with the surface dimensions which were obtained by Riggs and Green (2001, [88]) for the olivine/spinel interface in transformation zones, the best match to their results is reached in simulations using differential stress combined with a standard distribution of $\sigma_d = 0.2$ on the elastic parameters of the olivine host. The resulting fractal surface dimensions in the experiments are in the interval between 1.3 and 1.5, while surface dimensions calculated by Riggs and Green are between 1.17 and 1.35. Experiments on a visco-elastic spring network were ignored in this context, because strain rates in high pressure laboratory experiments are far to high for flow within the host material.

The values from the computer experiments appear still high in comparison. Under the assumption of accurate computer simulations, this can be explained by each or a combination of the following arguments:

- Riggs and Green determined the fractal surface dimension for hand-selected sections of their samples, where structures displayed a large surface/mass ratio according to their research interest. In difference the determination of the surface

dimension of structures resulting from the simulations included the complete structure.

- In agreement with Sec. 6.5.4 above, the surface dimension of the structures generated in simulations will be lowered if the standard deviation of the quenched noise on the elastic parameters of the material is reduced. Riggs and Green (2001, [88]) synthesized an especially pure material for their experiments, thus the small fractal surface dimension they achieved can be probably partly related to the low statistical distribution of elastic parameters.

- Again in agreement with Sec. 6.5.4, the surface dimension will be lowered if the value of the externally applied differential stress is increased. The exact amount of the differential stress applied in the experiments of Riggs and Green is unknown, thus a discrepancy with the conditions in the computer simulations is highly probable.

6.7 Dentritic localisation-structures on spinel grain boundaries

Among the simulations described above, an interesting localization phenomenon appeared when the standard deviation σ_d was set to 0.5 in an olivine host under differential stress. On a visco-elastic spring network and under consideration of the surface energy and elastic energy in the rate equations the spinel grain began to develop stable dentritic growth at approximately timestep 2500 (time-lapse sequence in Fig. 6.8 below and Fig. 6.3 (e)). The associated transition from a relatively even shaped grain to a dentrite structure is obvious in the plot of the temporal evolution of the fractal dimensions as well (Fig. 6.9).

A similar phenomenon was frequently encountered if a spinel grain with an even surface was manually inserted into a spinel host with a quenched gaussian distribution on the spring constants in the spring network. Fig. 6.10 displays the localizations forming on a spinel-semicircle which was manually introduced into an olivine parent with a standard distribution $\sigma_d = 0.2$ on the spring parameters of the lattice.

This localization phenomenom deserves certainly more attention than given in this work. A probable explanation of the dentritic structures is as follows. After forming

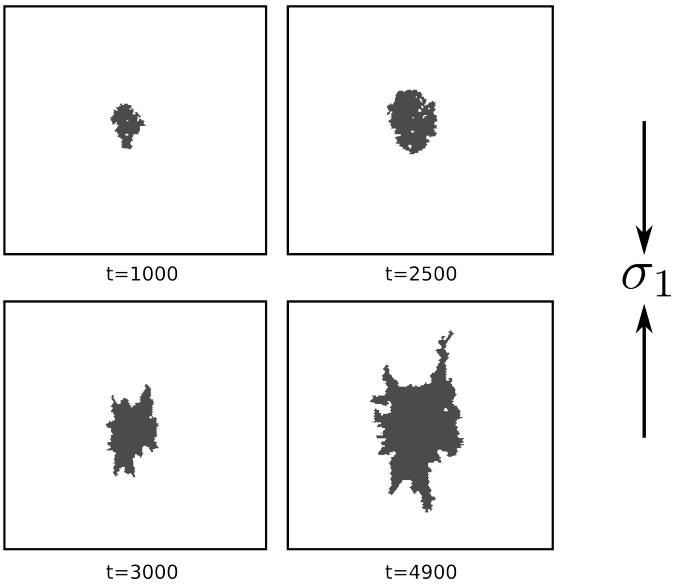

Figure 6.8: Time-lapse sequence of a spinel grain displaying strong localization effects. Between timestep 2500 and timestep 3000 the spinel structure starts to develop dentritic structures, which can be clearly seen in the fractal dimension (Fig. 6.9). σ_d of the olivine host is 0.5, stress is differential with a vertical σ_1.

initial bulges on the spinel surface, determined by local maxima of the stress distribution, the reaction is apparently mainly driven by stress concentrations at the tips, leading to a local runaway and thereby to the pronounced localization and elongation of dentritic surface structures.

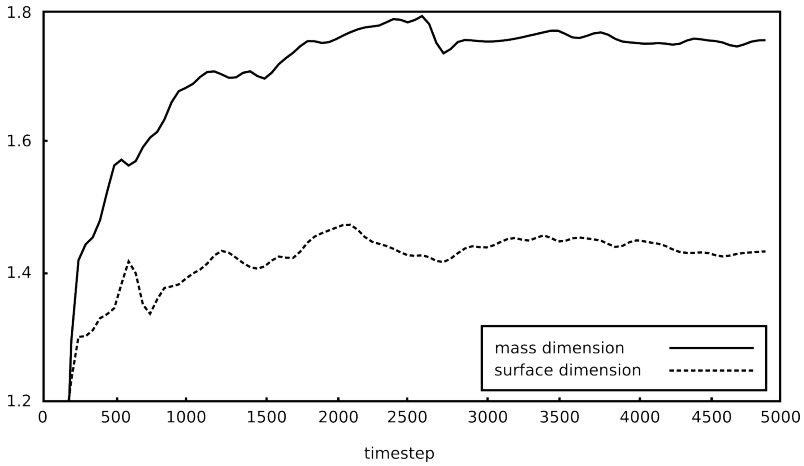

Figure 6.9: Development of the fractal mass dimension and the fractal surface dimension of the spinel grain in diplayed in Fig. 6.8. Due to a change of the general growth behaviour both dimensions display a significant decrease around timestep 2500.

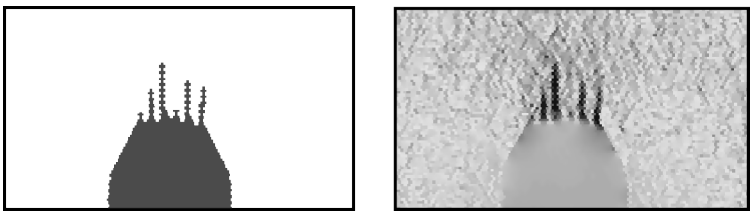

Figure 6.10: Localization in form of dentritic structures on a regular semicircular spinel grain towards the direction of σ_1 at timestep 500 under vertcal uniaxial compression. The standard deviation within the olivine host is $\sigma_d = 0.2$, and the normal stress on the grain boundary is the only contribution to the driving force considered in the growth algorithm.

7 Spinel network formation in olivine-bearing assemblages

7.1 Overview

7.1.1 Aim of the simulations

Previous computer simulations of the olivine→spinel transition at 400 km depth in the upper mantle, which have been performed by e. g. Riedl and Karato (1997, [87]), Däßler (1996, [21]) and Rubie and Ross (1994, [91]) were usually restricted to quantitative statements about the absolute content of spinel in a pure olivine host, which was calculated from kinetic rate laws. The restrictions of these models are dictated by the basic assumptions of kinetic theory itself, which assumes a homogeneous parent material with identical growth conditions at every point. Thus, these models pretend that growth of spinel grains is perfectecly circular once a nucleus formed, while growth anisotropies, either caused by heterogeneities of the material or anisotropies of the stress field are necessarily ignored. The same is true for the nucleation process, which remains essentially random in space, even if the statistical consequences of material heterogeneities are considered in the calculation of reaction rates.

These simplifications are unavoidable and not necessarily problematic if it is the single aim of a simulation to determine orientation-independent material parameters, such as the absolute amount of spinel in the system or the determination of the average grain size (e. g. Däßler et al. (1996, [21])). But they are insufficient when it comes to the calculation of network formation and system percolation (e. g. Riedl and Karato, 1997, [86]).

Olivine is commonly regarded as the rheology-defining consitutent of mantle material, given its abundance and its relative plastic weakness (Karato et al., 1998, [53], Ita and Stixrude, 1992, [47]). Therefore we can assume that a major change of the rheology of mantle rocks occurs, when the olivine→spinel transition within an olivine

bearing host rock is at the point of forming throughgoing load-bearing networks or potential .

The aim of the simulations discussed in this chapter is to calculate time-lapse sequences of microstructures related to the olivine→spinel transition, forming in material of pyrolitic composition and with the corresponding mineral assemblage at 400 km depth. The non-reactive mantle minerals in the series of simulations are assumed to be pyrope and enstatite, in agreement with the pyrolitic model (Ita and Stixrude, 1992, [47], Ringwood, 1975, [90], Irifune and Ringwood, 1987, [46], Irifune, 1987, [45]). In addition to the series of simulations using olivine bearing poly-mineralic assemblages as parent phase, we calculated the microstructures formed by spinel in monomineralic olivine under different types of externally applied deformation for comparison.

However, it is explicitly not the aim of this chapter to present a quantitative analysis of the forming microstructures, but to show the influence and the significance of a more realistic mantle rheology for the development of the olivine→spinel transition.

7.1.2 Experimental setup

Two different series of computer simulations were calculated. One series calculated the olivine/spinel intergrowth in a system consisting of homogeneous olivine under different settings for the externally applied strain. The second series was calculated for a heterogeneous system under hydrostatic stress where we altered the mineral assemblage in different runs. The following detailed descriptions below are therefore sorted according to the simulated mineral assemblages and the externally applied strain.

The experiments were calculated on a 100×100 spring lattice, which was scaled to a system size with a side length of 38 mm. The average grain diameter is in the order of $3 - 4$ mm, in agreement with estimates for the maximum grain size of rocks in the upper mantle (Riedl and Karato, 1996, [86]). We assumed that the normal stress on the olivine/spinel interface is the single critical parameter for the evolution of spinel grains on this scale. Thus, in difference to previous chapters, we did not consider the effects of the surface energy acting on the grain surface and the latent heat release of the reaction in the calculations.

Simulation series on the basis of a homogeneous host phase

Externally applied strain and mineral composition The host phase used in this series of experiments consisted of monomineralic olivine with identical elastic properties at every point. The computer experiments used three different types of externally applied strain, which were:

- uniaxial vertical strain, producing a stress field with a pronounced orientation,
- biaxiaxial compression, leading to hydrostatic stress conditions, and
- a combination of simple shear and biaxial compression. Biaxial compression was applied in order to reach the critical stress of the phase transition without changing the geometry of the lattice.

Nucleation The Johnson-Mehl model (Christian, 1981, [18]) for nucleation in a homogeneous parent material was, where a constant moderate overpressure of 163.3 MPa and 1000 C were assumed. Under these conditions 160 spinel grains are formed in a system of the given side length of 38 mm. Nuclei of these grains are inserted at random localities (cp. Sec. 3.4.1 and Sec. 2.3.2 for a summary of the approach and the governing equations).

The Johnson-Mehl model assumes nucleation to occur only once, at the beginning of the transformation. Subsequently only grain growth is considered (cp. Sec. 3.4.1).

Simulation series on the basis of a heterogeneous host phase

In order to reduce the complexity of the system and the computation time, which is considerably higher in the presence of several simulated mineral phases in the system, the simulations considered only hydrostatic stress conditions.

All of the computer simulations were calculated on the basis of an elastic spring network. In the most interesting case, an assemblage consisting of a combination of all considered mantle minerals, the computer simulations were performed for both, an elastic as well as a visco-elastic spring network.

Mineral assemblages The mineral composition of the mantle material in the simulations is a simplification of estimates from Ita and Stixrude (1992, [47]) (compiled

in Tab. C.15), with the difference that we replace clinopyroxene with orthopyroxene. Hence 20 % of the mineral assemblage consists either of the garnet phase pyrope or the orthopyroxene variety enstatite.

The computer model was set up to calculate the effects of enstatite and garnet separately as well as combined, and compare them with spinel microstructures in a homogeneous model. We applied a random algorithm to assign the elastic properties of the considered mineral phases to the predefined graines in the *elle*-file, where the elastic parameters of the garnet pyrope and of enstatite are randomly assigned to 20% of the total number of grains. This leads to a total of either 80% or 60% olivine, depending on the number of considered phases.

However, due to the random-assignment of mineral properties the mineral proportions are not constant but vary in certain limits from simulation to simulation.

The elastic anisotropy of olivine is accounted for by putting a small random distribution on the Youngs modulus of entire olivine grains, applying a statistical mean $\mu_d = 1$ on the spring constants (α) and a standard deviation $\sigma_d = 0.1$.

Enstatite has a Youngs modulus considerably smaller than the Youngs modulus of olivine, while pyrope is comparatively harder. Thus, the presence of these minerals has opposite effects on the distortion of the stress field, leading to local stress minima in case of enstatite and local maxima in case of pyrope.

Nucleation In contrast to the nucleation algorithm applied in the homogeneous systems above, the nucleation routine used for systems with a heterogeneous mineral composition is not random. Instead, spinel nuclei were inserted at local maxima in the stress distribution which are commonly situated along grain boundaries. Just as described in Sec. 3.4.1, nucleation occurs once at the begin of the transformation and from then on the number of grains is considered to be constant.

Due to relatively low resolutions of the simulations and resulting small numbers of stress maxima, the number of potential nucleation sites remains below the theoretically predicted number of spinel grains (cp. Sec. 3.4.1 and Sec. 2.3.2) and depends in addition on the random distribution of mineral phases. Usually the program inserted about 100 nuclei automatically into the host material, after the critical pressure was reached.

Spring network All computer experiments were calculated on the basis of an elastic spring network. In case of a combined olivine-pyrop-enstatite assemblage, which is the

closest approximation of real mantle material which was applied in the simulations, the purely elastic calculations are supplemented with calculations on the basis of a visco-elastic spring network.

We set the relevant parameters for the visco-elastic network as in previous chapters, using a timestep of $10^{11}s$ combined with a finite deformation of 0.002. The Newtonian viscosity η is set to $10^{22}\ Pa \cdot s$. Since it is consense to consider olivine as the weakest mineral phase in the mantle assemblages, the simulations are further simplyfied by considering the viscosity of enstatite and pyrope infinitely large, thus forming hard bodies in a plastic spinel matrix.

7.2 Spinel microstructures resulting from the simulations

7.2.1 Homogeneous parent phase

The olivine/spinel textures, which were obtained from simulations using a homogenous olivine host material, are compiled as a timeline in Fig. 7.1 below. Displayed is the growth of spinel in a system under uniaxial compression, biaxial compression and biaxial compression in combination with simple shear as described above. Each simulation inserts 160 nuclei into the host material after the critical pressure is reached.

The development of the olivine/spinel textures and the individual spinel grain is very much as predicted in Chap. 5.

Under uniaxial compression and the resulting strongly orientated stress field, grain growth is generally elongated towards the compressive direction, while single grains show the intergrowth features discussed in Sec. 5.4, primarily the merge of neighbouring grains and the subsequent continuation of the grain boundary migration as a single spinel grain (Fig. 7.1 (a)).

Hydrostatic stress conditions (Fig. 7.1 (b)) lead to the formation of isometric grains which merge and form clusters of spinel according to their spatial distribution.

The grain shapes and grain relations forming in the presence of combined biaxial compression and simple shear (Fig. 7.1 (c)), show a combination of the features of the experiments above. Grain shapes are almost isometric, caused by the biaxial component of the compression, but display a minor tendency of preferred growth towards the principle direction of the shear related particle movements. Under the conditions of the simulation, where right lateral simple shear was applied, this means a tendency to

form grain clusters on the diagonal from the top left towards the bottom right corner.

7.2.2 Heterogeneous parent phase

Olivine-pyrope assemblage

If only pyrope is present in the olivine matrix (Fig. 7.2) nucleation of spinel grains occurs primarily along the the olivine/pyrope interface. Only a minor amount of spinel nuclei form along olivine/olivine grain boundaries. The reason is the relatively large Youngs modulus of pyrope, compared to olivine, and the resulting local maxima in the stress distribution.

Growth of the spinel phase occurs along the connecting line between grains of pyrope, following the stress bridges which develop in the olivine matrix between the harder pyrope grains.

Olivine-enstatite assemblage

Although olivine is the harder material in case of the enstatite-olivine assemblage, nucleation along olivine/olivine interfaces is in balance with nucleation at olivine/enstatite interfaces (Fig. 7.3), caused by the numerically equivalent number of local maxima in the stress field within the olivine phase.

The subsequent growth of the spinel phase occurs primarily along the connection between enstatite grains and forms quickly throughgoing networks under inclusion of enstatite grains. This growth behaviour is similar to the preferred growth orientations observed in the olivine-pyrope assemblage.

Olivine-pyrope-enstatite assemblage

The simulation of nucleation and growth in a olivine-pyrope-enstatite assemblage must be considered to be the most realistic case, regarding the mineral content of upper mantle rocks. The development of spinel nucleation and growth in this assemblage is depicted in Fig. 7.4 using an elastic spring network and in Fig. 7.5 for a visco-elastic spring network. The resulting spinel structures under elastic and visco-elastic conditions are surprisingly similar in a poly-mineralic environment.

Nucleation of spinel occurs in abundance along olivine/olivine and olivine/pyrope inerfaces but is rare along olivine/enstatite boundaries. Growth and network forma-

tion after the nucleation appears to occur preferrentially on the connections between enstatite and pyrope and forms quickly networks according to their spatial distribution.

7.3 Driving force and consequences of the formation of spinel networks

The driving force for the strong localization of spinel growth in the simulations above is the increase of differential stress between pyrope grains and enstatite grains (Fig. 7.6). Although pyrope has a larger Youngs modulus than olivine, while the Youngs modulus of enstatite is smaller, the effect is essentially the same. In both cases the normal stress on the grain surface of spinel grains is increased and leads to an enhanced reaction velocity.

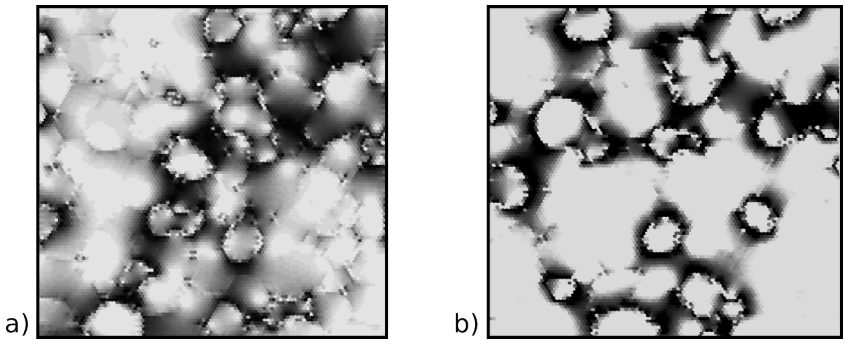

Figure 7.6: Differential stress field, forming in between the grains of (a) pyroxene (enstatite). (b) garnet (pyrope).

Comparing the microstructures formed by spinel in a monomineralic olivine host under hydrostatic pressure in Fig. 7.1 with the spinel structures that form in polymineralic host materials (Fig. 7.2 to Fig. 7.5), it is obvious that spinel in a polymineralic assemblage has a far larger tendency to form clusters. In addition the percolation of the total system by the formation of throughgoing spinel networks is significantly accelerated by the presence of pyrope and enstatite in the mineral assemblage, regardless if we consider a visco-elastic or an elastic spring network.

Further, the type of the applied stress plays an important role in the evolution of spinel microstructures. Considering the monomineralic system under uniaxial compression in Fig. 7.1 (b) we encounter a pronounced tendency to percolate the system,

due to the intense elongation of spinel grains. The conclusion, that similar effects occur in polymineralic host materials appears obvious.

We can thus conclude from the simulations in this chapter, that the choice of an appropriate host material is a critical factor in numerical and experimental investigations of the olvine→spinel transition and the probably related brittle failure of the material. Even if we consider the large difference in the scale of the grain size, that was assumed in the here-undertaken computer experiments, and the size of microcracks which were encountered in high pressure experiments of the olivine→spinel transition by e. g. Green et al. (1989, [40]) or Riggs and Green (2001, [88]), we can assume a large influence of the mineral assemblage on the localization of transition-related brittle failure.

Moreover, the grain size in the computer simulations must be regarded as an upper limit for a realistic grain size in mantle rocks (Karato, 1984, [51]). Especially in case of subducting material a much finer grained assemblage might be considered to be more realistic, thus extending the effect of a polymineralic composition to smaller scales.

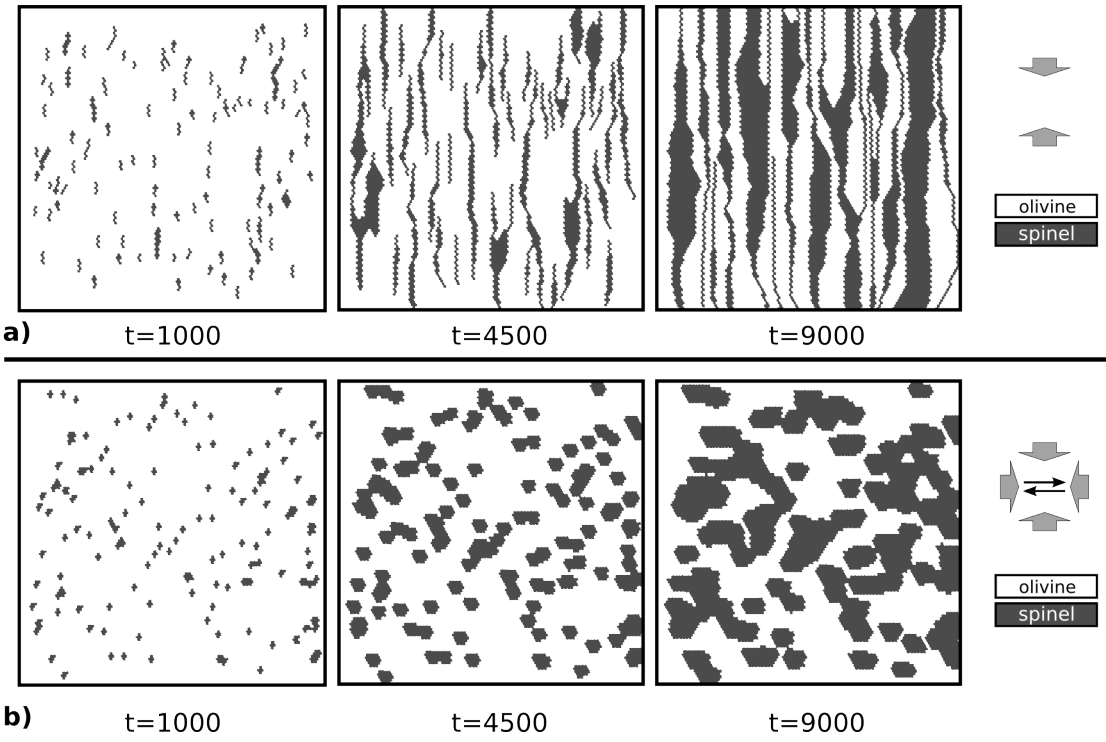

Figure 7.1: Time lapse of the evolution of olivine/spinel microstructures, resulting from a random distribution of 160 spinel seeds in homogeneous monomineralic olivine. Development of textures under (a) uniaxial compression, (b) biaxial compression and (c) right lateral simple shear, combined with biaxial compression in order to reach the critical stress. All simulations were performed on an elastic spring network.

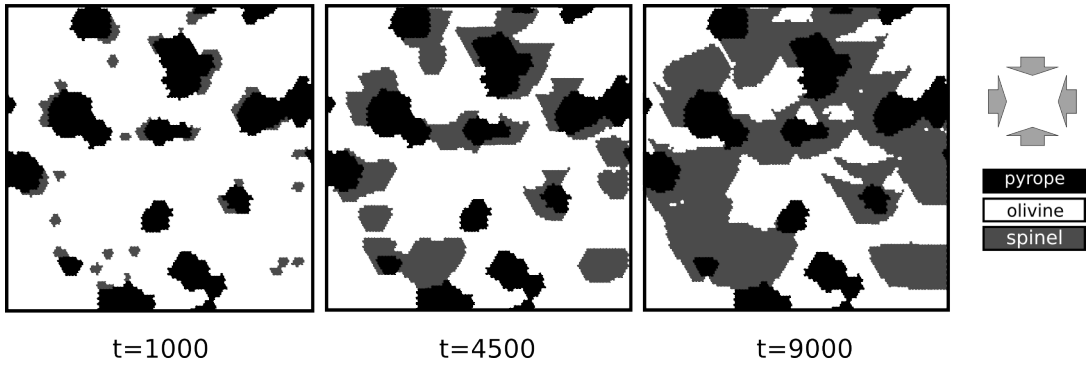

Figure 7.2: Time lapse of nucleation and growth of spinel in a olivine-garnet assemblage under hydrostatic stress on an elastic spring network. Spinel nuclei (seeds) were introduced at local stress maxima.

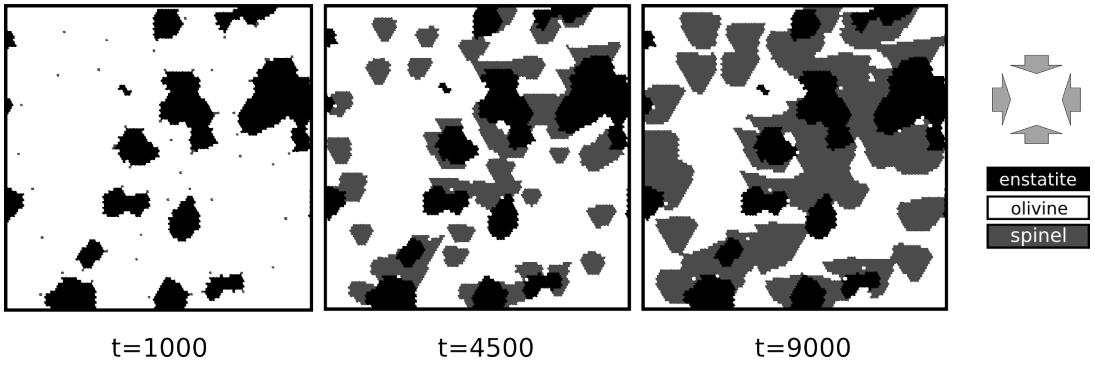

Figure 7.3: Time lapse of the microstructural evolution of spinel grains in a olivine-enstatite assemblage under hydrostatic stress on an elastic spring network. Spinel nuclei (seeds) were introduced at local stress maxima.

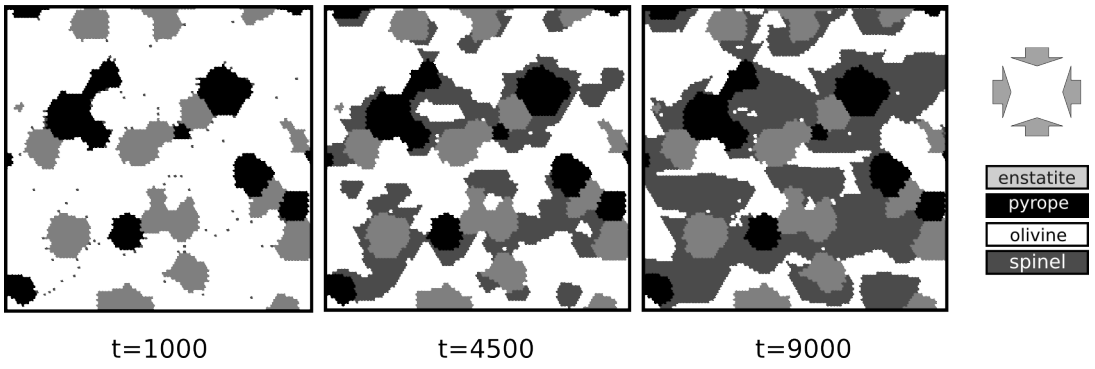

Figure 7.4: Time-lapse of nucleation and growth of spinel in a assemblage consisiting of olivine, enstatite and pyrope under hydrostatic stress on an elastic spring network. Spinel nuclei (seeds) were introduced at local stress maxima.

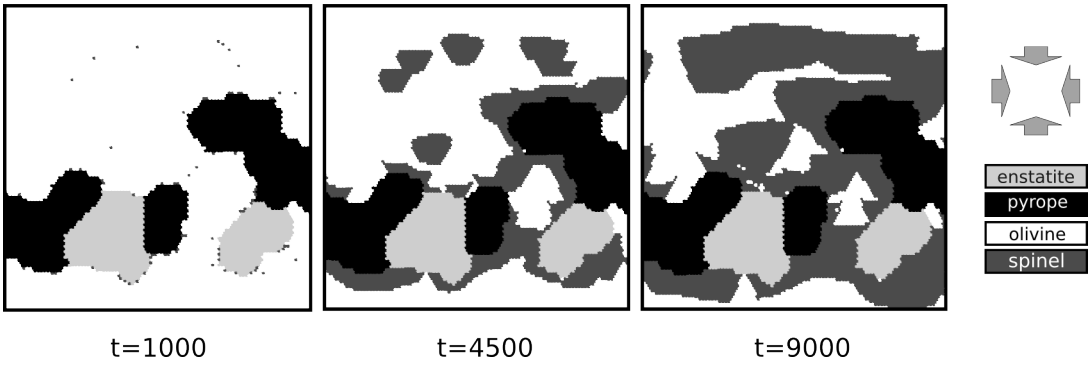

Figure 7.5: Time-lapse nucleation and growth of spinel in a assemblage consisiting of olivine, enstatite and pyrope under hydrostatic stress using a visco-elastic spring network. Spinel nuclei (seeds) were introduced at local stress maxima.

8 Summary and concluding remarks

This chapter aims to summarize and conclude the previous chapters. Further, suggestions to enhance the numerical model are made.

8.1 General conclusions

In order to gain a better understanding of the microstructures induced by the olivine→spinel transition in the mantle, it is necessary to deal with the non-availability of natural specimen of appropriate mantle rocks. Every investigation of the matter is therefore dependent on theoretical analysis and physical and numerical modeling. This thesis focused on the development and deployment of a computer model in order to simulate nucleation and growth of spinel in olivine.

8.1.1 Accuracy of the computer model

The computer code is able to reproduce growth features, which are known to appear in high pressure experiments with either silicatic olivine (Mg_2SiO_4) or a germanate equivalent (Mg_2GeO_4). This can be shown by principle growth features, notably the elongation of spinel grains towards the highest principal normal stress in the system. In addition the fractal dimension of structures modeled with the computer program is in the range of fractal dimensions known from high pressure experiments.

The similarity between simulated and experimental structures suggests, that the assumptions in the computer program are realistic and that the prediction of spinel grain shapes with the program is possible.

Yet the values for some important parameters are still inaccurate which may have considerable effects on the evolving spinel structures. Most notable is the error associated with the activation energy of the reaction, which has an exponential influence on the velocity of the grain boundary migration.

8.1.2 Anticrack-type growth mechanism of spinel in olivine

Various authors proposed an anticrack-type mechanism to explain a runaway process of spinel growth in olivine, which is supposed to lead to the brittle failure necessary to explain deep focus earthquakes.

It was possible to demonstrate in a series of simulations that the stress concentrations, which are necessary for an anticrack-type growth mechanism, are not consistent with the stress field that forms as a consequence of the olivine→spinel transition. Also the displacements in the host phase due to the phase transition do not comply with the displacements that would accompany an anticrack-like growth mechanism.

Computer experiments performed with monomineralic olivine with a gaussian quenched noise on the elastic parameters of the material displayed rough surface structures, which can occasionally resemble microstructures in the shape of anticracks. Local impurities of the host material can therefore be a working explanation when these structures are observed in high pressure experiments.

The particle displacements induced by an olivine→spinel transition in the often used germanate analogue of Mg_2SiO_4 proved to be partly different from displacements in natural occuring silicatic olivine. This raises the question if microstructures resulting from high pressure experiments in germanate-olivine are always valid approximations of microstructures in real mantle material.

8.1.3 Typical grain shapes and control parameter

The major influence on the shape of spinel grains is the direction of the principal stress acting on the grain. Differential and shear stress lead to elongated grain shapes, while hydrostatic stress is responsible for isometric grain perimeters.

The presence of statistical heterogeneities in the elastic parameters of the host phase leads generally to fractal grain structures. The fractality of the spinel structure may either affect the interior porosity or the roughness of the surface.

The effects of a disordered olivine host are largely neutralized if the simulations apply a visco-elastic spring network, where heterogeneities in the stress distribution are widely homogenized.

The fractal mass dimension and surface dimension of rough spinel structures converge towards a stable limit with progressive growth of the structure.

8.1.4 Network formation and percolation of spinel in olivine

A field of study, that has been completely ignored in studies of the olivine→spinel transition are transitions in the presence of non-reactive minerals as pyrope or enstatite. Heterogeneities in the stress field caused by the presence of these additional minerals form preferred nucleation sites for spinel and cause a localization of spinel growth along the connecting lines of these minerals. As a consequence spinel grains coalesce and form throughgoing networks which percolate the host material much faster than in a monomineralic olivine host. Interestingly, this observation was identical regardless if the calculations were performed on a visco-elastic or an elastic spring network.

It can be expected that the formation of throughgoing spinel networks have an important impact on the mechanical properties of the previously olivine dominated material. This can be either by the formation of potential shear zones associated with lateral spinel zones or by the formation of real spinel frameworks.

This phenom deserves certainly some more attention than could be given in this work, since it might link the rock textures of mantle material directly to the potential effects of the olivine→spinel transition on the material properties.

8.2 Possible improvements for shortcomings of the model

One of the major shortcomings of the here-developed growth algorithm is the absence of fracturing related to the olivine→spinel transition, which was omitted due to the significant complication of the program flow.

A further important improvement of the model would be the ability to model the elastic anisotropy of minerals, which would allow to include the preferred orientation of mineral grains and possible preferred growth orientations of spinel into the modeling of grain growth. In addition the unwanted anisotropies given by the predefined orientations of the regular hexagonal spring network should be erased, in order to have a more accurate representation of the growth structures. Both goals can be achieved if the normal spring model is supplemented with angular springs, connecting the normal spring between next-neighbour nodes.

Further, the current nucleation mechanism, where spinel nuclei are simultaneously activated at the beginning of the transformation, could be replaced by a constant nucleation mechanism.

Appendix

A Simulation of viscoelasticity in the spring network

A.1 Basic model

Viscoelasticity was introduced to the model with regard to the rheology of rocks under mantle-like PT-conditions. Unlike purely elastic substances, viscoelastic materials show a time-dependent strain rate due to the viscous component of the material. We consider linear rheological bodies with hookean elastic and Newtonian viscous behavior. For the elastic part of such a material $\sigma = 2E\epsilon$ (e. g. Ranalli, 1995, [84]).

Several models for viscoelastic materials exist, most notably the Maxwell and the Kelvin model, depicted in Fig. A.1. These models combine a purely hookean with a purely Newtonian element, either in series or in parallel.

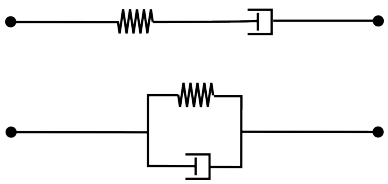

Figure A.1: Dashpot models. On top the Maxwell model, below the Kelvin model

While a phase transformation on the microstructural scale is by far to rapid to expect an impact of the viscous flow of the reaction during growth, the initial stress field at the time of nucleation within the overall material can be expected to be significantly altered by viscoelastic flow, due to the presence of hard/soft bodies and heterogeneity's in the system. Thus, by changing the starting conditions of the stress field before nucleation of the new phase, the dominant growth direction of newly formed high pressure phase as well as the preferred nucleation sites will be obviously influenced.

Progressive homogeneous deformation coupled with time-dependent viscous strain

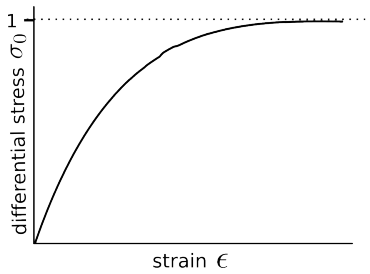

Figure A.2: Stress strain curve calculated by a homogeneous 2D particle-spring model under progressive pure shear strain. The strain is normalized to the maximum value. The shape of the curve equals analytically predicted solutions by converging against a threshold, where an equilibrium between the ongoing deformation of the body and the flow of the material is reached.

was first theoretically treated by Ramberg (1975, [83]) and later refined by e. g. Weijermars (1991, [105]). The basic confinements of these approaches are the restriction to (1) plane strain, (2) steady state conditions, resulting from a symmetrical steady state stress tensor and (3) cases without volume change. Due to the symmetrical stress tensor also the deformation is symmetric. Restrictions (1) and (3) are within the basic assumptions for a spatial discrete element of a 2D model as it is applied here. The confinement to steady state flow for discrete elements, due to a homogeneous deformation resulting in biaxial isochoric flow, is justified by the spatial and temporal discretization of the basic model, as long as the strain increment per timestep is not to large. Since viscous strain is proportional to the increasing elastic stress, we can expect to reach a yield stress, where the stress increase caused by a finite deformation step is in equilibrium with the stress decrease caused by the viscous flow of the material (Fig. A.2).

Various mathematical descriptions for the behavior of viscoelastic materials exist, most notably the Maxwell- and the Kelvin-model, both of them combining a spring and a dashpot, either in series (Maxwell) or in parallel (Kelvin).

In our simulations we effectively apply the Maxwell-model, by first doing a basic elastic relaxation, putting the particles in the positions of their elastic equilibrium, followed up by a viscous deformation of each single particle based on the elastic stress tensor and finally an additional elastic relaxation in order to achieve a spatial equilibrium distribution of the deformed particles again. The length of springs will be continuously adapted to the hull of the resulting elliptic shape.

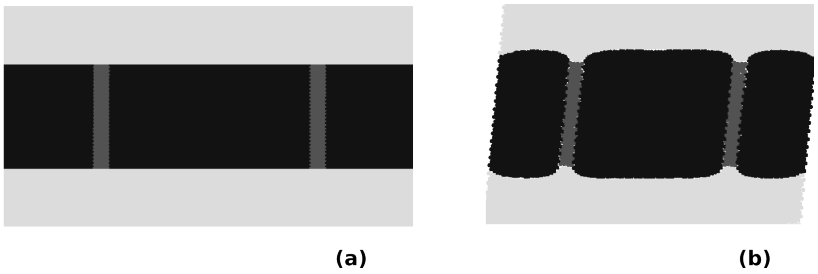

Figure A.3: Example of a viscoelastic deformation using the described scheme. Depicted is the output for a combination of pure and simple shear deformation. (a) in the undeformed state and (b) after deformation. The setting represents a low viscosity layer (black), interrupted by high viscosity vertical high viscosity zones in a medium viscosity host, similar to boudinage structures. Pure shear consists of vertical dilatation and horizontal compaction, simple shear is right lateral horizontal. 'Holes' in picture (b) are caused by the extreme deformation of single particles and resulting display problems.

A.2 Conjugate radii concept

Available formulas for the calculation of the progressive viscous deformation of materials, as given by the above mentioned Weijermars (1991) and Ramberg (1975) articles, allow the calculation of particle paths on the basis of a given stress tensor. Since the hull of a single particle in elastic equilibrium can be described by an ellipse (which, in the purely elastic or the undeformed viscous case, simplifies to a circle), a geometrical description of the ellipse in the terms of adequate markers on the hull seems to be desirable. The displacement of these markers under the current stress conditions can be computed, and a complete description of the ellipse could be instantly given. This, in turn, would allow the calculation of the new length of every spring within the particle as well as the calculation of repulsion forces between particles.

An adequate geometrical description, that fulfills these requirements, is the concept of conjugate radii as known from computer graphics (Tran-Thong, 1983, [100]). Two arbitrary radii of an ellipse are said to be conjugate, if each is parallel to the tangent to the ellipse at the other point, thus forming a rhomboid on the ellipse (Fig. A.2). The shape of an arbitrary, progressively deformed ellipse with a fixed center is defined at all times, if the two intersections of the elliptic hull with these radii are known, and if it can be guaranteed that these radii remain conjugate during the progressive plane viscous deformation.

The general equation to generate an ellipse based on the conjugate radii is

$$\begin{cases} x = b_x \cdot \cos(\phi) - a_x \cdot \sin(\phi) \\ y = b_y \cdot \cos(\phi) + a_y \cdot \sin(\phi) \end{cases} . \tag{A.1}$$

where ϕ ranges from 0 to 2π and $\vec{a} = \begin{pmatrix} a_x \\ a_y \end{pmatrix}$ and $\vec{b} = \begin{pmatrix} b_x \\ b_y \end{pmatrix}$ are the vectors for the conjugate radii with the midpoint of the ellipse as centers. Under general homogeneous deformation, which is given here, it is guaranteed that the rhomboid, formed by the conjugate radii and the tangents on the elliptic hull, preserves parallelism of its sides at all times and the tangents on the hull remain tangent.

Thus it suffices to calculate the particle path of the intersections between two arbitrary orthogonal radii of the initial circular particle for the local stress tensor for every timestep, to define the particle shape throughout the simulation. Starting points for this procedure are $\vec{a} = \begin{pmatrix} 1 \\ 0 \end{pmatrix}$ and $\vec{b} = \begin{pmatrix} 0 \\ 1 \end{pmatrix}$, the intersections with the coordinate axes.

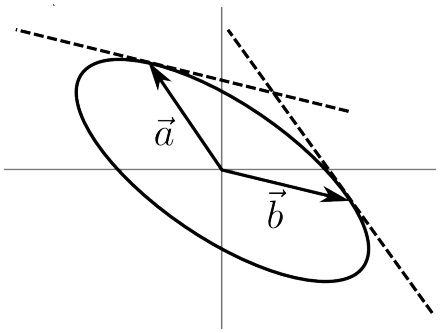

Figure A.4: Sketch of the conjugate radii concept. Per definition, conjugate radii parallel the tangent to the ellipse at the other point. $\vec{a}$ and $\vec{b}$ are vectors of the intersection of the radii and the hull, which will be iteratively displaced during the progressive deformation.

A.3 Particle path calculation

A progressive deformation is fully predictable and characterized by the principal stress orientation, provided that this orientation remains constant in relation to a reference frame (Ramberg, 1975, [83]). It is then possible to make inferences about the finite

deformation pattern, that will be accomplished after a particular time step. Since the stress tensor for each particle is considered to remain constant during a finite deformation step of the elastic lattice, it is thus possible to calculate the shape of the particle due to viscous flow iteratively. The reference frame is given by the center of every particle and the common coordinate system.

Particle pathes for $\vec{a}$ and $\vec{b}$ are calculated on the basis of the deviatoric stress tensor for each particle. The normal and the shear strain components of D_{ij} are related to the deviatoric stress tensor $\sigma_{ij}^{'}$ by

$$\dot{\epsilon_{xx}} = \frac{\sigma_{xx}^{'}}{2\eta} \tag{A.2}$$

$$\dot{\epsilon_{xy}} = \frac{\sigma_{xy}^{'}}{2\eta} \tag{A.3}$$

where η is the Newtonian viscosity.

The stress induces strain rates described by the strain rate tensor is

$$D_{ij} = \begin{bmatrix} \dot{\epsilon}_{11} & \dot{\epsilon}_{12} \\ \dot{\epsilon}_{21} & \dot{\epsilon}_{22} \end{bmatrix} = \begin{bmatrix} \sigma_{11}^{'} & \sigma_{12}^{'} \\ \sigma_{12}^{'} & -\sigma_{11}^{'} \end{bmatrix} \cdot \frac{1}{2\eta}. \tag{A.4}$$

Due to the symmetry of the deviatoric stress tensor, given by the spring network, $\dot{\epsilon}_{21} = \dot{\epsilon}_{12}$ and $\dot{\epsilon}_{22} = -\dot{\epsilon}_{11}$. Incompressibility is automatically accounted for by the equality of the absolute values of $\dot{\epsilon}_{11}$ and $\dot{\epsilon}_{22}$.

The solution of Eq. A.4 is obtained solving the set of equations given by (Ramberg, 1975, [83])

$$\begin{bmatrix} \dot{x} \\ \dot{y} \end{bmatrix} = D_{ij} \cdot \begin{bmatrix} x \\ y \end{bmatrix}, \tag{A.5}$$

which is generally given by

$$\begin{bmatrix} x \\ y \end{bmatrix} = \begin{bmatrix} c_{11} & c_{12} \\ c_{21} & c_{22} \end{bmatrix} \begin{bmatrix} \exp(\kappa_1 t) \\ \exp(\kappa_2 t) \end{bmatrix}, \tag{A.6}$$

where κ_1 and κ_2 are the eigenvalues, and

$$\kappa_1, \kappa_1 = \pm\frac{1}{2}\sqrt{2\dot{\epsilon}_{11} + 8\dot{\epsilon}_{12}} \tag{A.7}$$

for the particular case given here. The solution is then, again taking into account the equalities in Eq. A.4,

$$c_{11} = \frac{(\kappa_2 - \dot{\epsilon}_{11})x_0 - \dot{\epsilon}_{12}y_0}{\kappa_1 - \kappa_2}, \tag{A.8}$$

$$c_{12} = \frac{(\dot{\epsilon}_{11} - \kappa_1)x_0 + \dot{\epsilon}_{12}y_0}{\kappa_2 - \kappa_1}, \tag{A.9}$$

$$c_{21} = \frac{(\kappa_1 - \dot{\epsilon}_{11})(\kappa_2 - \dot{\epsilon}_{11})\dot{\epsilon}_{12}^{-1}x_0 - (\kappa_1 - \dot{\epsilon}_{11})y_0}{\kappa_1 - \kappa_2}, \tag{A.10}$$

$$c_{22} = \frac{(\kappa_1 - \dot{\epsilon}_{11})(\kappa_2 - \dot{\epsilon}_{11})\dot{\epsilon}_{12}^{-1}x_0 - (\kappa_2 - \dot{\epsilon}_{11})y_0}{\kappa_2 - \kappa_1}, \tag{A.11}$$

enabling a straight forward calculation of the new (x, y) position from an arbitrary (x_0, y_0).

A.4 Potential error sources

For a uniformly progressing externally applied deformation, an equilibrium threshold will be reached at some yield stress, where the stress-induced strain rate is identical to the external strain. At this point, the stress-strain curve will alternate around the the yield stress. The error is then ultimately defined by the step size of the applied deformation (Fig. A.2).

A more serious error source lies within the geometry of the normal force spring lattice itself, which is defined by the spring lengths. This model doesn't account for elastic forces associated to possible micro-rotations of springs. This circumstance is rather neglectable if the spring length is uniform for every spring attached to a particular node, since the area of a particle will not be modified by the actual orientation of the springs. The case is different for orientation-dependent spring lengths as given by the elliptical particle shape, which was applied here (Fig. A.5).

This problem can be potentially overcome by introducing angular springs, which connect adjacent normal springs and account therefore for elastic forces during rotation of springs (as described by e. g. Ostoja-Starzewski, 1996, [78]), though this scheme wasn't applied here. However, the impact of micro-rotations can be considered comparatively small in the in these particular simulations, since fracturing doesn't occur, which is

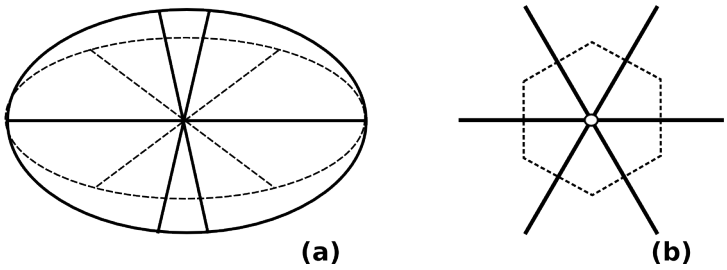

Figure A.5: (a) Possible area increase of a particle with springs of different lengths in case of micro-rotations. (b) Unit cell of a triangular lattice model with normal and angular springs, making area changes as in (a) mechanically reasonable.

usually the main reason for the loss of internal integrity and subsequent rotations off the mechanical elements within a lattice (Monette, 1994, [72]).

B Calculation of thermal conduction

B.1 Introduction

Inclusion of the latent heat release and subsequent conduction of the released heat energy into the program flow can be a key factor concerning localizations in the ongoing grain boundary migration. The temperature increase of a particle undergoing a phase transition can be calculated after Eq. 2.35. This chapter discusses the conduction of the released heat energy with time.

The basic formula for the subsequent heat-flow is the parabolic differential Fourier-equation, which can be solved by finite differencing. To solve the problem of heat conduction, several techniques could have been applied, in particular finite differencing and finite element approaches.

The implementation in the code applies a finite-difference technique, which is based on a rectangular lattice. The solution is obtained by an ADI (Alternating Direct Implicit) algorithm, which is described in detail below. Basically, this is implemented as an own class of the program, and relies thus on a (rather primitive) interface to communicate with the tridiagonal elastic lattice. Currently it can solve matrices for a

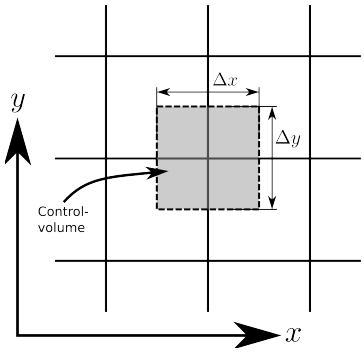

Figure B.1: Control volume on a section of the 2-dimensional finite difference lattice.

single heat-capacity and heat-conductivity, thus neglecting heterogeneities in the material. The large advantage of using unified parameters is the considerably accelerated computation time, since the involved matrices have to be solved only once instead of having to be solved for every single vector within the matrix.

A general difficulty in the finite difference-approach is the deformation of the underlying lattice. In many well-known finite-difference methods the solution is based on a fixed spacing in x- and y-direction and the system of equations can not be solved for varying parameters. One of the strengths of the ADI-method, beside its stability for every Δt, Δx, Δy, is the solvability in spite of changing positions of lattice-boundaries.

B.2 Implementation

During an ADI-run, every time-step is split into two equal parts. In the first part – which means integrating from $k\Delta t$ to $(k+1/2)\Delta t$ - x is taken to be implicit while y is treated explicitly. In a second step - from $(k+1/2)\Delta t$ to $(k+1)\Delta t$ - the method is made explicit in x and implicit in y.[1] The terms 'explicit' and 'implicit' in the numerical context refer to different schemes of the finite differencing (see e.g. Press et al., 1992, [81]).

Beside the advantage of being solvable for *different* spacings in x and y (which isn't advisable for purely explicit or implicit schemes), this method only involves solving a number of equations that are essentially tridiagonal and therefore computationally inexpensive. The method is known to be stable for all Δx, Δy and Δt.

Diffusion in the 2-dimensional case is generally governed by a parabolic partial differential equation of the form:

$$\frac{\partial u}{\partial t} = \frac{\partial}{\partial x}\left(D\frac{\partial u}{\partial x}\right) + \frac{\partial}{\partial y}\left(D\frac{\partial u}{\partial y}\right) \tag{B.1}$$

[1] In matrix form, Douglas and Peaceman (1955, [23]) proposed:

$$(I + B_1)\tilde{u}^{n+1/2} = (I - B_2)u^n + \frac{k}{2}f^{n+1/2}(\mathrm{x-sweep})$$

$$(I + B_2)u^{n+1} = (I - B_1)\tilde{u}^{n+1} + \frac{k}{2}f^{n+1/2}(\mathrm{y-sweep}),$$

where f is a source term and will be ignored. This algorithm can be economized into a form, in which B_1 does not appear explicitly (Wachspresse and Habetler, 1960, [103]).

Application to thermal conduction yields the classical Fourier-equation:[19]

$$\rho c \frac{\partial T}{\partial t} = \frac{\partial}{\partial x}\left(k \frac{\partial T}{\partial x}\right) + \frac{\partial}{\partial y}\left(k \frac{\partial T}{\partial y}\right) + \dot{f} \tag{B.2}$$

where ρ is the density, c the specific heat and k the heat diffusivity. $\dot{f}$ is the remainder of the Taylor expansion and represents a source term, which can be ignored if no constant heat-sources exists, leading to a Laplace-term (Hering et al., 1992, [43]). Implicit finite differencing (i.e. approximating infinite terms by finite differences, compare e.g. Press et al., 1992, [81]) of equation B.2 with $f = 0$ now yields:

$$\rho c \frac{T_{j,l}^{n+1} - T_{j,l}^{n}}{\Delta t} = k \left(\frac{T_{j+1,l}^{n+1} - 2T_{j,l}^{n+1} + T_{j-1,l}^{n+1}}{(\Delta x)^2} + \frac{T_{j,l+1}^{n+1} - 2T_{j,l}^{n+1} + T_{j,l-1}^{n+1}}{(\Delta y)^2} \right) \tag{B.3}$$

In equation B.3, n is the time-step, while j and l represent the spatial mesh. Transformed to the ADI-method, this gives:

$$T_{j,l}^{n+1/2} = \alpha \left(\delta_x^2 T_{j,l}^{n+1/2}\right) + \beta \left(\delta_y^2 T_{j,l}^{n}\right) + T_{j,l}^{n} \tag{B.4}$$

$$T_{j,l}^{n+1} = \alpha \left(\delta_x^2 T_{j,l}^{n+1/2}\right) + \beta \left(\delta_y^2 T_{j,l}^{n+1}\right) + T_{j,l}^{n+1/2} \tag{B.5}$$

.

This idea expands to matrix-equations of the following type[2]:

[2]this includes the following definitions:

$$\alpha = \frac{k\Delta t}{2\rho c(\Delta x)^2}; \beta = \frac{k\Delta t}{2\rho c(\Delta x y)}$$

$$x = k\Delta x; y = l\Delta y; k, l = 1, 2, 3...$$

$$\delta_x^2 T_{j,l}^{n} = T_{j+1,l}^{n+1} - 2T_{j,l}^{n+1} + T_{j-1,l}^{n+1}$$

$$\delta_y^2 T_{j,l}^{n} = T_{j,l+1}^{n+1} - 2T_{j,l}^{n+1} + T_{j,l-1}^{n+1}$$

$$\begin{bmatrix} 1 & 0 & 0 & ... & ... & 0 \\ -\alpha & 1+2\alpha & -\alpha & 0 & ... & ... \\ 0 & ... & ... & ... & ... & 0 \\ ... & ... & 0 & -\alpha & 1+2\alpha & -\alpha \\ 0 & ... & ... & 0 & 0 & 1 \end{bmatrix} \begin{pmatrix} T_{1,l}^{n+1/2} \\ T_{2,l}^{n+1/2} \\ ... \\ ... \\ T_{N,l}^{n+1/2} \end{pmatrix} =$$

$$\begin{bmatrix} 1 & 0 & 0 & ... & ... & 0 \\ -\beta & 1+2\beta & -\beta & 0 & ... & ... \\ 0 & ... & ... & ... & ... & 0 \\ ... & ... & 0 & -\beta & 1+2\beta & -\beta \\ 0 & ... & ... & 0 & 0 & 1 \end{bmatrix} \begin{pmatrix} T_{j,1}^{n} \\ T_{j,2}^{n} \\ ... \\ ... \\ T_{j,N}^{n} \end{pmatrix} \tag{B.6}$$

and

$$\begin{bmatrix} 1 & 0 & 0 & ... & ... & 0 \\ -\beta & 1+2\beta & -\beta & 0 & ... & ... \\ 0 & ... & ... & ... & ... & 0 \\ ... & ... & 0 & -\beta & 1+2\beta & -\beta \\ 0 & ... & ... & 0 & 0 & 1 \end{bmatrix} \begin{pmatrix} T_{j,1}^{n+1} \\ T_{j,2}^{n+1} \\ ... \\ ... \\ T_{j,N}^{n+1} \end{pmatrix} =$$

$$\begin{bmatrix} 1 & 0 & 0 & ... & ... & 0 \\ -\alpha & 1+2\alpha & -\alpha & 0 & ... & ... \\ 0 & ... & ... & ... & ... & 0 \\ ... & ... & 0 & -\alpha & 1+2\alpha & -\alpha \\ 0 & ... & ... & 0 & 0 & 1 \end{bmatrix} \begin{pmatrix} T_{1,l}^{n+1/2} \\ T_{2,l}^{n+1/2} \\ ... \\ ... \\ T_{N,l}^{n+1/2} \end{pmatrix} \tag{B.7}$$

which are essentially tridiagonal and can be solved in a trivial manner by means of the Gauss-algorithm (compare e.g. Gershenfeld, 1999, Press et al., 1992, [81]), or by an algorithm optimized for matrices of that form. One can also solve it for the total system as a whole instead for vectors (as has been implemented in the *latte*-code), which is probably the easiest and – more important – fastest method, by simply uniting the Temperature-vectors to a matrix.

The boundary condition can be set for instance according to a Dirichlet condition,

which governs the temperature of boundary nodes as a function of time. In case of the algorithm as implemented in *latte*, T as a boundary condition is currently kept constant at a reasonable temperature (for instance 1000°K).

B.3 Accuracy increase and optimization of the computation time

The accuracy can be considerably increased, if the parameters α and β from Eq. B.6 and B.7 are diminished, preferably below an (empirically determined) value of 1. Since α, β are defined as ratio of the timestep and some function of the spacing widths Δx and Δy, an internal scaling down of the timestep and looping until the diminished timesteps add up to the original one is sufficient. On the downside, this scheme may lead to a considerable increase of computation time.

Computation time can be saved, on the other hand, if a thermal relaxation is omitted for timesteps larger than the thermal relaxation time. After the thermal relaxation time, the heat energy will be evenly distributed in the system. Using fixed boundary conditions this means that the system will be reset to the boundary temperature. This way, remarkable savings of computation time can be achieved in case of slow reactions, in particular considering the above mentioned scaling down of timestep. The thermal relaxation time τ is given by

$$\tau = \frac{d^2 \rho c}{\lambda}, \tag{B.8}$$

where d is the half-diameter of the total system and λ the thermal conductivity (Gerthsen, 1989, [35]).

C Parameters used in the computer simulations

C.1 Thermodynamic parameters of the α/β-olivine transition

C.1.1 Constants

Entropy difference $\alpha \rightarrow \beta$ olivine Δs	Akaogi et al., 1989, [2]	$-7.7\ J/(mol \cdot K)$
Volume difference $\alpha \rightarrow \beta$ olivine Δv	Akaogi et al., 1989, [2]	$-3.16 \cdot 10^{-6}\ m^3/mol$
Interphase free energy $\alpha \rightarrow \beta$ olivine γ	Cooper and Kohlstedt, 1982, [20]	$0.6\ J/m^2$
Specific heat of olivine c_{ol}	Akaogi et al., 1989, [2]	$1.05 \cdot 10^3\ J/(kg \cdot K)$
Thermal diffusivity κ_{ol}	Däßler et al., 1996, [21]	$1.0 \cdot 10^{-6}\ m^2/s$
Preexponential factor I_0	Sung and Burns, 1976, [97]	$1.0 \cdot 10^{40}\ 1/(m^3 \cdot s \cdot K)$
Preexponential factor Y_0	Karato et al., 2001, [54]	$1.58 \cdot 10^{12}\ m/(s \cdot K)$
Intercept of Clapeyron equation, P_0	Akaogi et al., 1989, [2]	$10.8 \cdot 10^9\ GPa$
Slope of Clapeyron equation	Akaogi et al., 1989, [2]	$2436708.86\ Pa/K$

Table C.1: Values of parameters used in the calculation of rates of the α-/β-olivine transition.

α_m	Rubie and Ross, 1994, [91]	$159\ J/(mol \cdot K)$
Activation volume V_0^*	Rubie and Ross, 1994, [91]	$1.19 \cdot 10^4\ J/(mol \cdot GPa)$
K_c	Rubie and Ross, 1994, [91]	8
$K_c^{'}$	Rubie and Ross, 1994, [91]	1

Table C.2: Values of parameters used for the calculation of the activation energy ΔH_a (Eq. 2.9 - Eq. 2.11).

C.1.2 Molar volume

The molar volume of α-olivine and β-olivine can be calculated using the parameters given in Table C.3 with (Akaogi et al., 1989, [2])

$$V = V_{298} \exp\left(\int_{298}^{T} \alpha\,(T)\,dT\right) \tag{C.1}$$

where the thermal expansion coefficient α is given by

$$\alpha(T) = a + b \cdot T + c \cdot T^{-2}. \tag{C.2}$$

Phase	cm^3/mol	$a \cdot 10^5$	$b \cdot 10^9$	$c \cdot 10$
α-Mg_2SiO_4	43.67	3.052	8.504	-5.824
β-Mg_2SiO_4	40.51	2.711	6.885	-5.767

Table C.3: Parameters for the calculation of the molar volume of α-olivine and β-olivine, after Akaogi et al., 1989, [2], using Eq. C.1 and C.2.

C.1.3 Heat capacity

In a similar manner the heat capacity C of either α-olivine and β-olivne is given by (Akaogi et al., 1989, [2])

$$C = A + B \cdot T^{-0.5} + C \cdot T^{-2} + D \cdot T^{-3}, \tag{C.3}$$

parameters are listed in Table C.4.

Phase	$A \cdot 10^{-2}$	$B \cdot 10^{-3}$	$C \cdot 10^{-6}$	$D \cdot 10^{-8}$
α-Mg_2SiO_4	2.178	-1.408	0.0	-5.264
β-Mg_2SiO_4	2.164	-1.472	0.0	1.663

Table C.4: Parameters for the calculation of the heat capacity of α-olivine and β-olivine, after Akaogi et al., 1989, [2], using Eq. C.3.

C.2 Elastic parameters of minerals

C.2.1 Silicate olivine ($\alpha - (Mg_{0.9}Fe_{0.1})_2\, SiO_4$)

Isotropic isothermal bulk modulus K_{ol}	Zha et al., 1998, [107]	130 GPa
Isotropic isothermal shear modulus G_{ol}	Liebermann, 2000, [66]	78 GPa

Table C.5: Elastic parameters of silicate olivine $[\alpha - (Mg_{0.9}, Fe_{0.1})_2 SiO_4]$ as applied in the computer simulations. Molar parameters are denoted with lowercase letters.

C.2.2 Silicate spinel ($\beta - (Mg_{0.9}Fe_{0.1})_2\, SiO_4$)

Isotropic bulk modulus K_{spin}	Bina et al., 2001, [12]	170 GPa
Isotropic shear modulus G_{spin}	Kiefer et al., 2001, [57]	116 GPa

Table C.6: Elastic parameters of spinel/wadsleyite $[\beta - (Mg_{0.9}, Fe_{0.1})_2 SiO_4]$ as applied in the computer simulations. Molar parameters are denoted with lowercase letters.

C.2.3 Magnesium germanate olivine ($\alpha - Mg_2GeO_4$)

Molar volume v_{ge-ol}	Navrotsky, 1973, [74]	$4.58 \cdot 10^{-5}\ m^3/mol$
Isotropic bulk modulus K_{ge-ol}	Weidner and Hamaya, 1983, [104]	117.7 GPa

Table C.7: Elastic parameters of magnesium germanate olivine $[\alpha - Mg_2GeO_4]$.

C.2.4 Magnesium germanate spinel ($\beta - Mg_2GeO_4$)

Molar volume $v_{ge-spin}$	Navrotsky, 1973, [74]	$4.23 \cdot 10^{-5}\ m^3/mol$
Isotropic bulk modulus $K_{ge-spin}$	Weidner and Hamaya, 1983, [104]	179.0 GPa

Table C.8: Elastic parameters of magnesium germanate spinel $[\beta - Mg_2GeO_4]$.

C.2.5 Pyroxene (enstatite, $MgSiO_3$)

Isotropic bulk modulus K_{opx}	Frisillo and Barsch, 1972, [31]	104.79 GPa
Molar volume v_{opx}	Angel, 1994, [6]	$3.1292 \cdot 10^{-5}$ m^3/mol
Thermal expansion coefficient α_V	Hugh-Jones, 1997, [44]	$32.2 \cdot 10^{-4}$ K^{-1}

Table C.9: Elastic and thermal parameters of pyroxene (orthopyroxene with $En_{80}Fs_{20}$).

C.2.6 Garnet (Pyrope, $Mg_3Al_2Si_3O_{12}$)

Molar volume v_{py}	Geiger, 1997, [34]	$1.13163 \cdot 10^{-4}$
Thermal expansion coefficient α_V	Pal et al., 1999, [79]	$0.236 \cdot 10^{-4}$ K^{-1}
Isotropic bulk modulus K_{py}	Chen et al., 1997, [17]	171 GPa

Table C.10: Elastic and thermal parameters of garnet (pyrope).

C.3 Creep parameters of mantle minerals

C.3.1 Silicate olivine (forsterite, $\alpha - (Mg_{0.91}Fe_{0.09})_2\, SiO_2$)

preexponential factor A
stress exponent n
activation energy E

Table C.11: Parameters from Bai et al. (1991, [9]).

C.3.2 Orthopyroxene (enstatite, $MgSiO_3$)

The equations given for the creep in enstatite differ from those of the other minerals, since Mackwell (1991, [68]) takes generally two types of creep separately into account. These two types are not further defined. The total strain rate caused by creep is then calculated from:

$$\dot{\epsilon} = \left(\frac{1}{\epsilon_1} + \frac{1}{\epsilon_2}\right)^{-1}. \tag{C.4}$$

preexponential factor A	$5.2 \cdot 10^5\ MPa^{-1}s^{-1}$
stress exponent n	3.5
activation energy E	$540\ kJ/mol$

Table C.12: Parameters for ϵ_1 in Eq. C.4 in enstatite, given in Mackwell (1991, [68]). The constituent power law equation is $\dot{\epsilon_1} = A \cdot \left(\sigma^{'}\right)^n \cdot \exp\left(\frac{E}{RT}\right)$. The deviatoric stress $\sigma^{'}$ is given in MPa.

preexponential factor A	$1 \cdot 10^{14}\ MPa^{-1}s^{-1}$
stress exponent n	3.5
activation energy E	$540\ kJ/mol$

Table C.13: Parameters for ϵ_2 in Eq. C.4 in enstatite, given in Mackwell (1991, [68]). The constituent power law equation is $\dot{\epsilon_2} = A \cdot \left(\sigma^{'}\right)^n \cdot \exp\left(\frac{E}{RT}\right)$. The deviatoric stress $\sigma^{'}$ is given in MPa.

C.3.3 Garnet (pyrope, $Mg_3Al_2Si_3O_{12}$)

preexponential factor A	$3.5 \cdot 10^6 \begin{pmatrix} +4.8 \\ -2.0 \end{pmatrix} \cdot 10^6\ GPa^{-1}s^{-1}$
stress exponent n	3.2 ($\pm$0.7)
activation energy E	270 ($\pm$40) kJ/mol

Table C.14: Parameters for pyrope creep. The constituent power law equation is $\dot{\epsilon} = A \cdot \left(\sigma^{'}\right)^n \cdot \exp\left(\frac{E}{RT}\right)$. Data from Li et al. (2006, [65]). The deviatoric stress $\sigma^{'}$ is given in GPa.

C.4 Composition of mantle material

Pyrope, $Mg_3Al_2Si_3O_{12}$	15%
Clinopyroxene	15%
Opx	10%
Olivine	60%

Table C.15: Mineralogical composition of pyrolitic material at a depth of approximately 350 km. Data after Ita and Stixrude (1992, [47]).

Bibliography

[1] M. Akaogi and S. Akimoto. High-pressure phase equilibria in a garnet lherzolite, with special reference to $Mg^{2}+-Fe^{2}+$ partitioning among constituent minerals. *Physics of the Earth and Planetary Interiors*, 19:31–51, 1978.

[2] M. Akaogi, E. Ito, and A. Navrotsky. Olivine-modified spinel-spinel transitions in the system Mg_2SiO_4 - Fe_2SiO_4: Calorimetric measurements, thermochemical calculation, and geophysical application. *Journal of Geophysical Research*, 94(B11):15671–15685, 1989.

[3] S. Akimoto and H. Fujisawa. Olivine-spinel solid solution equilibria in the system $Mg_2SiO_4 - Fe_2SiO_4$. *Journal of Geophysical Research*, 73:1467–1479, 1968.

[4] Allen. *Relaxation methods*. McGraw-Hill Book Company, 1954.

[5] O. L. Anderson and J. D. Bass. Transition region of the earth's upper mantle. *Nature*, 320:321–328, 1986.

[6] R. J. Angel and D. A. Hugh-Jones. Equations of state and thermodynamic properties of enstatite pyroxenes. *Journal of Geophysical Research*, 99:19777–19783, 1994.

[7] M. Avrami. Kinetics of Phase Change. II: Transformation-Time Relations for Random Distribution of Nuclei. *J Chem Phys*, 8:212–224, 1949.

[8] J. D. Axe and Y. Yamada. Scaling relations for grain autocorrelation functions during nucleation and growth. *Physical Review B*, 34(3):1599–1606, 1986.

[9] Q. Bai, S. Mackwell, and D. Kohlstedt. High Temperature Creep of Olivine Single Crystals. 1. Mechanical Results for Buffered Samples. *Journal of Geophysical Research*, 96:2441–2463, 1991.

[10] J. D. Bernal. Discussion. *Observatory*, 59:268, 1936.

[11] M. I. Billen and G. Hirth. Newtonian versus non-Newtonian upper mantle viscosity: Implications for subduction initiation. *Geophysical Research Letters*, 32, 2005.

[12] C. R. Bina, S. Stein, F. C. Marton, and E. Van Ark. Implications of slab mineralogy for subduction dynamics. *Physics of the Earth and Planetary Interiors*, 127:51–66, 2001.

[13] C. R. Bina and B. J. Wood. Olivine-Spinel Transitions: Experimental and Thermodynamic Constraints and Implications for the Nature of the 400-km Seismic Discontinuity. *Journal of Geophysical Research*, 92(B6):4853–4866, 1987.

[14] A. Brearley and D. Rubie. Transformation mechanisms of San Carlos olivine to $(MgFe)_2SiO_4$ β-phase under subduction zone conditions. *Physics of the Earth and Planetary Interiors*, 86:45–67, 1994.

[15] A. Bunde and S. Havlin. *Fractals and Disordered Systems.* Springer, Berlin, 1996.

[16] P. C. Burnley and H. W. Green. Stress dependence of the mechanism of the olivine→spinel transition. *Nature*, 338:753–756, 1989.

[17] G. J. A. Chen, G. D. Cook, D. Gwanmesia, and R. C. Liebermann. Elastic wave velocities of $Mg_3Al_2Si_3O_12$-pyrope garnet to 10 GPa. *American Mineralogist*, 84:384–388, 1999.

[18] J. Christian. *The Theory of Transformations in Metals and Alloys*, volume 15 of *International Series on Materials Science and Technology.* Pergamon Press, Oxford, 1981.

[19] H. Cívzková, J. van Hunen, and A. van den Berg. Stress distribution within subducting slabs and their deformation in the transition zone. *Physics of the Earth and Planetary Interiors*, 161:202–214, 2007.

[20] R. F. Cooper and D. L. Kohlstedt. *High pressure research in geophysics*, chapter Interfacial energies in the olivine-basalt system, pages 217–228. Reidel, Dordrecht, 1982.

[21] R. Däßler, D. Yuen, S. Karato, and M. Riedl. Two-dimensional thermo-kinetic model for the olivine-spinel phase transition in subducting slabs. *Physics of the Earth and Planetary Interiors*, 94(94):217–239, 1996.

[22] A. Davies. *The Finite Element Method: A First Approach.* Clarendon Press, Oxford, 1980.

[23] . J. Douglas, Jr. and D. Peaceman. Numerical solution of two-dimensional heat flow problems. *American Institute of Chemical Enngineering Journal*, 1:505–512, 1955.

[24] E. Dowty. Crystal Growth and Nucleation Theory and the Numerical Simulation of Igneous Crystallisation. In R. B. Hargraves, editor, *Physics of Magmatic Processes*, chapter 10. Princeton University Press, 1980.

[25] C. Dupas, H. Green, and T. Young. Analytical electron microscopy of a synthetic peridotite experimentally deformed in the β olivine stability field. *Journal of Geophysical Research*, 99:15821–15832, 1994.

[26] M. Eden. A two dimensional growth process. In J. Neyman, editor, *Proceedings of the Fourth Berkeley Symposium on Mathematical Statistics and Probability*, pages 223–239, Berkeley, CA., 1961. University of California Press.

[27] C. Faloutsos and I. Kamel. Relaxing the Uniformity and Independence Assumptions Using the Concept of Fractal Dimension. *Journal of Computer and System Sciences*, 55:229–240, 1997.

[28] D. Fitts. *Nonequilibrium thermodynamics.* McGraw-Hill, New York, 1962.

[29] R. C. Fletcher and D. D. Pollard. Anticrack model for pressure solution surfaces. *Geology*, 9:419–424, 1981.

[30] C. Fowler. *The solid earth.* Cambridge University Press, Cambridge, 2001.

[31] A. L. Frisillo and G. R. Barsch. Measurements of single-crystal elastic constants of bronzite as a function of pressure and temperature. *Journal of Geophysical Research*, 77:6360–6384, 1972.

[32] H. Frost and C. Thompson. The effect of nucleation conditions on the topology and geometry of two-dimensional grain structures. *Acta metallurgica*, 35(2):529–540, 1987.

[33] H. J. Frost and M. F. Ashby. *Deformation-Mechanism Maps*. Pergamon, 1982.

[34] C. A. Geiger and A. Feenstra. Molar volumes of mixing of almandine-pyrope and almandine-spessartine garnets and the crystal chemistry and thermodynamic-mixing properties of the aluminosilicate garnets. *American Mineralogist*, 82:571–581, 1997.

[35] C. Gerthsen, H. Knesel, and H. Vogel. *Physik*. Springer, Berlin, 1989.

[36] J. Gibbs. On the equlibrium of heterogeneous substances. In *Collected works of J. Willard Gibs*, volume 1. Yale University Press, 1906.

[37] M. Gölke and J. Mechie. Finite-element modelling of the structure and evolution of the South Kenya Rift, East Africa. *Tectonophysics*, 236:439–452, 1994.

[38] J. Gouyet, M. Rosso, and B. Sapoval. Fractal Surfaces and Interfaces. In A. Bunde and S. Havlin, editors, *Fractals and Disordered Systems*, pages 264–301. Springer, New York, 1996.

[39] M. Grah, K. Alzebdeh, P. Sheng, M. Vaudin, K. Bowman, and M. Ostatoja-Starzewski. Brittle intergranular failure in 2D microstructures: Experiments and computer simulations. *Acta mater*, 44(10):4003–4018, 1996.

[40] H. Green II and P. Burnley. A new self-organizing mechanism for deep-seated earthquakes. *Nature*, 341:733–737, 1989.

[41] H. Green II and H. Houston. The mechanics of deep earthquakes. *Annual Review of Earth and Planetary Sciences*, 23:169–213, 1995.

[42] Y. Gueguen and A. Nicolas. Deformation of Mantle Rocks. *Annual Reviews of Earth and Planetary Sciences*, 8:119–144, 1980.

[43] E. Hering, R. Martin, and M. Stohrer. *Physik für Ingenieure*. VDI-Verlag, Düsseldorf, 1992.

[44] D. Hugh-Jones. Thermal expansion of $MgSiO_3$ and $FeSiO_3$ ortho- and clinopyroxenes. *American Mineralogist*, 82:689–696, 1997.

[45] T. Irifune. An experimental investigation of the pyroxene-garnet transformation in a pyrolite composition and its bearing on the constitution of the mantle. *Physics of the Earth and Planetary Interiors*, 45(4):324–336, 1987.

[46] T. Irifune and A. E. Ringwood. Phase transformations in a harzburgite composition to 26 GPa: implications for dynamical behaviour of the subducting slab. *Earth and Planetary Science Letters*, 86(2-4):365–376, 1987.

[47] J. Ita and L. Stixrude. Petrology, Elasticity and Composition of the Mantle Transition Zone. *Journal of Geophysical Research*, 97(B5):6849–6866, 1992.

[48] E. Ito and T. Takahashi. Post spinel transformations in the system $Mg_2SiO_4 - Fe_2SiO_4$ and some geophysical implications. *Journal of Geophysical Research*, 94:10637–10646, 1989.

[49] M. W. Jessel, P. D. Bons, L. Evans, T. D. Barr, and K. Stüwe. Elle, the numerical simulation of metamorphic and deformation textures. *Computers & Geosciences*, 27:17–30, 2001.

[50] W. Johnson and R. Mehl. Reaction kinetics in processes of reaction and growth. *Trans AIME*, 135:42–58, 1939.

[51] S. Karato. Grain-size distribution and rheology of the upper mantle. *Tectonophysics*, 104:155–176, 1984.

[52] S. Karato. *The Dynamic Structure of the Deep Earth.* Princeton University Press, Princeton, 2003.

[53] S. Karato, C. Dupas-Bruzek, and D. Rubie. Plastic deformation of silicate spinel under the transition-zone conditions of the Earthâ**s mantle. *Nature*, 395:266–269, 1998.

[54] S. Karato, M. Riedel, and D. Yuen. Rheological structure and deformation of subducted slabs in the mantle transition zone: implications for mantle circulation and deep earthquakes. *Physics of the Earth and Planetary Interiors*, 127(3-4):83–108, 2001.

[55] S. Karato and P. Wu. Rheology of the Upper Mantle. *Science*, 260:771–778, 1993.

[56] W. T. Kelvin. On the Division of Space with Minimum Partitional Area. *Philosophical Magazine*, 24(151):503, 1887.

[57] B. Kiefer, L. Stixrude, J. Hafner, and G. Kresse. Structure and elasticity of wadsleyite at high pressures. *American Mineralogist*, 86:1387–1395, 2001.

[58] S. King. *Mineral Physics and Crystallography: A Handbook of Physical Constants*, chapter Models of Mantle Viscosity, pages 227–236. American Geophysical Union, Washington, D.C., 1995.

[59] R. J. Kirkpatrick. Towards a kinetic model for the crystallization of magma bodies. *Journal of Geophysical Research*, 81:2565–2571, 1976.

[60] D. Koehn. Fracturing. In P. Bons, D. Koehn, and M. Jessel, editors, *Microdynamics Simulation*, pages 171–181. Springer, Berlin, 2008.

[61] D. Koehn, J. Arnold, B. Jamtveit, and A. Malthe-Sorenssen. Instabilities in stress corrosion and the transition to brittle failure. *American Journal of Science*, 303:956–971, 2003.

[62] D. Koehn, A. Malthe-Sorenssen, and C. W. Passchier. The structure of reactive grain-boundaries under stress containing confined fluids. *Chemical Geology*, 230:207–219, 2006.

[63] W. Langbein. *Thermodynamik*. Verlag Harri Deutsch, Frankfurt am Main, 1999.

[64] A. Lasaga. *Kinetic Theory in the Earth Sciences*. Princeton Series in Geochemistry. Princeton University Press, New Jersey, 1998.

[65] L. Li, H. Long, P. Raterron, and D. Weidner. Plastic flow of pyrope at mantle pressure and temperature. *American Mineralogist*, 91:517–525, 2006.

[66] R. C. Liebermann. *Earth's Deep Interior. Mineral Physics and Tomography From the Atomic to the Global Scale*, chapter Elasticity of Mantle Minerals, pages 181–199. American Geophysical Union, Washington D.C., 2000.

[67] D. A. Lockner, J. D. Byerlee, V. Kuksenko, A. Ponomarev, and A. Sidorin. Quasi-static fault growth and shear fracture energy in granite. *Nature*, 350:39–42, 1991.

[68] S. Mackwell. High-temperature rheology of enstatite: Implications for creep in the mantle. *Geophysical Research Letters*, 18:2027–2030, 1991.

[69] K. Mahin, H. Kentaon, and J. W. Morris Jr. Comparative analysis of the cellular and Johnson-Mehl microstructures through computer simulation. *Acta metallurgica*, 28:443–453, 1980.

[70] A. Malthe-Sørenssen, T. Walmann, J. Feder, T. Jossang, and P. Meakin. Simulation of extensional clay fractures. *Physical Review E*, 58(5):5548–55641, 1998.

[71] P. Meakin. Noise-reduced and anisotropy-enhanced Eden and screened-growth models. *Physical Reviews*, A 38:418–426, 1988.

[72] L. Monette and M. P. Anderson. Elastic and fracture properties of the two-dimensional triangular and square lattice. *Modelling and Simulation in Materials Science and Engineering*, 2:53–66, 1994.

[73] J. Mosenfelder, M. Frederic, C. Ross, L. Kerschgofer, and D. Rubie. Experimental constraints on the depth of olivine metastability in subducting lithosphere. *Physics of the Earth and Planetary Interiors*, 127:165–180, 2001.

[74] A. Navrotsky. Thermodynamic Relations Among Olivine, Spinel and Phenacite Structures in Silicates and Germanates: I. Volume Relations and the Systems NiO-MgO-GeO_2, and CoO-MgO-GeO_2. *Journal of Solid State Chemistry*, 6:21–41, 1973.

[75] M. Nordmeier. *Zugänge zur nichtlinearen Physik am Beispiel am Beispiel fraktaler Wachstumphänomene.* Lit Verlag, Münster, 1999.

[76] R. J. O'Connel. On the scale of mantle convection. *Tectonophysics*, 38:119–136, 1977.

[77] I. Orgzall and B. Lorenz. Computer simulations of cluster-size distributions in nucleation and growth processes. *Acta metallurgica*, 36:627–631, 1988.

[78] M. Ostoja-Starzewski, P. Y. Sheng, and K. Alzebedeh. Spring network models in elasticity and fracture of composites and polycrystals. *Computational Material Science*, (7):82–93, 1996.

[79] V. Pal, M. Singh, and B. R. K. Gupta. Analysis of thermal expansion coefficients under the effect of high temperature for minerals. *Journal of Physics and Chemistry of Solids*, 60:1895–1896, 1999.

[80] P. Pfeifer and M. Obert. Fractals: basic concepts and terminology. In D. Avnir, editor, *The Fractal Approach to Heterogeneous Chemistry*. Wiley, New York, 1989.

[81] W. H. Press, S. A. Teukolky, W. T. Vetterling, and B. P. Flannery. *Numerical Recipes in C: The Art of Scientific Computing*. Cambridge University Press, New York, 1992.

[82] A. Putnis. *Introduction to Mineral Sciences*. Cambridge University Press, 1992.

[83] H. Ramberg. Particle paths, displacement and progressive strain applicable to rocks. *Tectonophysics*, 28:1–37, 1975.

[84] G. Ranalli. *Rheology of the earth*. Chapman & Hall, London, 1995.

[85] F. Reis. Depinning Transitions in Interface Growth Models. *Brazilian Journal of Physics*, 33:501–513, 2003.

[86] M. Riedl and S. Karato. Microstructural development during nucleation and growth. *Geophysical Journal International*, 125:397–414, 1996.

[87] M. R. Riedl and S. Karato. Grain-size evolution in subducted oceanic lithosphere associated with the olivine-spinel transformation and its effects on rheology. *Earth and Planetary Science Letters*, (148):27–43, 1997.

[88] E. M. Riggs and H. W. Green. Shear localization in tansformation-induced faulting: first-order similarities to brittle shear failure. *Tectonophysics*, (340):95–107, 2001.

[89] A. Ringwood. Phase transformations and their bearing on the constitution and dynamics of the mantle. *Geochimica and Cosmochimica Acta*, 55:2083–2110, 1991.

[90] E. A. Ringwood. *Composition and Petrology of the Earth Mantle*. McGraw-Hill, New York, 1975.

[91] D. Rubie and C. Ross. Kinetics of the olivine-spinel transformation in subducting lithosphere: experimental constraints and implications for deep slab processes. *Physics of the Earth and Planetary Interiors*, (86):223–241, 1994.

[92] A. Saada. *Elasticity: theory and applications*. Krieger, Malabar, 1993.

[93] T. Saetre, O. Hunderi, and E. Nes. Computer simulation of primary recrystallisation microstructures: the effect of nucleation and growth kinetics. *Acta metallurgica*, 34(6):981–987, 1986.

[94] I. Shimizu. Nonhydrostatic and Nonequilibrium Thermodynamics of Deformable Materials. *Journal of Geophysical Research*, 97(B4):4587–4597, 1992.

[95] T. Stace. How small is a solid? *Nature*, 331:116–117, 1988.

[96] K. Suito. Phase relations of pure Mg_2SiO_4 up to 200 kilobars. In M. H. Manghani and S. Akimoto, editors, *High Pressure Research - Applications to Geophysics*. Academic Press, Orlando, 1977.

[97] C. Sung and R. Burns. Kinetics of high-pressure phase transformations: implications to the evolution of the olivine - spinel transition in the downgoing lithosphere and its consequences on the dynamics of the mantle. *Tectonophysics*, 31:1–32, 1976.

[98] C. Sung and R. Burns. Kinetics of the olivine→spinel transition: implications to deep focus earthquake genesis. *Earth and Planetary Science Letters*, 32:165–170, 1976.

[99] M. F. Thorpe and I. Jasiuk. New Results in the Theory of Elasticity for Two-Dimensional Composites. *Proceedings of the Royal Society of London*, A438:531–544, 1992.

[100] Tran-Thong. Ellipse, arc of ellipse and elliptic spline. *Computers and Graphics*, 7(2):169–175, 1983.

[101] P. Vaughan, H. Green, and R. Coe. Anisotropic growth in the olivine-spinel transformation of Mg_2GeO_4 under nonhydrostatic stress. *Tectonophysics*, 108:299–322, 1984.

[102] T. Vicsek. *Fractal Growth Phenomena*. World Scientific, Singapore, 1992.

[103] E. Wachspresse and G. Habetler. An alternating-direction-implicit iteration technique. *Journal of the Society of Industrially Applied Mathematics*, (8):403–424, 1960.

[104] D. J. Weidner and N. Hamaya. Elastic properties of the olivine and spinel polymorphs of Mg_2GeO_4, and evaluation of elastic analogues. *Physics of the Earth and Planetary Interiors*, 33:275–283, 1983.

[105] R. Weijermars. The role of stress in ductile deformation. *Journal of Structural Geology*, 13:1061–1078, 1991.

[106] T. E. Young, H. W. Green, A. M. Hofmeister, and D. Walker. Infrared spectroscopic investigation of hydroxyl in $\beta(Mg,Fe)_2SiO_4$ and coexisting olivine: Implications for mantle evolution and dynamics. *Physics and Chemistry of Minerals*, 19:409–422, 1993.

[107] C. S. Zha, T. S. Duffy, R. T. Downs, H. K. Mao, and R. J. Hemley. Brillouin scattering and X-ray diffraction of San Carlos olivine: direct pressure determination to 32 GPa. *Earth and Planetary Science Letters*, 159:25–33, 1998.